Multi-Stage Amphoteric Redox Hydrocarbons Containing Phenalenyl Units.

Takashi Kubo

1996

Department of Chemistry, Graduate School of Science,
Osaka University

Multi-Stage Amphoteric Redox Hydrocarbons Containing Phenalenyl Units.

Takashi Kubo

1996

Department of Chemistry, Graduate School of Science,
Osaka University

Contents

– Chapter 1 –

General Introduction

In principle, any molecule can behave as a "donor" or "acceptor". For example, many aromatic compounds are subject to oxidation and reduction to give cation and anion species, respectively. Addition or removal of electrons to or from a molecule is well-known to cause the dramatic change of properties; for that matter chemical reactivity, color, magnetic susceptibility, and so on. However, most of reduced or oxidized compounds such as radicals, cations, and anions, *i.e.* redox compounds, are unstable thermodynamically and/or kinetically, namely highly reactive. This prevents the detailed investigation of the properties of the redox states. The stability of a given species will depend not only on its own ionization potential and electron affinity but also on the distribution pattern of electrons. The most important factor to stabilize redox states of a molecule should depend on high oxidation and reduction ability, and highly delocalized structure of electrons.

Recently studies have been accumulated of the redox chemistry which plays an important role in electroconductors,[1] photosynthetic systems,[2] electrogenerated chemiluminescence,[3] and so on. Thus the design and the investigation of redox systems are interesting not only from a purely scientific but also from a material point of view.

Some conjugated hydrocarbons are known to exhibit the amphoteric redox property that a molecule is oxidized and reduced by multi-stage electron transfer. The numerical sum of oxidation potential (E^{ox}) and reduction potential (E^{red}), *i.e.* $E^{sum} = E^{ox} + (-E^{red})$, might be used to evaluate the extent of the amphoteric redox property of a given molecule. Hünig investigated such amphoteric redox systems as polyene [4a,b] **1.1**, **1.2**, **1.3**, and **1.4**. These compounds reportedly behave as four-stage amphoteric redox compounds (Figure 1.1).

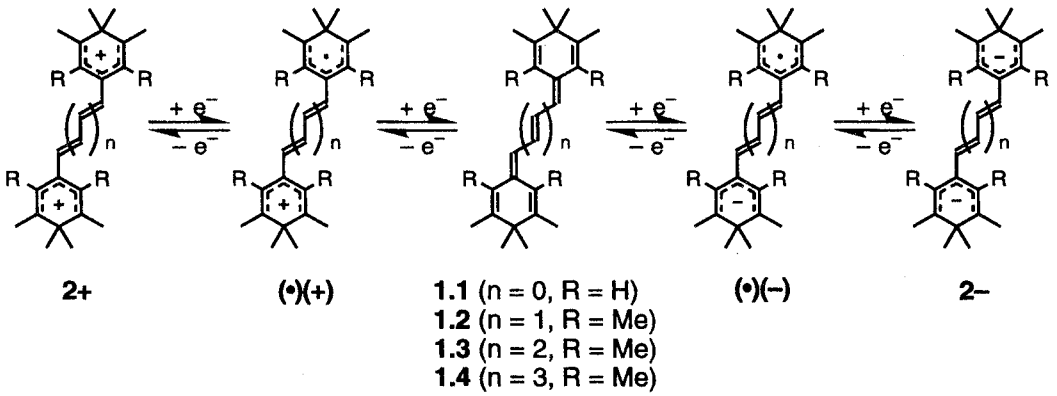

Figure 1.1. Four-stage amphoteric redox behavior of **1.1**, **1.2**, **1.3**, and **1.4**

However, these compounds were not designed so as to exhibit high redox ability and thus gave a relatively high E_1^{sum} value.

A compound with low ionization potential and high electron affinity, *i.e.* high HOMO and low LUMO, will show high redox ability to give stable redox states. In particular, a compound with NBMO as frontier orbitals will be a potential candidate to exhibit the highest redox ability, because addition or removal of electrons in NBMO should not change the magnitude of π-electron energy in the simple HMO approximation. A representative is phenalenyl radical **1.5**•, which has a NBMO with an occupation number of one. This radical exhibits a relatively small E_1^{sum} value of 1.6 V among hydrocarbons. Three redox states (**1.5**$^+$, **1.5**•, and **1.5**$^-$) of phenalenyl species are known to be stable thermodynamically and the properties of them have been investigated in detail.[5] However, the open-shell phenalenyl radical suffers from a serious disadvantage, *i.e.* lack of kinetic stability. Phenalenyl radical tends to dimerize or to give oxidized species in the presence of air as ordinary radicals. Thus molecules with a closed-shell structure retaining the high redox ability of phenalenyl species will promise to develop the stable redox compounds with a small E^{sum} value.

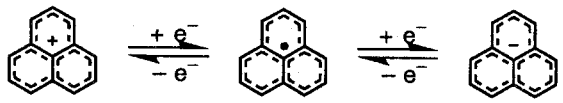

1.5•

Figure 1.2. Two-stage amphoteric redox behavior of phenalenyl radical **1.5**•

On the basis of these concepts, 1,2-bis(phenalene-1-ylidene)ethane **1.6** (BPLA) [4c] was designed and synthesized. As shown in Figure 1.3, the replacement of two 1,4-cyclohexadienyl units as essential redox sites in **1.1** with two phenalenyl units leads to the compound **1.6**. Expectedly, **1.6** behaved as a four-stage amphoteric redox system and exhibited a small E_1^{sum} value of 1.51 V. The two phenalenyl units with higher redox ability clearly contribute to the smaller E_1^{sum} value compared to **1.1**.

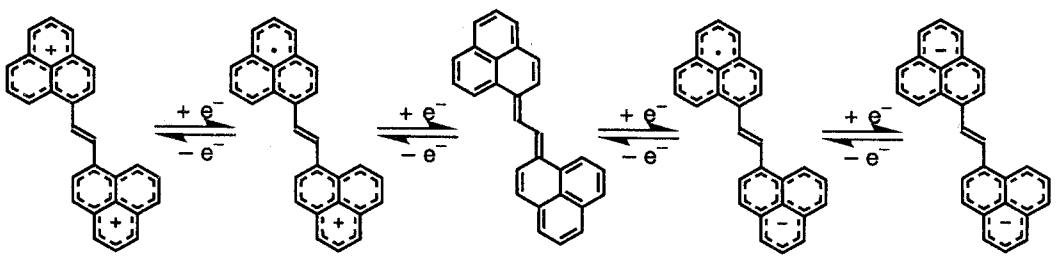

1.6^{2+} **1.6**$^{(•)(+)}$ BPLA **1.6** **1.6**$^{(•)(-)}$ **1.6**$^{2-}$

Figure 1.3. Four-stage amphoteric redox behavior of **1.6**

For a smaller E_1^{sum} value, polycyclic aromatic hydrocarbons **1.7** (PDPL) [4d] and **1.8** (IDPL) [4e] were designed and synthesized. These compounds are designed as the unstable structure in the neutral state should disappear in the oxidation and reduction states. The compound **1.7** contains a pentalene structure, while an *s*-indacene structure is built in the center of **1.8**. [6] They have indeed the considerably small E_1^{sum} values of 0.99 V for **1.7** and 1.10 V for **1.8**. The former shows the smallest value among the closed-shell hydrocarbons reported so far.

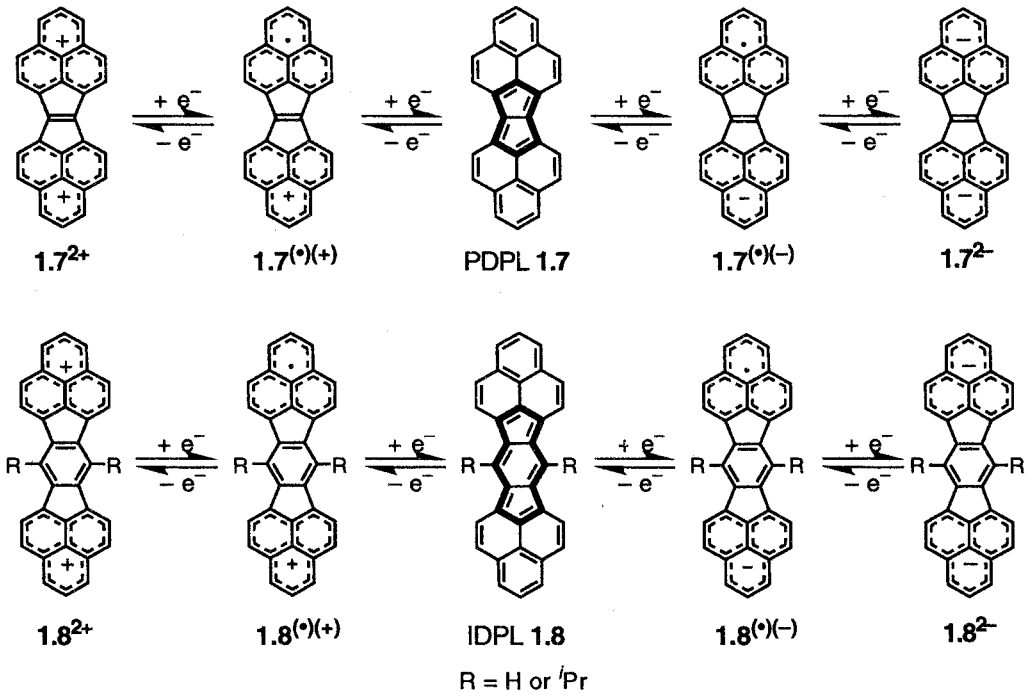

Figure 1.4. Four-stage amphoteric redox behavior of **1.7** and **1.8**

Table 1.1 lists the electrochemical data of some redox compounds.

Table 1.1. Cyclic voltammetric data of redox compounds

	E_2^{ox}	E_1^{ox}	E_1^{red}	E_2^{red}	E_1^{sum}	E_2^{sum}
1.1 [a]	+1.04	+0.68	-2.12	-2.64	2.80	3.68
1.2 [a]	+0.68	+0.60	-1.95	-2.44*	2.55	3.12
1.3 [a]	+0.68	+0.59	-1.83	-2.8*	2.51	3.39
1.4 [a]	+0.60	+0.56	-1.67	-1.99	2.27	3.55
1.5 [b]		+0.7	-0.9		1.6	
BPLA **1.6** [c]	+0.83*	+0.39	-1.12	-1.35	1.51	2.18
BPLE **1.9** [d]	+0.78*	+0.51	-0.83	-1.21	1.34	1.99
PDPL **1.7** [d]	+1.02*	+0.56*	-0.43	-1.17	0.99	2.19
IDPL **1.8** (^{i}Pr) [e]	+0.84*	+0.62*	-0.48	-1.07	1.10	1.91

[a] Measured against Ag/AgCl in DMF/benzene or CH_2Cl_2 with $^nBu_4NBF_4$ as supporting electrolyte at -60 °C; sweep rate 200 mVs^{-1}. [b] Measured against the saturated calomel electrode (SCE) in CH_3CN with 0.1 M $^nBu_4NBF_4$. [c] Measured against the saturated calomel electrode (SCE) in DMF with 0.1 M Et_4NClO_4 as supporting electrolyte at -50 °C; sweep rate 7 mVs^{-1}. [d] Measured against the saturated calomel electrode (SCE) in DMF with 0.1 M Et_4NClO_4 as supporting electrolyte at -50 °C; sweep rate 30 mVs^{-1}. [e] Measured against the saturated calomel electrode (SCE) in DMF with 0.1 M Et_4NClO_4 as supporting electrolyte at -40 °C; sweep rate 500 mVs^{-1}.
The values by an astrerisk correspond to irreversible wave.

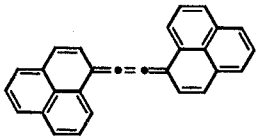

BPLE **1.9** [4f]

An E_1^{sum} value helps to investigate the redox behavior of a given molecule and the electronic structure of the redox states will also provide significant information on the development of stable redox compounds with higher amphotericity. Unfortunately, the instability of the compounds described above left the investigation of such properties unexplored.

In the following chapters, I will describe the interesting properties of three redox systems, *i.e.* TTB-IDPL **1.10**, TTB-as-IDPL **1.11**, and HTB-TBzD **1.12•**, which are stabilized kinetically with bulky *tert*-butyl groups.

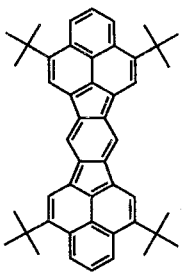

1.10

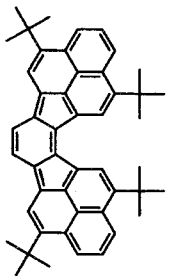

1.11

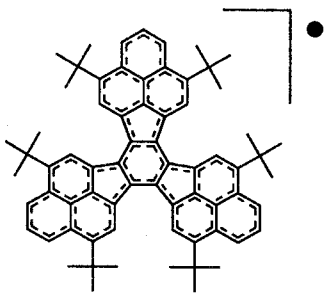

1.12

References

1) J. R. Ferraro, J. M. Williams, *Introduction to synthetic electrical conductors*; Academic Press, New York, 1987; J. B. Torrance, *Acc. Chem. Res.*, **1979**, *12*, 79; F. Wudl, *Acc. Chem. Res.*, **1984**, *17*, 227; K. Nakasuji, M. Nakatsuka, I. Murata, *Yuki Gousei Kagaku Kyoukaisi*, **1983**, *41*, 204; G. Saito, N. Okada, *Yuki Gousei Kagaku Kyoukaisi*, **1987**, *45*, 501; K. Nakasuji, M. Sasaki, I. Murata, *Yuki Gousei Kagaku Kyoukaisi*, **1988**, *46*, 956.

2) J. S. Connolly, J. R. Bolton, *Photoinduced Electron Tranfer*. M. A. Fox, M. Chanon, Ed. Elsevier, 1988, Part D, p 303; J. T. Meyer, *Acc. Chem. Res.* **1989**, *22*, 163.

3) J. D. Debad, J. C. Morris, V. Lynch, P. Magnus, A. J. Bard, *J. Am. Chem. Soc.* **1996**, *118*, 2374, and references cited therein.

4) a) B. Hagenbruch, K. Hesse, S. Hünig, G. Klug, *Justus Liebigs Ann. Chem.* **1981**, 256. b) S. Hünig, M. Hornaer, P. Schilling, *Angew. Chem. Int. Ed. Engl.* **1975**, *14*, 556. c) K. Nakasuji, K. Yoshida, I. Murata, *J. Am. Chem. Soc.* **1982**, *104*, 1432. d) K. Nakasuji, K. Yoshida, I. Murata, *J. Am. Chem. Soc.* **1983**, *105*, 5136. e) I. Murata, S. Sasaki, K. -U. Klabunde, J. Toyoda, J. Nakasuji, *Angew. Chem. Int. Ed. Engl.* **1991**, *30*, 172. f) K. Nakasuji, K. Yoshida, I. Murata, *Chem. Lett.* **1982**, 969. See also, V. D. Parker, *J. Am. Chem. Soc.* **1976**, *98*, 98; K. Deuchert, S. Hünig, *Angew. Chem. Int. Ed. Engl.* **1978**, *17*, 875; K. Takahashi, T. Suzuki, *J. Am. Chem. Soc.* **1989**, *111*, 5483; K. Takahashi, *Pure. Appl. Chem.* **1993**, *65*, 127; R. Bachmann, F. Gerson, G. Gescheidt, E. Vogel, *J. Am. Chem. Soc.* **1992**, *114*, 10855; R. Bachmann, F. Gerson, G. Gescheidt, E. Vogel, *J. Am. Chem. Soc* **1993**, *115*, 10286; E. Vogel, J. Dörr, A. Herrmann, J. Lex, H. Schmickler, P. Walgenbach, J. P. Gisselbrecht, M. Gross, *Angew. Chem. Int. Ed. Engl.* **1993**, *32*, 1597.

5) D. H. Reid, *Quart. Rev.* **1965**, *19*, 274; F. Gerson, *Helv. Chim. Acta*, **1966**, *49*, 1463; H. Prinzbach, V. Freudenberger, U. Scheidegger, *Helv. Chim. Acta*, **1967**, *50*, 1087; I. Sethson, D. Johnels, U. Edlund, A. Sygula, *J. Chem. Soc. Perkin Trans 2*. **1990**, 1339.

6) Both pentalenes and *s*-indacenes with a periphery having $4n\pi$ electrons are known to be highly reactive compounds. See, K. Hafner, *Angew. Chem. Int. Ed. Engl.* **1964**, *3*, 165; R. Dönges, K. Hafner, H. J. Lindner, *Tetrahedron Lett.* **1976**, 1345; M. Suda, *Yuki Gousei Kagaku Kyoukaisi*, **1978**, *36*, 657; K. Hafner, B. Stowasser, H. -P. Krimmer, S. Fischr, M. C. Böhm, H. J. Lindner, *Angew. Chem. Int. Ed. Engl.* **1986**, *25*, 630.

– Chapter 2 –

Properties of tetra-*tert*-butyl-*s*-indaceno[1,2,3-*cd*:5,6,7-*c'd'*]diphenalene (TTB-IDPL)

2.1 Introduction

The recent studies of BPLA,[1] BPLE,[2] and PDPL[3] revealed that each of the multi-stage amphoteric redox compounds containing phenalenyl units show a high amphotericity as expected and the phenalenyl units play an important role in developing the amphoteric redox property. In particular, PDPL exhibited much smaller E_1^{sum} value (0.99 V) than those of BPLA (1.51 V) and BPLE (1.31 V). This finding suggests that the concept shown in Figure 1.4 occupies an importmat position to develop higher amphoteric compounds. On the basis of the concept, IDPL **2.1** containing unstable *s*-indacene structure in neutral state was designed and studied by Sasaki,[4] Masui,[5] and Ohashi[6] (Figure 2.1.1).

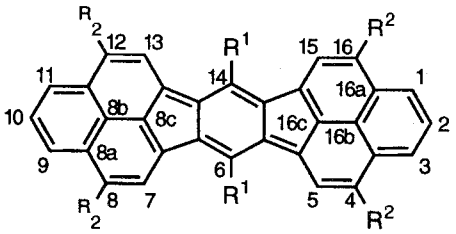

α^1 : 1,3,9,11
α^2 : 4,8,12,16
α^3 : 5a,6b,13a,14b
β^1 : 2,10
β^2 : 5,7,13,15

2.1 $R^1 = R^2 = H$
2.2 $R^1 = {}^i\text{Pr}$, $R^2 = H$
2.3 $R^1 = H$, $R^2 = {}^t\text{Bu}$

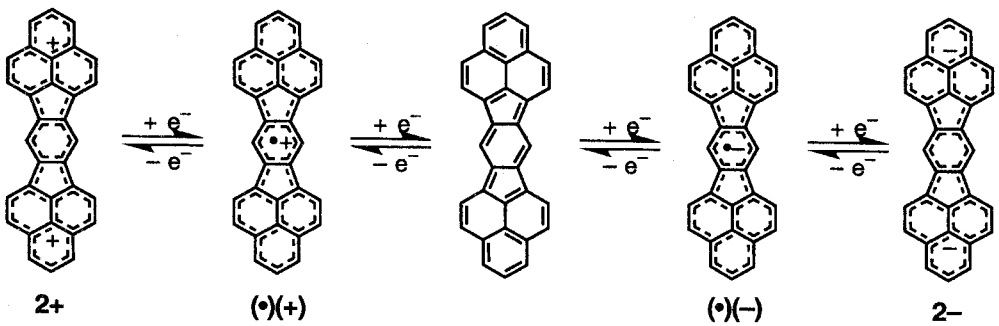

Figure 2.1.1. Four-stage amphoteric redox of IDPL **2.1**

In comparison with PDPL, IDPL was expected to exhibit smaller E_1^{sum} value because the charge and the spin of IDPL could be delocalized over more sp^2 carbons.

Theoretical consideration (HMO calculations, Figure 2.1.2) supported this assumption. The HOMO–LUMO gap of IDPL (0.24β) is smaller than that of PDPL (0.36β). Contrary to expectation, electrochemical experiment of IDPL exhibited larger E_1^{sum} values (1.10 V for **2.2**, 1.16 V for **2.3**) than that of PDPL (0.99 V).

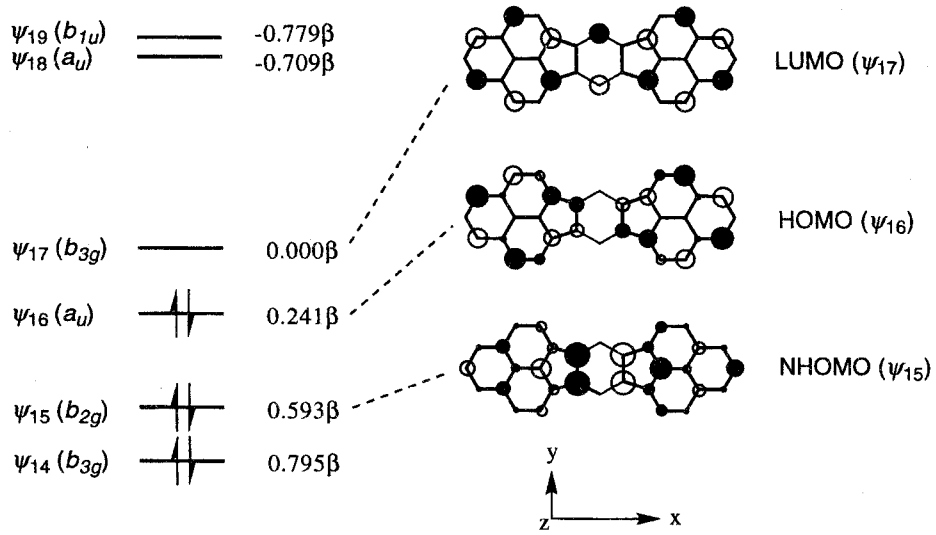

Figure 2.1.2. Selected molecular orbitals of **2.1** calculated by the HMO method.

Primary interest of potentially amphoteric redox compounds is evaluation of the magnitude of E_1^{sum} value. Another prominent feature is that these compounds may expectedly give *stable* reduced and oxidized states. A compound is not unusual to give plural redox states. For example, neutral naphthalene is known to give radical anion and radical cation species. However, limited examples give five redox states.

Sasaki, Masui, and Ohashi revealed the properties of dication, dianion, and neutral states of IDPL. The properties of the remaining radical cation and radical anion are also important. Furthermore, there are many other interesting properties in neutral IDPL. As described in Chapter 3 and 4, tetra-*tert*-butyl IDPL is extremely stable compared to TTB-as-IDPL **3.2** and HTB-TBzD **4.3**•. These considerations dictated us to study the properties of TTB-IDPL.

2.2 Synthesis of TTB-IDPL

TTB-IDPL **2.3** was recently synthesized by Ohashi.[6] The synthetic procedure of **2.3** is shown in Scheme 2.1.2. TTB-IDPL was found to be stable in the solid state for a year but gradually decomposed in solution. The solid was found to remain unchanged even at 300 °C in a sealed degassed tube. In comparison with unsubstituted or diisopropyl IDPL, **2.3** showed higher solubility and stability due to the bulky *tert*-butyl groups. Recrystallization from benzene gave so pure green prisms that its elementary analysis data was in good agreement with the calculation.

Calcd for $C_{48}H_{48}$: C 92.26%, H 7.74%; found C 92.29%, H 7.79%.

Scheme 2.1.1. Synthetic procedure of **2.3**

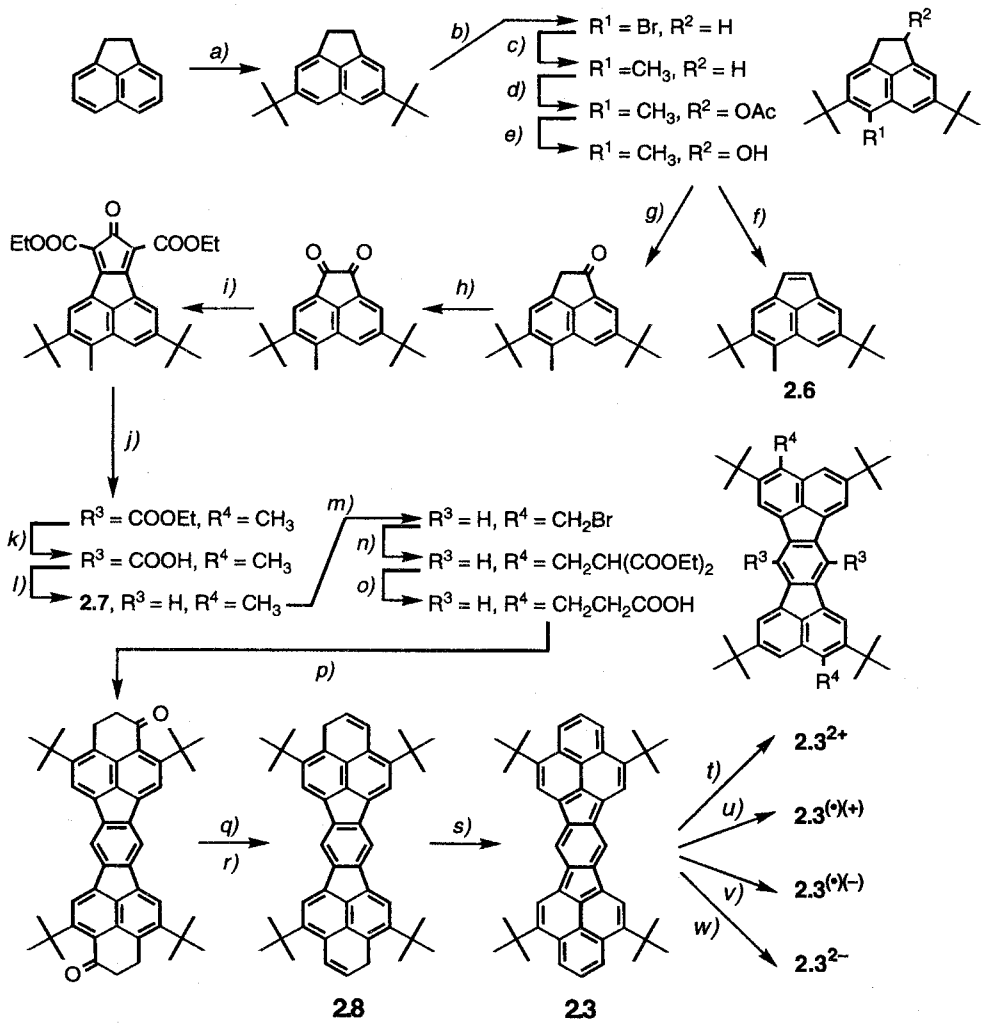

Reaction conditions : *a)* ^{t}BuCl, $AlCl_3$, CH_2Cl_2, rt, 3h, 64%. *b)* NBS, DMF, rt, 2 d, 43%. *c)* 1) ^{n}BuLi, 2) CH_3I, THF, -75°C to rt, 12 h, 94%. *d)* Pb_3O_4, AcOH + benzene, reflux, 2.5 h, 78%. *e)* KOH, EtOH + H_2O, reflux, 1 h, 94%. *f)* cat. *p*-toluenesulfonic acid, benzene, reflux, 20 min, 91%. *g)* Jones reagent, acetone, rt, 2 h, 92%. *h)* NBS, DMSO, 50°C, 36 h, 80%. *i)* Diethyl acetone-1,3-dicarboxylate, Et_3N, THF + MeOH, rt, 12 h, 46%. *j)* 1) **2.6**, reflux, 1 h 20 min, 2) *p*-chloranil, reflux, 3 h 30min, xylenes, 99%. *k)* LiI, DMF, reflux, 4 d, 99%. *l)* Cu_2O, quinoline, reflux, 3 h, 95%. *m)* NBS, benzoyl peroxide, benzene, reflux, 25 min. *n)* NaOEt, $CH_2(COOEt)_2$, EtOH + benzene, rt, 3 d, 77%(2 steps). *o)* 1) aqueous KOH, EtOH, reflux, 20 h, 2) 4 N HCl, 3) reflux, H_2O, 84 h, 98%. *p)* 1) $(COCl)_2$, benzene, reflux, 2 h, 2) $AlCl_3$, CH_2Cl_2, -50°C, 3 h, 82%. *q)* LAH, THF, rt, 2 h, 83%. *r)* cat. *p*-toluenesulfonic acid, benzene, reflux, 5 min, 81%. *s)* *p*-chloranil, benzene, reflux, 40 min, 78%. *t)* D_2SO_4 or excess $SbCl_5$, CH_2Cl_2. *u)* 1 eq $SbCl_5$, CH_2Cl_2. *v)* K-mirror, under vacuum, THF or DME. *w)* K-mirror, under vacuum, THF-d_8.

The cyclic voltammetry of **2.3** gave rise to four reversible redox waves (E_2^{ox} = +0.84 V, E_1^{ox} = +0.48 V, E_1^{red} = –0.67 V, E_2^{red} = –1.25 V; E_1^{sum} = 1.16 V, E_2^{sum} = 2.09 V).

2.3 NMR spectroscopy

2.3.1 Neutral

^{1}H and ^{13}C NMR spectra of TTB-IDPL **2.3** were recorded at –30 °C. Figure 2.3.1 shows the aromatic region of the ^{1}H NMR spectrum of **2.3**. The ^{1}H and ^{13}C NMR chemical shifts are given in Figure 2.3.2. Assignments of individual ^{1}H and ^{13}C resonances are comfirmed by NOESY, HMBC, and HMQC experiments.

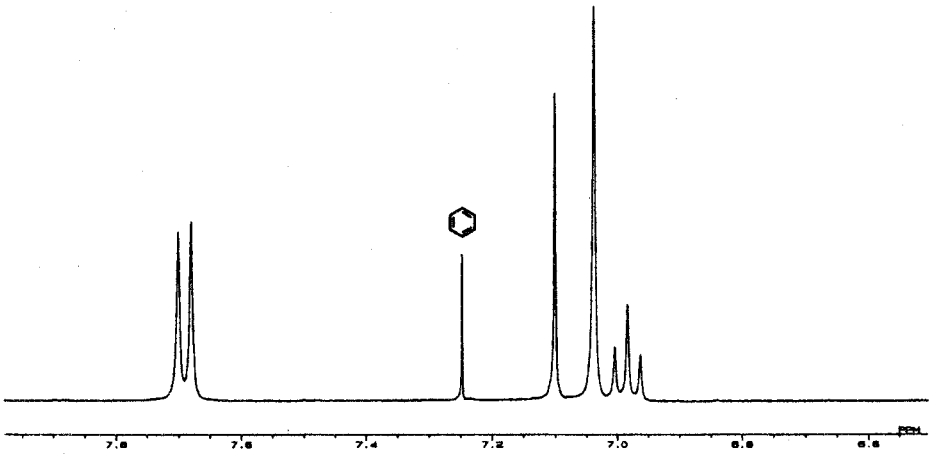

Figure 2.3.1. ^{1}H NMR spectrum of **2.3** in acetone-d_6 + CS_2 (1:4) at –30 °C.

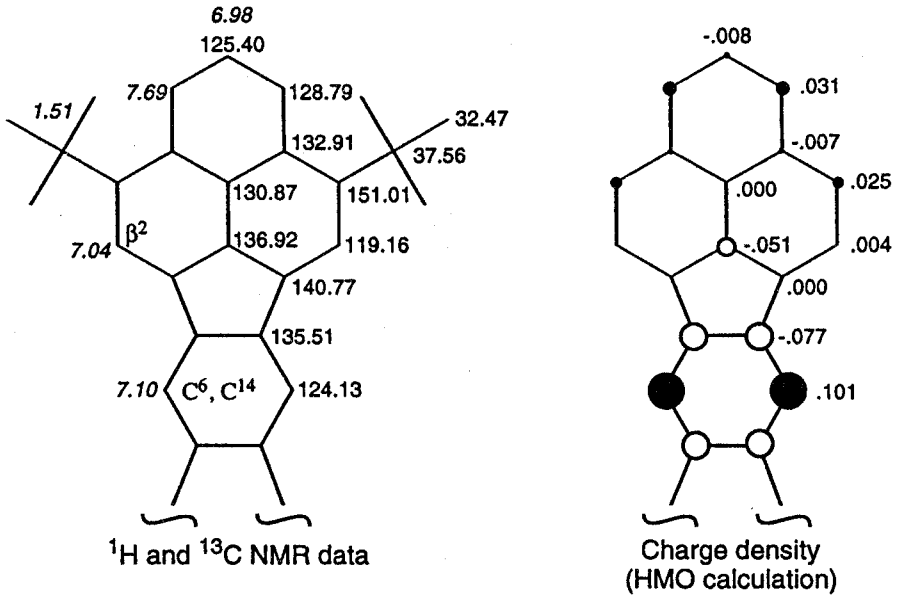

Figure 2.3.2. NMR data and charge density of **2.3**

Examination of the pattern of ^{1}H and ^{13}C signals suggests that **2.3** possesses an molecular flamework with D_{2h} symmetry but not the localized bond structure with C_{2h} symmetry. At elevated temperatures, progressive line broadening was observed (Figure 2.3.3). The line broadening is reversible upon a temperature change of the sample solution.

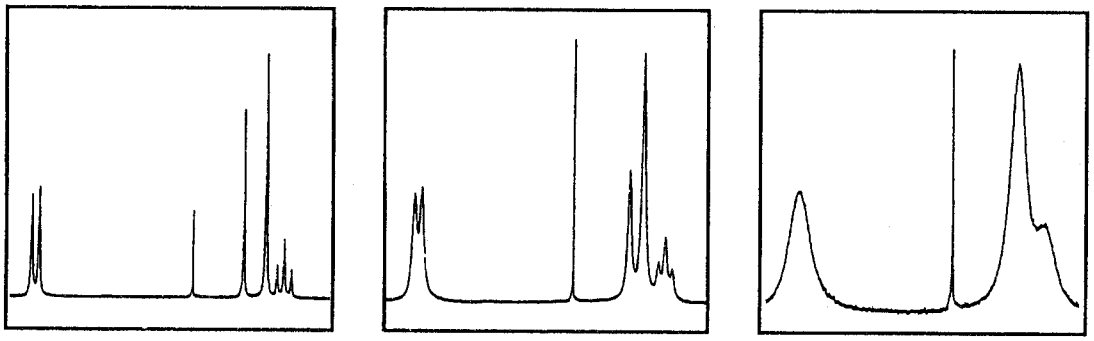

Figure 2.3.3. Temperature dependance of ^{1}H NMR spectrum of **2.3**

Most indicative are that 1) a trace of unidentificable radical species was detected by ESR spectroscopy at such higher temperature that the broadening of ^{1}H NMR spectra was observed; 2) the solid **2.3** gave triplet signal which increased in intensity with higher temperature. These observations lead to two possible explanations for the behavior of the ^{1}H NMR spectra. The first one is that paramagnetic species may be present; for that matter those can be easily formed from **2.3** by oxidation or abstraction of a hydrogen atom from solvents. The radical species prefers dimerization at low temperatures as normal radical species. At higher temperatures, the dimers dissociate to paramagnetic monomers, which cause line broadening of the NMR signals. Another is that **2.3** can be thermally accessible to the triplet species. Most closed-shell compounds are in ground state singlet and require high energy (light absorption) for electronic excitation. However, compounds with a small HOMO–LUMO gap are capable of producing the excited singlet or triplet states by supply of low energy (heat). The ground state singlet **2.3** with small E_1^{sum}, *i.e.* a small HOMO–LUMO gap, may be in equiliblium with thermally accessible triplet state, which cause line broadening of the NMR signals.

Comparison of the ^{13}C NMR spectra and the HMO calculations of **2.3** with those of 2,5,9,12-tetra-*tert*-butylacenaphtho[1,2;*k*]fluoranthene **2.4** (Figure 2.3.4) reveals only minor differences in the charge distribution for equivalent carbon atoms. However, ^{1}H-signals at the β^2, C^6, C^{14} positions of **2.3** appear in higher field than those of **2.4**.

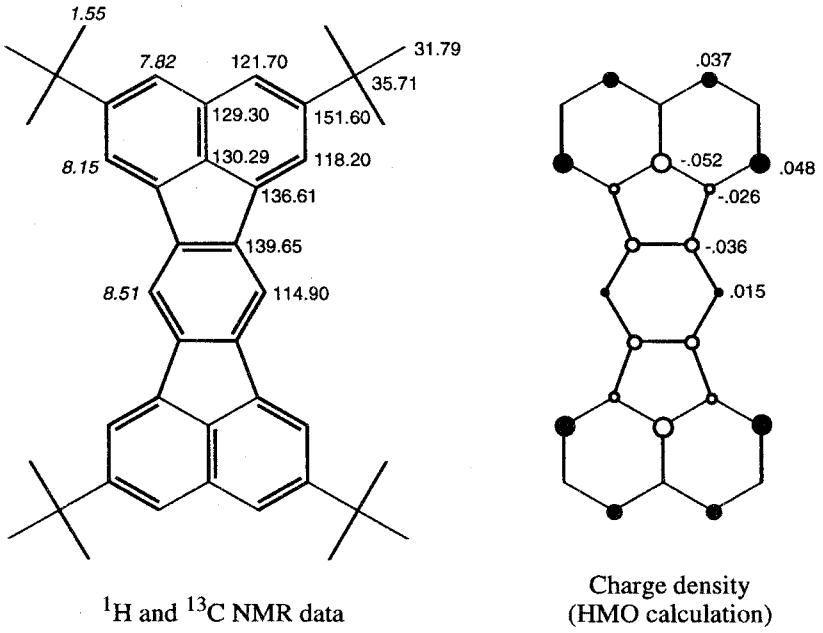

^{1}H and ^{13}C NMR data

Charge density
(HMO calculation)

Figure 2.3.4. NMR data and charge density of **2.4**

It is well established that major effect which governs the ^{13}C chemical shifts of a set of sp^2 carbons is the charge density at the relevant carbon atom. However, proton chemical shifts are sensitive to both charge density and ring current effects. The up field shifts of **2.3** can be attributed to a paramagnetic ring current effect. Ring current calculations [7] indicate that weakly paramagnetic ring current is formed in *s*-indacene unit of **2.3**. In contrast, strongly diamagnetic ring current is formed in two naphthalene and central benzene rings of **2.4** (Figure 2.3.5).

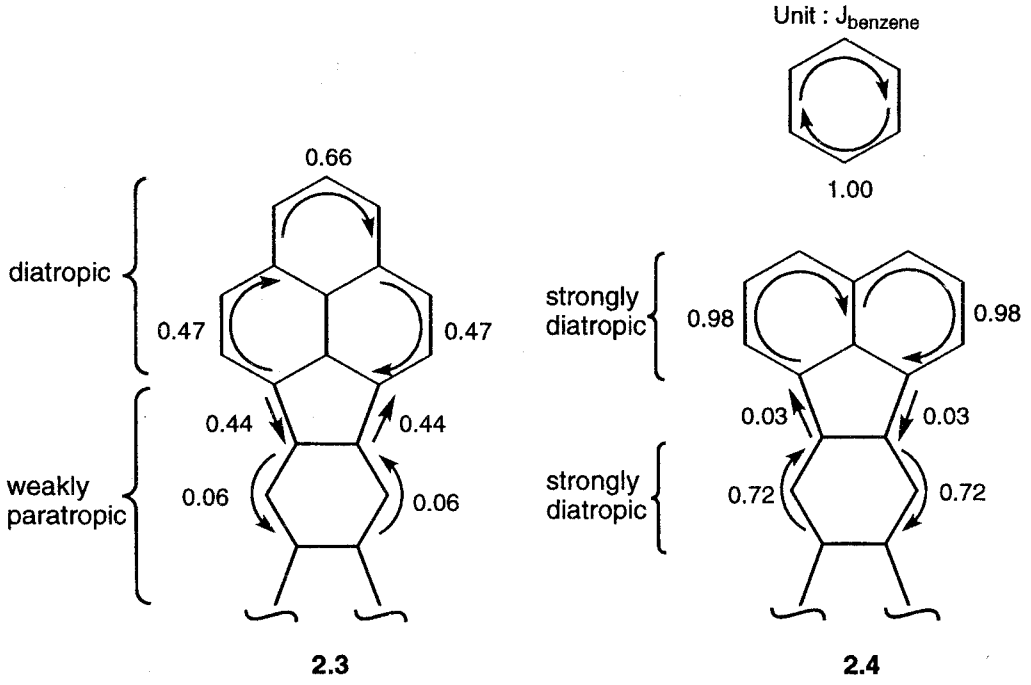

Figure 2.3.5. Ring current calculation of **2.3** and **2.4**

2.3.2 Dication 2.3^{2+}

Dication species **2.3**$^{2+}$ were obtained as a purple solution by dissolving **2.3** in concentrated D_2SO_4 or as purple needles by treating **2.3** with excess $SbCl_5$ in dichloromethane. Figure 2.3.6 shows the aromatic region of the ^1H NMR spectrum of the purple solution. The ^1H and ^{13}C NMR chemical shifts are given in Figure 2.3.7.

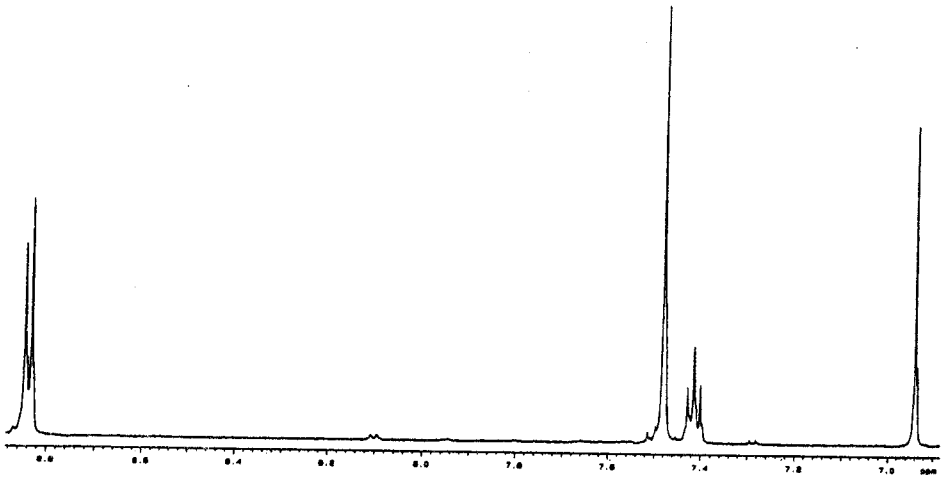

Figure 2.3.6. ^1H NMR spectrum of **2.3**$^{2+}$ in D_2SO_4 at 60 °C.

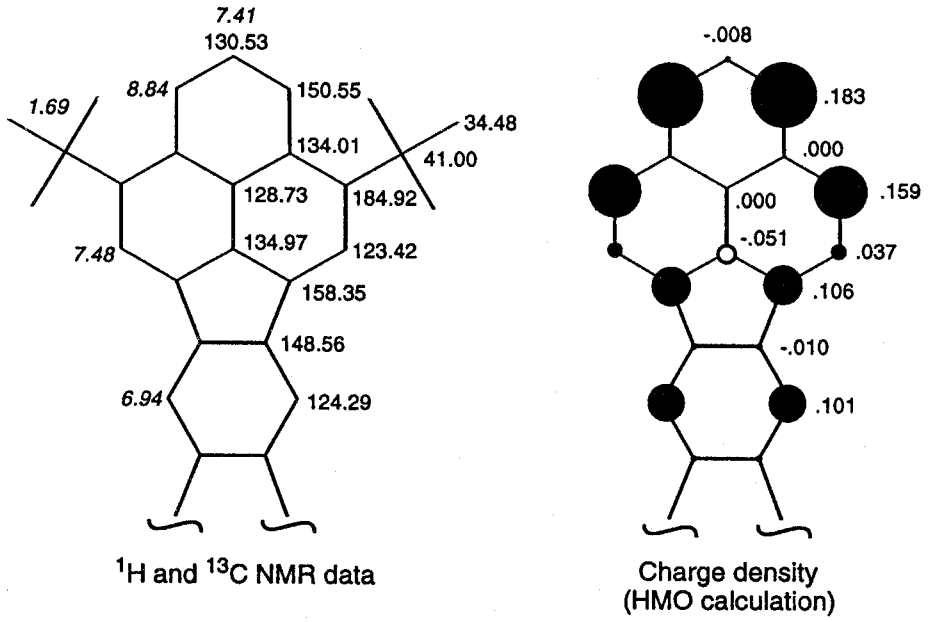

Figure 2.3.7. NMR data and charge density of **2.3**$^{2+}$

The total ^{13}C chemical shift change ($\Sigma\Delta\delta_c$) of sp^2 carbons on going from **2.3** to **2.3**$^{2+}$ is 369 ppm, *i.e.* 185 ppm per electron. This value is in good agreement with the Spiesecke and Schneider correlation predicting a total ^{13}C chemical shift of 160 – 200

ppm per unit of charge.[8] A comparison of the ^{13}C NMR spectra of two phenalenyl units of **2.3**$^{2+}$ with those of phenalenyl cation species [9] reveals only minor differences in the chemical shifts for equivalent carbon atoms except for α^2-carbons of **2.3**$^{2+}$ deshielded by the *tert*-butyl groups. This finding suggests that the positive charge is delocalized mainly over the two phenalenyl units with the charge distributions similar to that in phenalenyl cation species, in accordance with HMO calculations which indicate the total charge density of +1.82 on the two phenalenyl units (Figure 2.3.7). However, $H_{\alpha 1}$, $H_{\beta 1}$, and $H_{\beta 2}$ of **2.3**$^{2+}$ are more shielded than the protons of phenalenyl cation species. The upfield shifts can be related to the formation of paramagnetic ring current. London–McWeeny ring current calculations support the idea that **2.3**$^{2+}$ should show strong and weak paratropism at the central *s*-indacene and the terminal benzene rings, respectively (Figure 2.3.8).

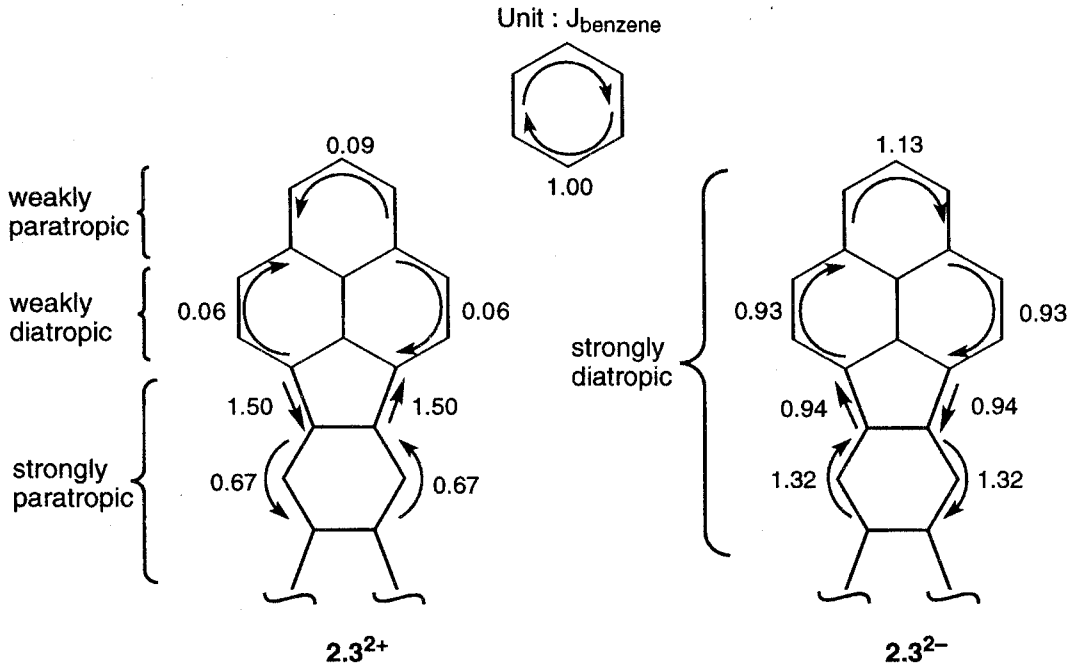

Figure 2.3.8. Ring current calculation of **2.3**$^{2+}$ and **2.3**$^{2-}$

2.3.3 Dianion

Treatment of dihydro compounds **2.8** with a potassium mirror in THF in a sealed degassed tube at –78°C yielded dianion species **2.3**$^{2-}$ as a deep blue solution. Figure 2.3.9 shows the aromatic region of the ^1H NMR spectrum of the blue solution. The ^1H and ^{13}C NMR chemical shifts are given in Figure 2.3.10.

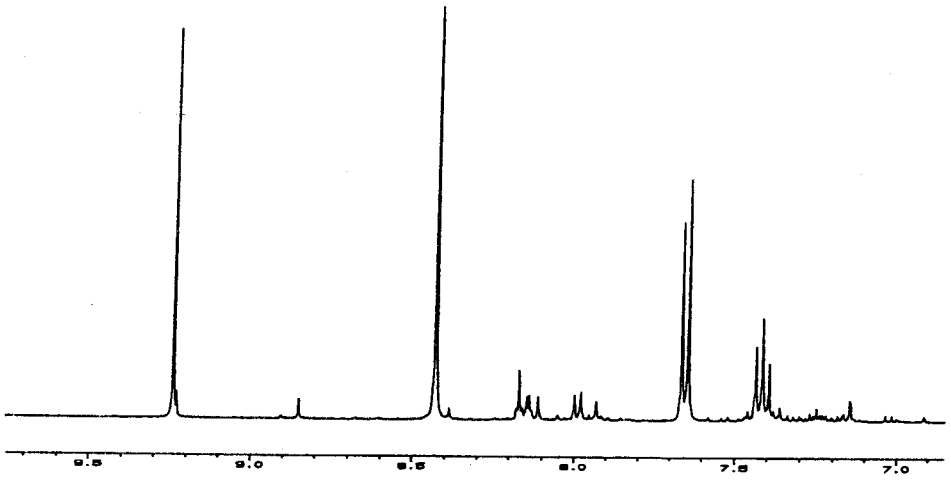

Figure 2.3.9. ^{1}H NMR spectrum of **2.3**$^{2-}$ in THF-d_8 at 30 °C.

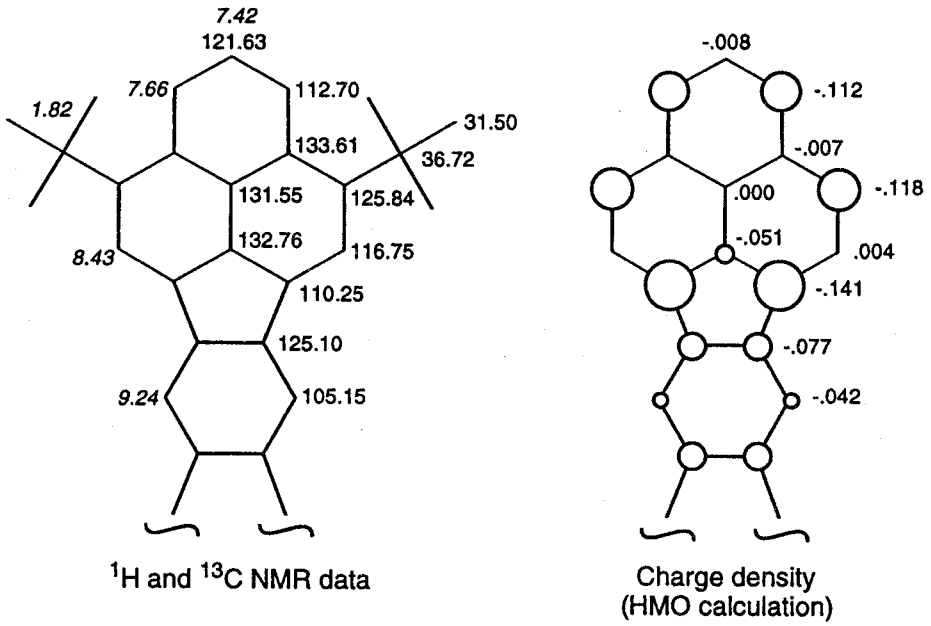

Figure 2.3.10. NMR data and charge density of **2.3**$^{2-}$

The ^{13}C NMR spectrum of dianion **2.3**$^{2-}$ reveals reasonably the dianionic nature with a total upfield shift of 388 ppm (Figure 2.3.10). The ^{13}C chemical shift for sp^2 carbons changes largely at the α^1, α^2, α^3, C^6, and C^{14} positions, but slightly at other positions, on going from **2.3** to **2.3**$^{2-}$. This result is consistent with HMO calculations, which indicate that the LUMO of **2.3** has a NBMO character, possessing coefficients of +0.071 or –0.071 at the α^1, α^2, α^3, C^6, and C^{14} positions, and of zero at other positions (Figure 2.1.2). Despite the shielding effect of the negative charges, all protons appear considerably in downfield region. In particular, the largest downfield shift is observed for H^6 and H^{14}, although C^6 and C^{14} appear in the highest field among the sp^2 carbons

of **2.3**$^{2-}$. It is well established that the ^{13}C chemical shift of a sp^2 carbon is influenced sensitively by the charge density at the carbon atom, but slightly by ring current effects. The ^{13}C NMR spectrum and HMO calculation reveal that the charge densities at C^6 and C^{14} are more negative in **2.3**$^{2-}$ than in **2.3**. These findings clearly suggest that the opposite effect of the diamagnetic deshielding relative to the shielding due to the negative charges is even more significant in **2.3**$^{2-}$. The ring current calculations suggest the formation of a strongly diamagnetic ring current along the periphery of **2.3**$^{2-}$ with the contribution of a peripheral 28C-30π conjugate system [10] (Figure 2.3.8).

Both dication and dianion species are stable at room temperature. On the basis of the HMO calculation, two phenalenyl units have 91% of the total positive charges and 81% of the total negative charges in the dication and dianion states, respectively. This finding suggests large contribution of the type **2.3b** structure to the stability of both doubly charged species.

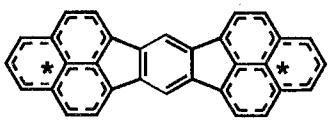

* = + or –

structure **2.3b**

2.4 ESR spectroscopy

2.4.1 Introduction

Because the E_1^{sum} value to estimate the amphotericity of a molecule is the numerical sum of oxidation potential (E_1^{ox}) and reduction potential (E_1^{red}), the electronic states of monocation or monoanion species give important information to develop higher amphotericity. As shown in section 2.3, information for the electronic states of closed–shell compounds such as dication **2.3**$^{2+}$ and dianion **2.3**$^{2-}$ could be obtained from ^{13}C NMR data. In the case of monocation **2.3**$^{(\bullet)(+)}$ and monoanion **2.3**$^{(\bullet)(-)}$, however, the unpaired electron prevents the studies of the electronic states by NMR spectroscopy. The most powerful means to investigate the spin distribution is ESR spectroscopy.

ESR spectra of radical species give hyperfine structures due to the interaction of the unpaired electron with the magnetic nuclei of the radical. In most cases involving hydrocarbon radicals, all of the readily observed hyperfine splitting are caused by protons, since the only abundant isotope of carbon is nonmagnetic. The hyperfine coupling constants $a_{H\mu}$ of a proton is proportional to the π-spin population ρ_μ on the neighboring carbon, known as the McConnell relation.[11]

$$a_{H\mu} = Q \bullet \rho_\mu$$

The proportionality factor Q has a value of 23 – 30 gauss and a negative sign, as shown both by theory and experiment. The most useful and convenient method to estimate a theoretical π-spin population is HMO–McLachlan calculations.[12]

McLachlan has developed a convenient perturbation procedure which is formally equivalent to the CI method, but which uses only HMO quantities plus one additional parameter λ. The formula is

$$\rho_\mu = c_{j,\mu}{}^2 + \lambda \sum_\nu \pi_{\mu,\nu} c_{j,\nu}{}^2$$

μ : the given center
ν : all the remaining center
j : singly occupied orbital ψ_j
$c_{j,\mu}$: molecular orbital coefficient
$\pi_{\mu,\nu}$: HMO atom–atom polarizabilities

The additional parameter λ is usually taken as 1.2, although the absolute magnitudes of negative spin populations calculated with this value are frequently too large.

Phenalenyl radical is known to exhibit a well-resolved ESR spectrum,[13] from which two hyperfine coupling constants are obtained (6.3 G and 1.8 G). In general, only the absolute values of $a_{H\mu}$ can be determined from an ESR spectrum. Theoretical π-spin populations calculated by HMO–McLachlan method (λ = 1.2) are 0.229 at α-position and –0.073 at β-position. Application of the McConnell relation with Q = –27 G gives calculated coupling constants (6.18 G at α-position and –1.97 G at β-position). On the basis of the calculated coupling constants, the experimental coupling constants are assigned ; 6.3 G at α-position and 1.8 G at β-position. These analysis are confirmed by computer simulation of the ESR spectrum. In conclusion, absolute values of π-spin populations for phenalenyl radical are found to be large at α-position and small at β-position.

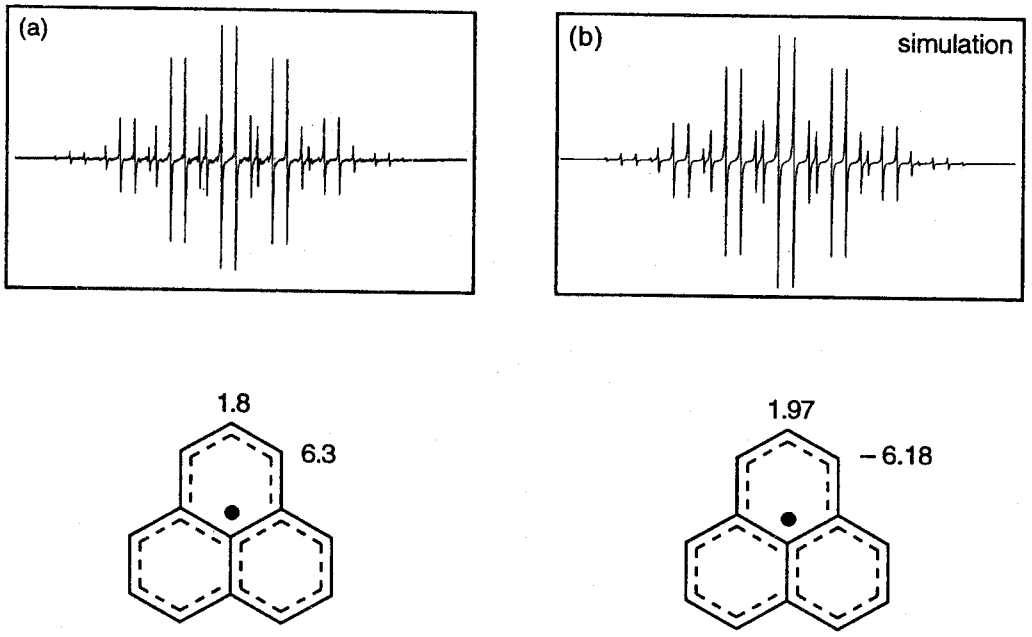

Figure 2.4.1. (a) ESR spectrum of the radical cation of phenalenyl radical in toluene at 240 K and (b) the simulated spectrum.

Thus the information about the electronic states of radical species can be extracted by use of ESR spectroscopy. In section 2.4.2 and 2.4.3, I will discuss the electronic states of **2.3**$^{(\bullet)(+)}$ and **2.3**$^{(\bullet)(-)}$ extracted from the ESR spectra.

2.4.2 Radical cation **2.3**$^{(\bullet)(+)}$

The low first oxidation potential (E_1^{ox}) and the high first reduction potential (E_1^{red}) indicate that TTB-IDPL **2.3** should be easily oxidized to the radical cation **2.3**$^{(\bullet)(+)}$ and reduced to the radical anion **2.3**$^{(\bullet)(-)}$. Furthermore, the reversible redox waves in the cyclic voltammogram for **2.3** suggest both the radical species to be stable.

The reaction of **2.3** with $SbCl_5$ in CH_2Cl_2 generated the radical cation **2.3**$^{(\bullet)(+)}$, which was found to be stable at room temperature and gave rise to the well-resolved ESR spectra as shown in Figure 2.4.2. No detectable changes were observed in the spectra in the range of 213 – 273 K.

The coupling constants of the ring protons are given in Figure 2.4.3 along with the spin density calculated by the HMO–McLachlan method (λ = 1.2). The assignment of the coupling constants is based on the calculated spin density and is confirmed by studies of the radical cation of the 2,10-dideuterated derivative **2.5**. The deuterated compounds were synthesized following Scheme 2.4.1.

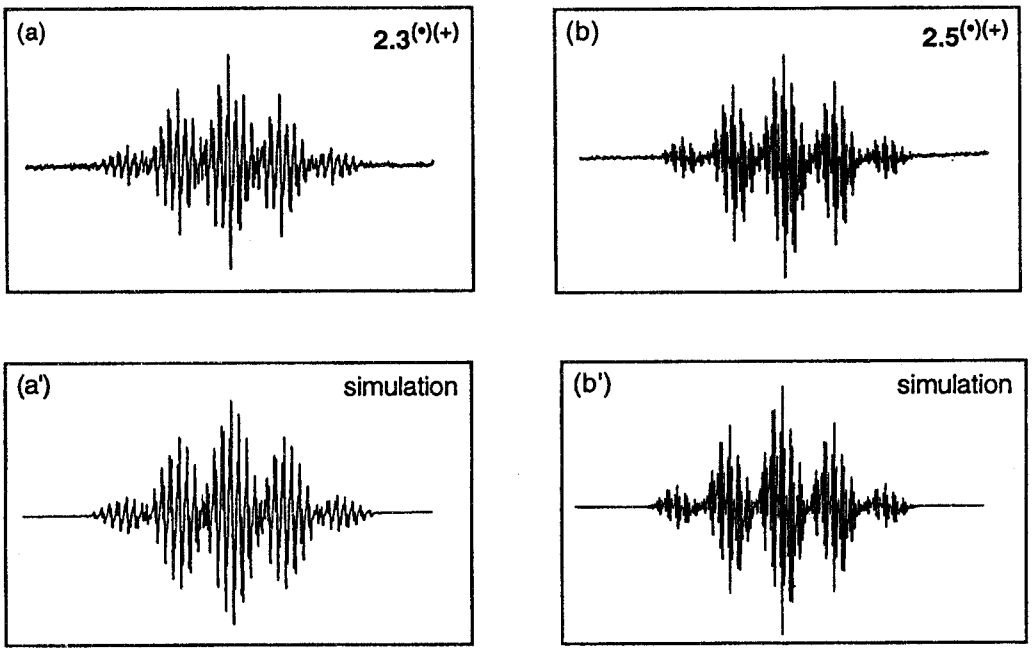

Figure 2.4.2. ESR spectra of (a) the radical cations of **2.3** and (b) deuterated derivative **2.5** generated with $SbCl_5$ in CH_2Cl_2 at - 20 °C, and the correspondig simulated spectra (a') and (b'), respectively.

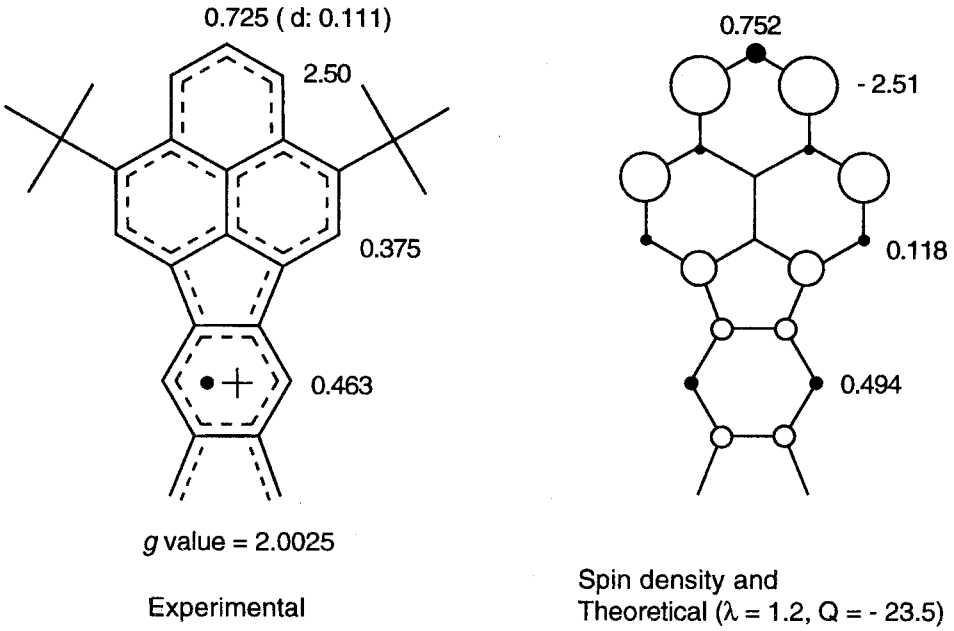

Figure 2.4.3. Experimental and theoretical hyperfine coupling constants (in G) along with spin density of $\mathbf{2.3}^{(\bullet)(+)}$ and $\mathbf{2.5}^{(\bullet)(+)}$. In parentheses, a coupling constant of deuteron. Open-circle and closed-circle represent positive and negative spin density, respectively.

Scheme 2.4.1

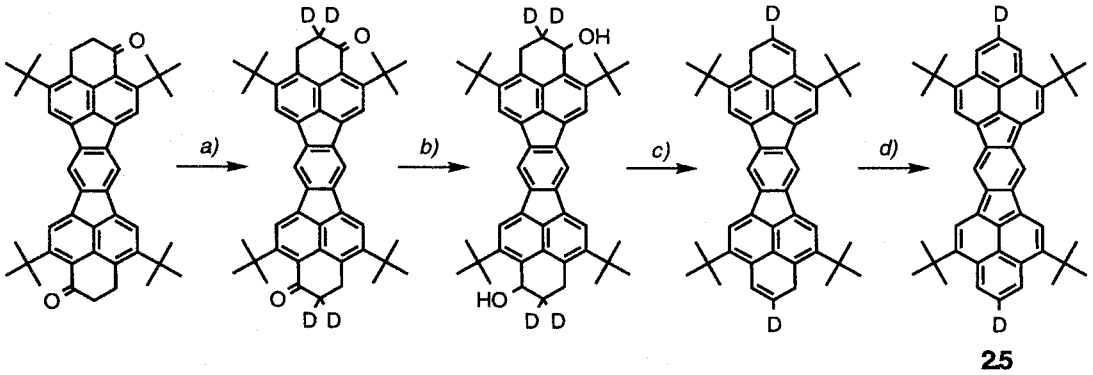

Reaction condition : *a)* CF_3COOD, CH_2Cl_2, rt, 1 d, 87%. *b)* $LiAlH_4$, THF, rt, 2 h, 78%. *c)* *p*-toluenesulfonic acid, benzene, reflux, 5 min, 78%. *d)* *p*-chloranil, benzene, reflux, 1 h.

2.4.3 Radical anion $\mathbf{2.3}^{(\bullet)(-)}$

The radical anion $\mathbf{2.3}^{(\bullet)(-)}$ was obtained by the treatment of **2.3** with a potassium mirror in THF. The radical anion was also stable and gave rise to the well-resolved ESR spectra as shown in Figure 2.4.4. No detectable changes were observed in the spectra in the range of 213 – 273 K.

Figure 2.4.5 shows the hyperfine coupling constants and the calculated spin density of $\mathbf{2.3}^{(\bullet)(-)}$.

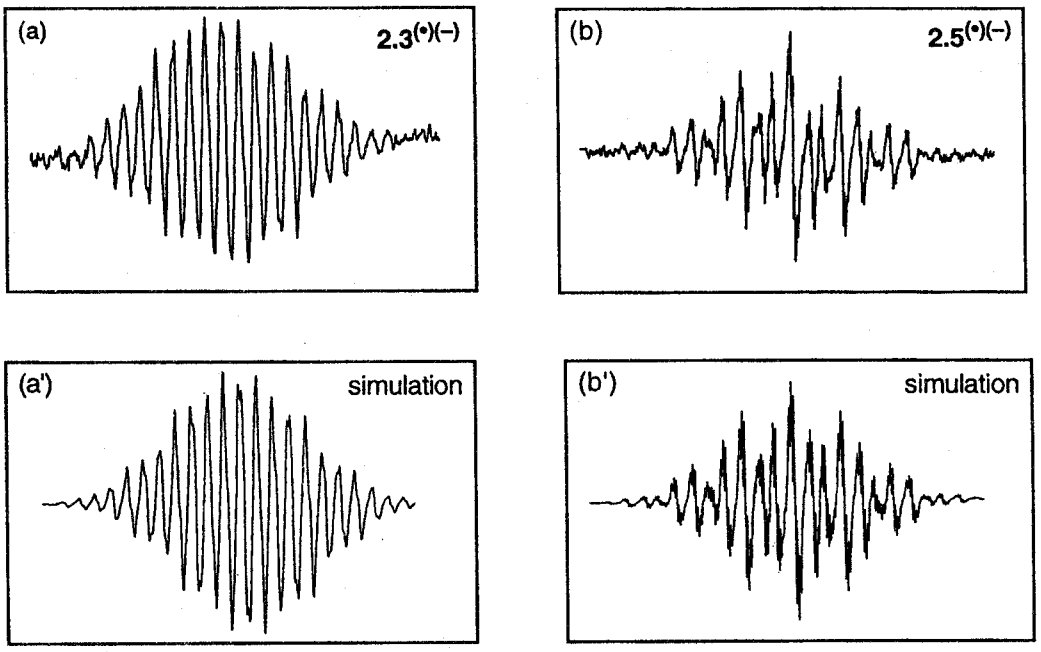

Figure 2.4.4. ESR spectra of (a) the radical anions of **2.3** and (b) deuterated derivative **2.5** generated with K–mirror in THF at - 20 °C, and the correspondig simulated spectra (a') and (b'), respectively.

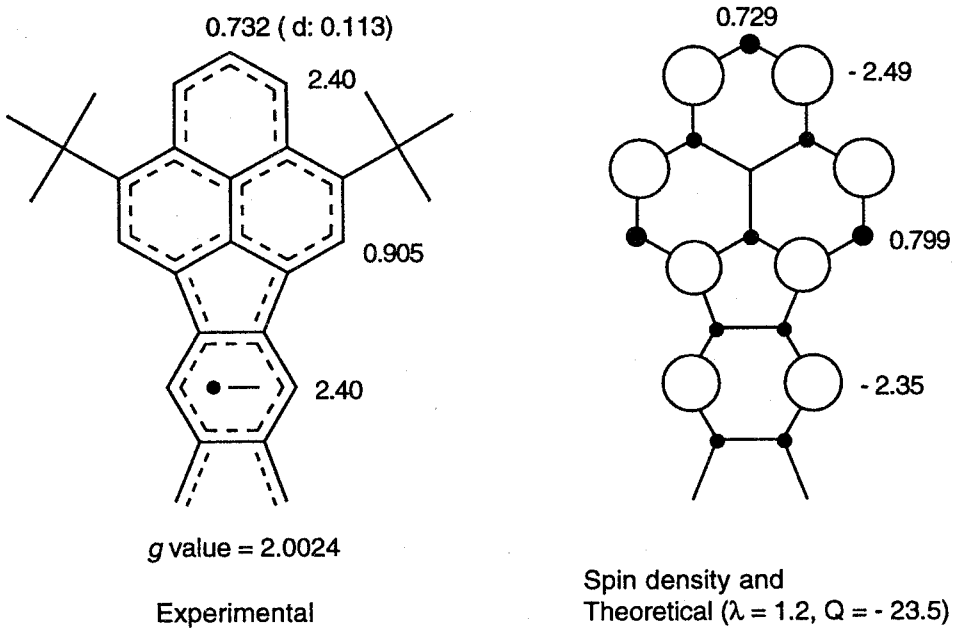

Figure 2.4.5. Experimental and theoretical hyperfine coupling constants (in G) along with spin density of **2.3**$^{(\bullet)(-)}$ and **2.5**$^{(\bullet)(-)}$. In parentheses, a coupling constant of deuteron. Open-circle and closed-circle represent positive and negative spin density, respectively.

The liner relationship between the coupling constants observed and the calculated values supports the idea that the unpaired electron is not confined to one limited

phenalenyl unit but is delocalized over the entire molecule in **2.3**$^{(\bullet)(+)}$ and **2.3**$^{(\bullet)(-)}$. On the basis of the HMO–McLachlan calculations, 86 percent of the π-spin population resides on the two phenalenyl units in both the radical species. These findings suggest that the two phenalenyl units, which cause the delocalization of an unpaired electron over the entire molecule, contribute largely to the stability of both the radical species.

The π-charge distribution of dianion **2.3**$^{2-}$ should relate closely to the π-spin distribution of **2.3**$^{(\bullet)(-)}$, because the unpaired electron in **2.3**$^{(\bullet)(-)}$ occupies, in principle, the same orbital (LUMO of **2.3**) as the two paired electrons in **2.3**$^{2-}$. An analogous statement should hold for the π-spin distribution in the radical cation **2.3**$^{(\bullet)(+)}$ and π-charge distribution in **2.3**$^{2+}$. Comparison of the coupling constants of **2.3**$^{(\bullet)(-)}$ with ^{13}C chemical shift changes on going from **2.3** to **2.3**$^{2-}$ reveals good correlation that these values are large at $C^{\alpha 1}$, C^{6}, and C^{14}, and small at $C^{\beta 1}$ and $C^{\beta 2}$. For **2.3**$^{2+}$ and **2.3**$^{(\bullet)(+)}$, large coupling constants and chemical shift changes are found at $C^{\alpha 1}$ and small ones at $C^{\beta 1}$, $C^{\beta 2}$, C^{6}, and C^{14}. Both the radical species exhibit larger coupling constants at $C^{\alpha 1}$ than those at $C^{\beta 1}$ and $C^{\beta 2}$ in the two phenalenyl units. The similar π-spin distribution pattern is found in phenalenyl radical species exhibiting larger (6.5 G) and smaller (1.8 G) coupling constants at α and β position, respectively. Futhermore, as shown in section 2.3.2, the charge distributions in phenalenyl units of **2.3**$^{2+}$ are similar to that of phenalenyl cation. These similarities support the idea that HOMO of **2.3** retain a NBMO character to some extent. On the other hand, the LUMO of **2.3** has a purely NBMO character. Thus the small E_1^{sum} value of **2.3** can be attributed to the NBMO character of the frontier orbitals (HOMO and LUMO) of **2.3**.

2.4.4 Neutral 2.3

As described in section 2.3.1, the toluene solution of neutral **2.3** gave rise to weak ESR signals (Figure 2.4.6). The species to give this ESR spectrum was unidentifiable, but should be generated by oxidation or hydrogen atom abstraction from solvents. Although the solid **2.3** also gave the ESR signal, the spectral width was nearly 10 times larger than that observed in the solution. The spectrum can be regarded as typical of a triplet state and had zero-field parameter of $D = 96$ G and $E \leq 2$ G.

The following will describe our way of finding the reason why one paramagnetic compound was observed in solution and another in the solid state. The species to give the ESR spectrum in the solution should be a monoradical resulting from oxidation or hydrogen atom abstraction from the solvent by the reactive thermally excited triplet state. The triplet spectrum is generally broadened by fast relaxation in solutions. In the solid state, the doublet impurities gave an intence and narrow peak in the center of the spectrum, whereas the wider signal can be easily distinguishable, which was triplet signal observed at the wings of the free-radical signal.

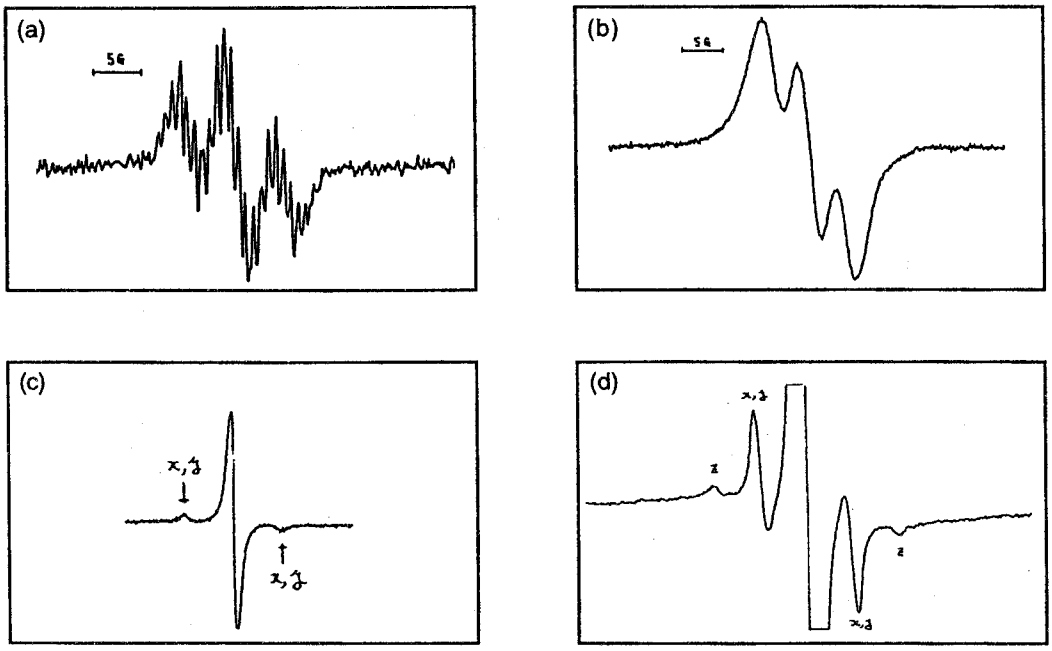

Figure 2.4.6 ESR spectra of doublet species at room temperature in (a) toluene solution and (b) solid state. Triplet signal in solid state at 130 °C with (c) low and (d) high gain.

These pieces of behavior are typical of a biradicaloid. The designation *biradicaloid* asserts that a given molecular structure has two approximately nonbonding electronic configuration(s) in the ground state.[14] Biradicaloids are highly reactive compounds exhibiting a strong paramagnetic shift in the ^{1}H NMR signals and a high propensity toward both oxdation and reduction. Such properties are characteristic for compounds with a small energy gap between the frontier orbitals. Kolc and Michl [15] studied extensively pleiadene and several of its derivatives. Pleiadene can be written with the Kekulé structure or as the biradicaloid canonical structure. The actual molecule is obtained as a highly reactive hydrocarbon which can be only studied at low temperatures frozen in a glass and which dimerizes at normal temperatures. Such behavior is consistent with MO calculations indicating a small HOMO–LUMO gap. Chichibabin's hydrocarbon [16] can also be written in quinoidal or diradical form. Although this compound is so stable as to give the green single-crystal with metallic luster,[16b] the blue-violet solution is sensitive to air.

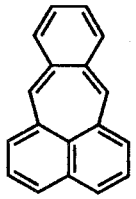

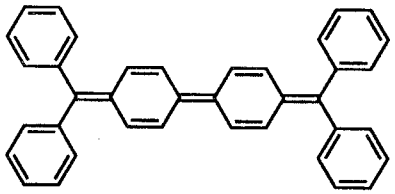

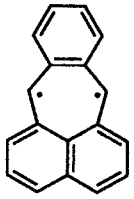

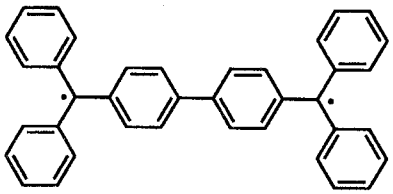

pleiadene

chichibabin's hydrocarbon

The zero-field parameter, D, provides a measure of the average distance between the unpaired spins in the triplet, whereas the other parameter, E, reflects the deviation of the wave function from 3-fold or higher symmetry. These quantities can be calculated using eq (1) and (2),[17] where the brackets are averages over the electronic wave function.

$$D = 0.75g^2\beta^2\langle(r^2 - 3z^2)/r^5\rangle \quad (1)$$

$$E = 0.75g^2\beta^2\langle(y^2 - x^2)/r^5\rangle \quad (2)$$

The average distance between the two interacting spins in **2.3** could be estimated from D to be 6.6 Å,[18] which was smaller than the distance between the center of phenalenyl unit (9.5 Å). This finding suggests that an unpaired electron is not 'localized' on a phenalenyl unit, but can delocalize on the central benzene and another phenalenyl unit.

Unfortunately, the forbidden $\Delta M_S = \pm 2$ half-field absorption could not be observed. A triplet-state signal at half field is known not to be observable for large separation of two electrons.[19] The variation of the signal intensity of the triplet with temperature indicated that the triplet is a thermally excited state. The signal intensity, I, was plotted against temperature in Figure 2.4.7.

A generated least-squares computer program led to a best fit of expression (3) [20]

$$I \propto 1/\{T[3 + \exp(J/k_bT)]\} \quad (3)$$

to the data with $J = 4.66 \pm 0.08$ kcal/mol, which is the energy separation between the ground singlet state and the excited triplet.

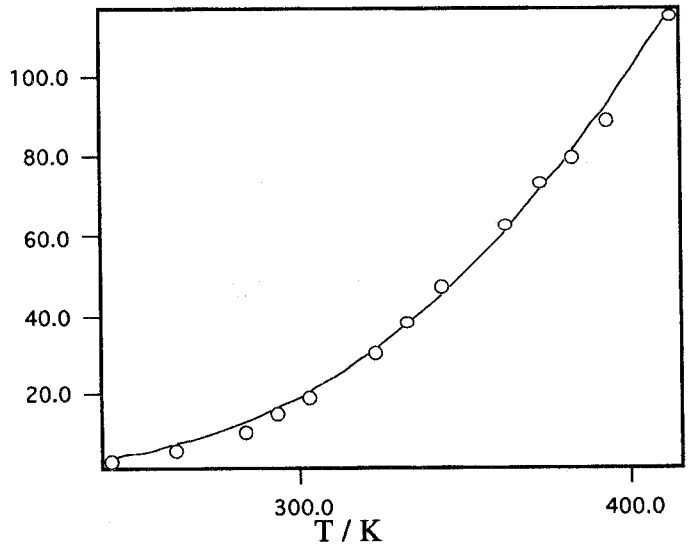

Figure 2.4.7. Temperature dependence of the spectral intensity of the triplet. The solid line is from eq (3).

2.5 UV/Vis/NIR

2.5.1 Neutrtal ***2.3***

Although all precursors for TTB-IDPL **2.3** showed yellow color, dehydration of the dihydro derivatives caused a dramatic change of the color. The solution of **2.3** shows a green color. The deep color is apparently responsible for the small HOMO–LUMO gap of **2.3**. As the HOMO–LUMO energy difference decreases, so also does the spectral excitation energy; thus the absorption band would be shifted to longer wavelength. Figure 2.5.1 shows the electronic absorption spectra of the five redox states of **2.3**, while Table 2.5.1 lists the wavelengths of the band maxima.

Table 2.5.1. Maxima, λ_{max} (in nm) (ε, $cm^{-1}M^{-1}$), of electronic bands for the five redox states of **2.3**

$\mathbf{2.3^{2+}}$	$\mathbf{2.3^{(\bullet)(+)}}$	**2.3**	$\mathbf{2.3^{(\bullet)(-)}}$	$\mathbf{2.3^{2-}}$
330 (76200)	351	342 (69100)	320	294
378 (22400)	393	352 (75100)	372	330
401 (21100)	660	370 (124000)	430	376
534 (35700)	683	405 (7900)	596	456
578 (61200)	1440	448 (7500)	630	582
620 – 720 [a]	1832	687 (16000)	1248	660
		755 (369000)	1288	
			1488	
			1546	

[a] weak shoulder absorption

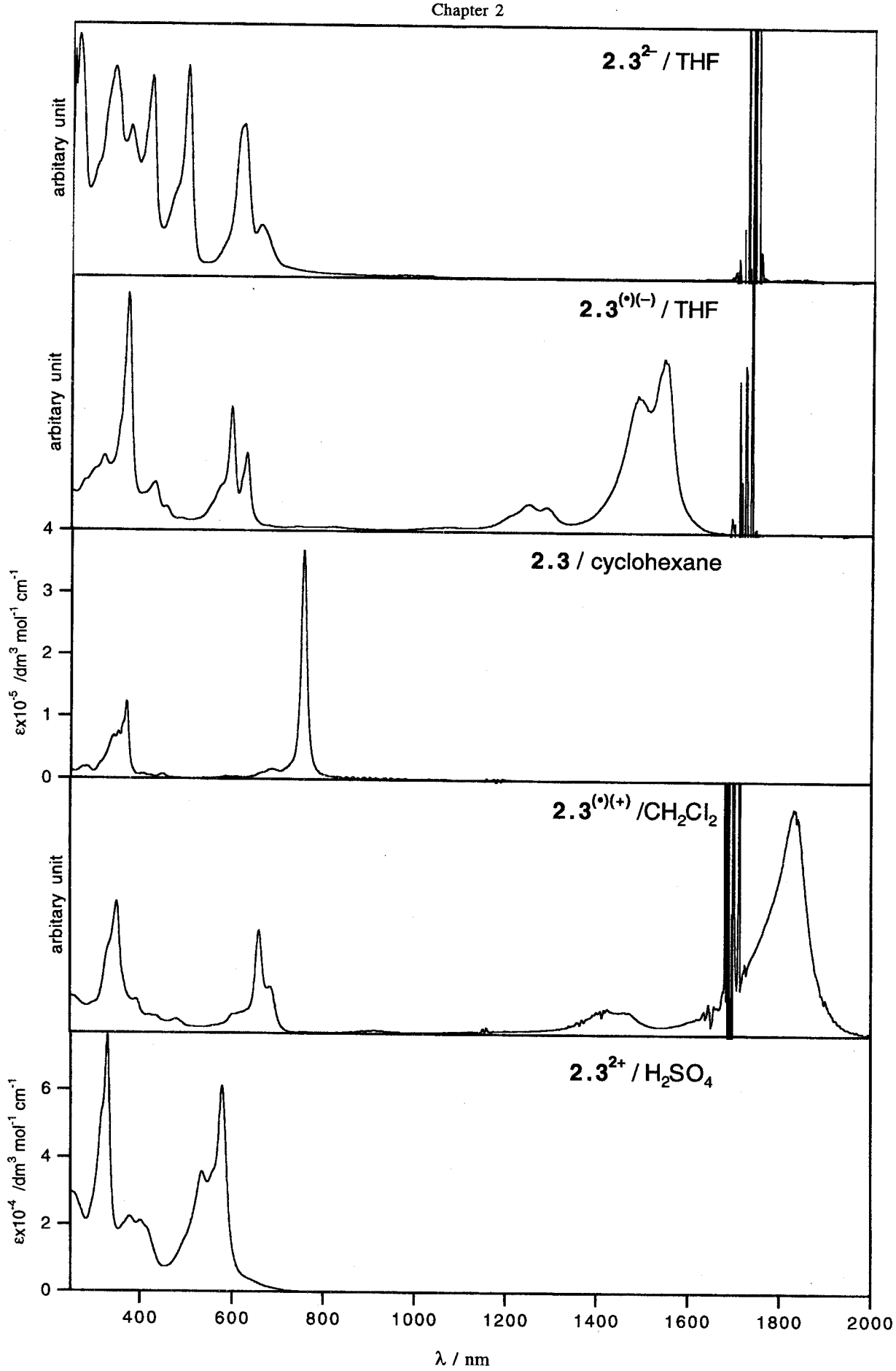

Figure 2.5.1. Electronic absorption spectra of the five redox states of **2.3**

The green color of **2.3** can be readily ascribed to a highly intense band at 755 nm. Another intense band at 350 – 370 nm can not contribute to the color because of the high transition energy (UV region). In order to assign the electronic bands to transitions between orbitals, MO calculations by the INDO/S CI method were performed (Table 2.5.2). In each case, the ten highest occupied and ten lowest unoccupied orbitals were used for configuration interaction.

Table 2.5.2. Selected electronic transition data for five redox states of **2.3** calculated by the INDO/S CI method and assignments of the observed electronic bands.

	theoretical				experimental
	symmetry label [d]	ΔE, eV	oscillator strength	substantial contribution [a], %	λ, nm; ΔE,eV
2.3^{2+}	B_{2u} (y)	1.60	0.02	a_u (ψ_{16}), ← b_{2g} (ψ_{15}), 90	*b*
2.3$^{(\bullet)(+)}$	B_{3u} (x)	0.65	0.41	b_{3g} (ψ_{17}) ← a_u (ψ_{16}), 91	1832; 0.68
2.3	B_{1g}	1.08	0.00	b_{3g} (ψ_{17}) ← b_{2g} (ψ_{15}), 94	1030; 1.20[c]
	B_{3u} (x)	1.65	2.27	b_{3g} (ψ_{17}) ← a_u (ψ_{16}), 93	755; 1.64
2.3$^{(\bullet)(-)}$	B_{3u} (x)	0.73	0.32	b_{3g} (ψ_{17}) ← a_u (ψ_{16}), 84 a_u (ψ_{18}) ← b_{3g} (ψ_{17}), 6	1546; 0.80
2.3^{2-}	B_{3u} (x)	2.44	1.37	a_u (ψ_{18}) ← b_{3g} (ψ_{17}), 84 b_{3g} (ψ_{20}) ← a_u (ψ_{16}), 10	660?; 1.88?

[a] In parentheses, the molecular orbitals calculated by the HMO method. See Figure 2.2. [b] Could not be assigned due to the weak and broad peaks. [c] Observed in high concentration of benzene solution. [d] In parentheses, the direction of the induced transition dipole. The choice of the axes in D_{2h} symmetry is specified in Fiugre 2.1.2.

Figure 2.5.2 presents schematically the calculated SCF energy levels of the six relevant highest occupied or lowest unoccupied orbitals for the five redox states of **2.3**. On the basis of the calculation, the intense band at 755 nm could be assigned to a symmetry-allowed B_{3u} transition, which is HOMO → LUMO excitation. In addition to this long-wavelength bands, the INDO/S calculations predict a symmetry-forbidden transition in near-infrared (NIR) region. The low solubility of **2.3** in cyclohexane prevents the detection of predicted weak bands in NIR region. However, the NIR bands could be observed in high concentration of benzene solution (Figure 2.5.3).

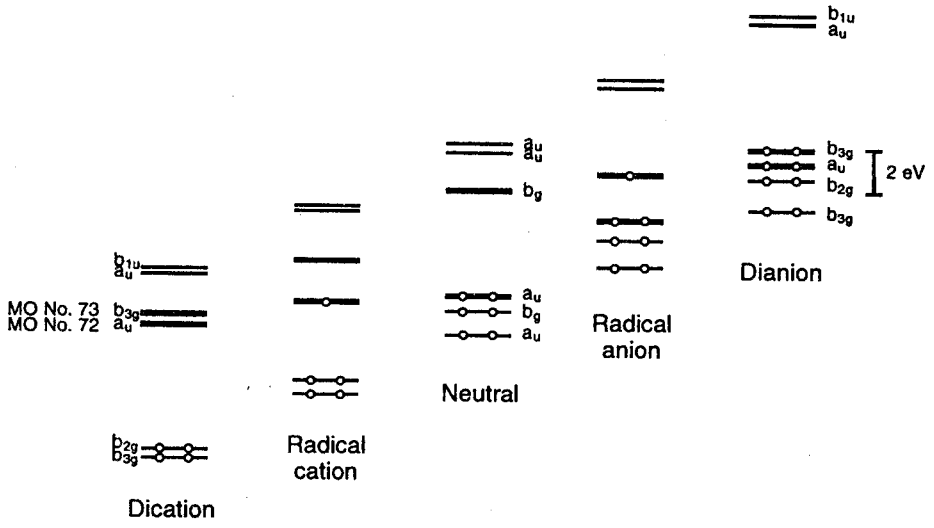

Figure 2.5.2. Energy levels of several occupied and unoccupied MOs in the five redox stages of IDPL **2.1**, as calculated by the MOPAC6/PM3 method. The optimized structures are in C_{2h} symmetry for neutral state and in D_{2h} symmetry for other states. The bold lines represent HOMO and LUMO of neutral state.

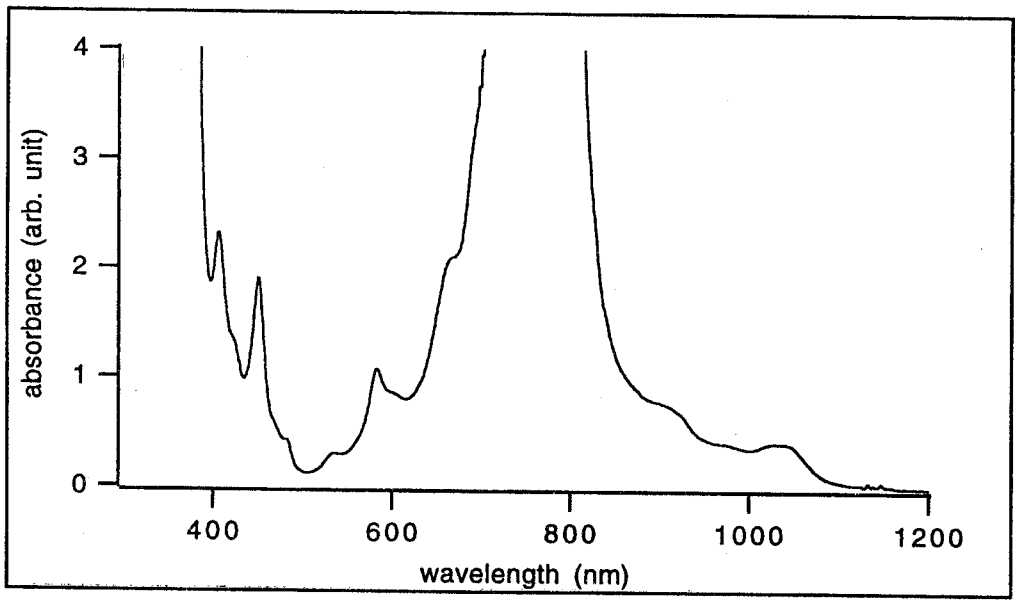

Figure 2.5.3. Electronic spectrum of **2.3** in high concentration of benzene solution

The calculations predict that NHOMO–LUMO transition should contribute largely to the longest wavelength absorption. Clearly, the transition with larger energy gap (NHOMO–LUMO) appeared at longer-wavelength region than that with smaller energy gap (HOMO–LUMO). In order to remove this discrepancy, the electron correlation should be considered. When the spectral excitation energy is described by a transition from MO ψ_a to MO ψ_b, the singlet-singlet excitation energy ΔE_{ab} is, to a close approximation, given by eq (2-1).[21]

$$\Delta E_{ab} = \varepsilon_b - \varepsilon_a - J_{ab} + 2K_{ab} \quad (2\text{-}1)$$

where $(\varepsilon_b - \varepsilon_a)$ is the energy difference between the ψ_b andψ_a, J_{ab} is the molecular Coulomb repulsion integral, and K_{ab} is the exchange integral. The exchange integral K_{ab} is a measure of the repulsion of the overlap charge density $\psi_a(1)\bullet\psi_b(1)$ with identically distributed overlap charge density $\psi_a(2)\bullet\psi_b(2)$. If the two orbitals, ψ_a and ψ_b, spread over different region of space, their overlap density will be small and then K_{ab} can hardly be large. The HMO calculations indicate that HOMO and LUMO of **2.3** occupy similar region in space, and $K_{HOMO,LUMO}$ should be relatively large. In contrast, NHOMO and LUMO are localized largely in different parts of space. As a result, the overlap density as well as $K_{NHOMO,LUMO}$ should be quite small. Small $K_{NHOMO,LUMO}$ values lead to the longer-wavelength absorption. [22]

This assumption was borne out by the weak intensity of the NIR transition. The intensity of a transition is proportional to the square of the transition dipole moment of the overlap density $\psi_a(1)\bullet\psi_b(1)$. The small overlap $\psi_{HOMO}(1)\bullet\psi_{LUMO}(1)$ of **2.3** should be responsible for the small transition dipole moment, and the NIR transition should be fairly weak.

The green compound **2.3** shows no emission spectra at >755 nm, although the large extinction coefficient for absorption at 755 nm suggests a large rate constant for emission. Emission is usually known to occur from S_1 state for most organic molecules (Kasha's rule).[23] For **2.3**, the absorption at 755 nm produces not S_1 but S_2 excited state, which undergo rapid $S_2 \rightarrow S_1$ internal conversion. Thus the absence of emission supports the presence of S_1 state at > 755 nm.

2.5.2 Radical cation ***2.3***$^{(\bullet)(+)}$ *and radical anion* ***2.3***$^{(\bullet)(-)}$

Oxidation or reduction of aromatic hydrocarbons such as naphthalene and anthracene results in formation of a deeply colored solution. The following statements are accepted for these observations. The species responsible for these colors are undoubtedly radical ions. Additional long-wavelength bands, which are not observed for the neutral aromatic compounds, are due to the transition in which singly occupied MO (SOMO) participates; SOMO → LUMO, HOMO → SOMO excitation, etc. However, when green compound **2.3** was oxidized or reduced with $SbCl_5$ or K mirror, the color of the solution did not change dramatically. The resulting green and greenish blue color of the solution containing **2.3**$^{(\bullet)(+)}$ and **2.3**$^{(\bullet)(-)}$ can be reasonably attributed to absorption bands at $\lambda \leq 683$ nm and 630 nm, respectively. In addition to these long-wavelength absorption, **2.3**$^{(\bullet)(+)}$ and **2.3**$^{(\bullet)(-)}$ gave the lower energy bands in near-infrared (NIR) region (Figure 2.5.1). The INDO/S calculations indicate that the NIR band of **2.3**$^{(\bullet)(+)}$ and **2.3**$^{(\bullet)(-)}$ should be due to the excited configuration corresponding

to b_{3g} (ψ_{17}) ← a_u (ψ_{16}) excitation (symmetry-allowed B_{3u} transition), which is SOMO → LUMO excitation for **2.3**$^{(\bullet)(+)}$ and HOMO → SOMO for **2.3**$^{(\bullet)(-)}$ (Table 2). These low energy transitions in the NIR region implies the small HOMO–LUMO gap of **2.3**, because the MO ψ_{16} and ψ_{17} correspond to the HOMO and the LUMO of **2.3**, respectively. This may well be because a green colored neutral hydrocarbon, hexacene, also gives a NIR band in the radical anion state due to HOMO → SOMO excitation.[24]

In NIR region, intramolecular charge-transfer bands are commonly observed. For example, bis(TTF) radical cations [25] and polyacene diquinone radical anions [26] exhibited a broad absorption band in NIR region.

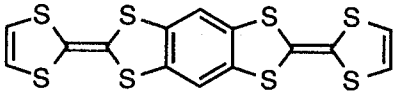

bis TTF

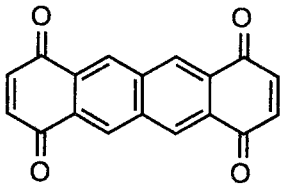

polyacene diquinone

These compounds are thought to be mixed-valence species (class II) [27] containing two weakly interacting redox sites and an odd electron localized on a redox site. However, the sharpness and the vibrational structure of the NIR bands for **2.3**$^{(\bullet)(+)}$ and **2.3**$^{(\bullet)(-)}$ are incompatible with the characteristics of a charge-transfer band. The intensity of the NIR bands follows Beer's law over the concentration range of 10^{-5} to 10^{-4}, indicating that these absorption are not due to a CT transition in any aggregated forms of these radicals. As mentioned above, the ESR studies suggest the delocalization of the charge and the spin over the whole of the molecule. Furthermore, the cyclic voltammogram of **2.3** shows four one-electron waves with quite more largely separate values for the corresponding half-wave potentials ($E_2^{ox} - E_1^{ox} = 0.35$V, $E_1^{red} - E_2^{red} = 0.58$V) than those of class II species. In accordance with the classification of mixed-valence species, **2.3**$^{(\bullet)(+)}$ and **2.3**$^{(\bullet)(-)}$ can be regarded as class III species containing two strongly interacting redox sites, phenalenyl units. Completely delocalized molecules should be placed in the class III category. These considerations support the idea that formula B is a better description for the singly charged paramagnetic species, **2.3**$^{(\bullet)(+)}$ and **2.3**$^{(\bullet)(-)}$, than formula A.

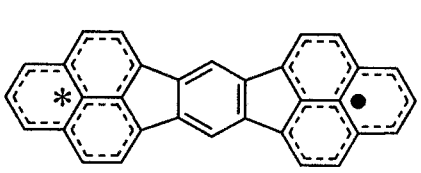

* = + or –

A

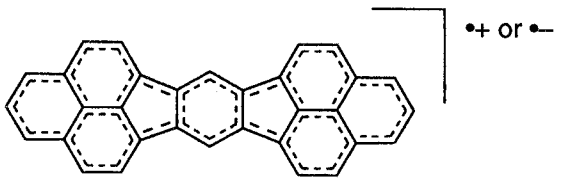

•+ or •–

B

2.5.3 Dication 2.3^{2+} and dianion 2.3^{2-}

The absorption maxima of $\mathbf{2.3}^{2+}$ and $\mathbf{2.3}^{2-}$ appear at shorter wavelength than those of other redox states of **2.3** (Figure 2.5.1). In particular, the absorption of $\mathbf{2.3}^{2-}$ terminates at the shortest-wavelength. This finding suggests the large HOMO–LUMO gap for $\mathbf{2.3}^{2-}$, which is consistent with the HMO calculations. Because a large HOMO–LUMO gap causes a small contribution of a paramagnetic ring current effect to the molecule in question,[28] the hypsochromic shifts of $\mathbf{2.3}^{2-}$ support the idea that low-field shifts of ^{1}H NMR spectrum for $\mathbf{2.3}^{2-}$ should be caused by a strong diamagnetic ring current effect.

The assignment of the first absorption bands in $\mathbf{2.3}^{2+}$ and $\mathbf{2.3}^{2-}$ remains still questionable. For $\mathbf{2.3}^{2+}$, the weak transitions were observed at 620 – 720 nm, but the absorption maxima could not be determined due to the broadness and the weakness of the absorption. The INDO/S calculations predict the symmetry-forbidden HOMO–LUMO transition at 775 nm, which may correspond to the absorption at 620 – 720 nm.

2.6 X-ray crystallography

2.6.1 TTB-IDPL 2.3

Cryatals suitable for X-ray diffraction were successfully obtained as crystals of *m*-difluorobenzene solvates by recrystallization from a *m*-difluorobenzene solution at room temperature. The crystal selected for X-ray analysis was 0.2 x 0.3 x 0.3 mm in size and sealed in a glass capillary containing glass fibers impregnated with *m*-difluorobenzene. The compound was found to crystallize in space group C_{mca} with four molecules in the unit cell. The atomic parameters are given in Table 2.6.1 and 2.6.2.

The crystal structure of **2.3** determined at room temperature shows effective D_{2h} symmetry (Figure 2.6.1), which is consistent with the presence of only five ^{1}H NMR signals even at –60 °C. In comparison with 7,14-di-*n*-propylacenaphto[1,2-*k*]fluoranthene, [29] **2.3** gives shorter bond length between C2 and C3 by 0.032 – 0.033 Å. This must be due, at least in part, to increased π-bonding between C2 and C3. In the canonical forms, no double bonds appear between naphthalene units and a benzene unit in acenaphthofluoranthene, while **2.3** retains double bonds in C2-C3 bonds. The increased π-bonding is also supported by the simple HMO calculations indicating a larger π-bond order (0.457 for **2.3**; 0.402 for acenaphthofluoranthene).

The large degree of π-bonding between C2 and C3 of **2.3** supports the idea that two phenalenyl units should not function independently but largery interact with each other. This is consistent with only a very small contribution from the type **2.3c** structure.

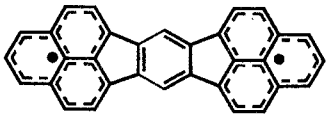

2.3c

Bond lengths and angles of *s*-indacene unit in **2.3** are found to be similar to those of tetra-*tert*-butyl-*s*-indacene. [30]

The packing diagram in Figure 2.6.2 reveals that the molecules **2.3** form "lattices" with cavities large enough to accommodate two molecules of *m*-difuorobenzene. The tortional angle between two molecules **2.3** are 78°.

(a)

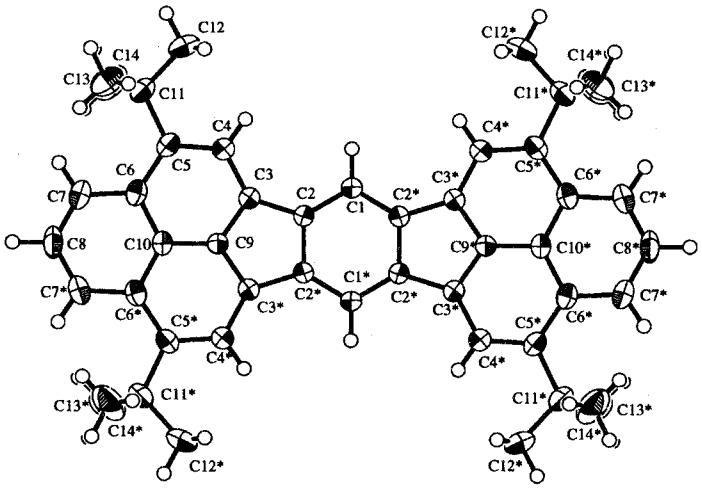

(b)

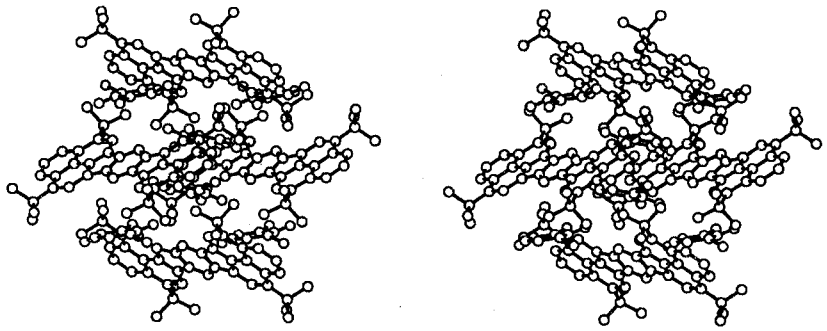

(c)

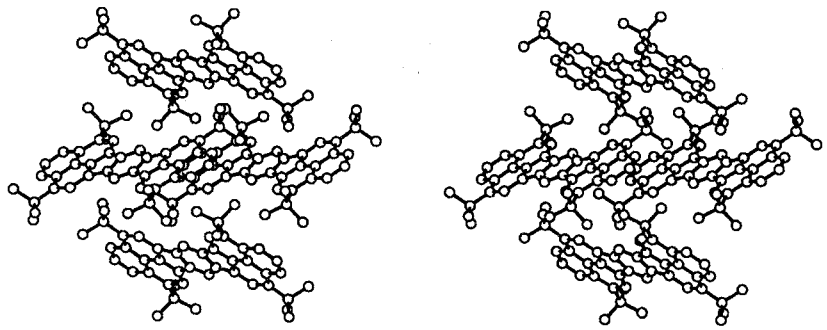

Figure 2.6.1. (a) The moleculer structure of **2.3**, (b) the stereoscopic view of the molecular packing with solvent, (c) and the molecular packing without solvent. Displacement ellipsoids are drawn at the 50% probability level.

(a)

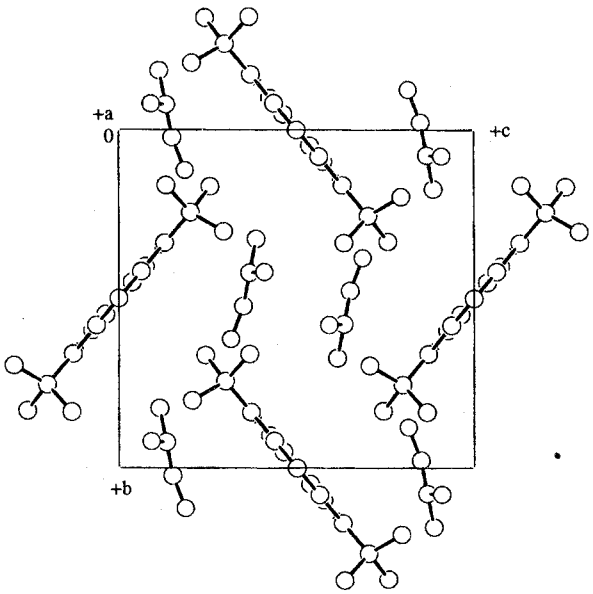

(b)

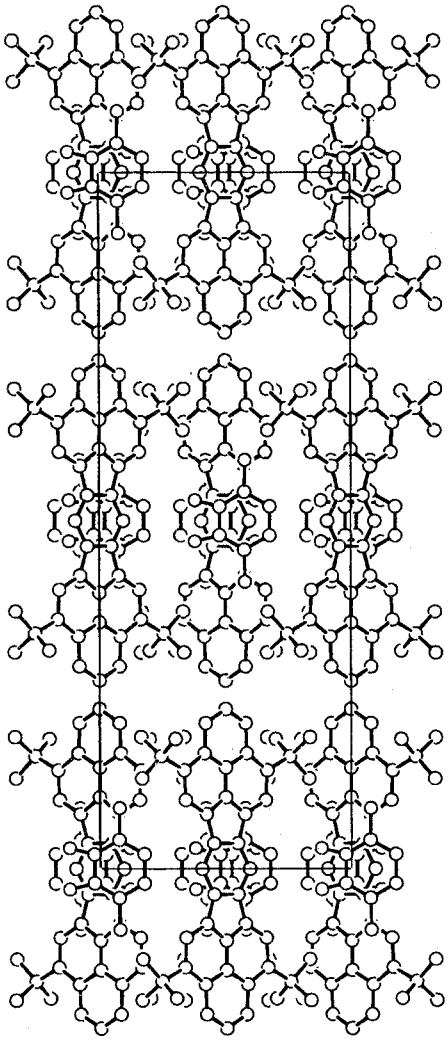

Figure 2.6.2. (a) The molecular packing of **2.3** in the *bc*-plane, (b) the crystal structure of **2.3** along the *c*-axis.

Table 2.6.1. Experimental X-ray data of **2.3**.

Crystal data

$C_{60}H_{54}F_4$	Mo$K\alpha$ radiation
$M_r = 851.08$	$\lambda = 0.71069$ Å
Orthorhombic	Cell parameters from 25 reflections
C_{mca}	$\theta = 27.7$–$29.8°$
$a = 32.602(3)$ Å	$\mu = 0.079$ mm^{-1}
$b = 11.768(3)$ Å	$T = 296$ K
$c = 12.199(3)$ Å	Prismatic
$V = 4680(2)$ Å^3	0.20 x 0.30 x 0.30 mm
$Z = 4$	Green
$D_x = 1.208$ Mg m^{-3}	

Data collection

Rigaku AFC7R diffractometer	1163 observed reflections $[I > 3.00\sigma(I)]$
$\omega/2\theta$ scans	$2\theta_{max} = 55.0°$
Absorption correction: refined from ΔF	$h = 0 \rightarrow 15$
3002 measured reflections	$k = 0 \rightarrow 41$
3001 independent reflections	$l = 0 \rightarrow 15$
	3 standard reflections monitored every 150 reflections
	intensity decay: –0.51%

Refinement

Refinement on F	$(\Delta/\sigma)_{max} = 0.06$
$R = 0.054$	$\Delta\rho_{max} = 0.15$ e Å^{-3}
$wR = 0.057$	$\Delta\rho_{min} = -0.29$ e Å^{-3}
$S = 2.14$	Extinction correction: none
3002 reflections	Atomic scattering factors from *International Tables for X-ray crystallograpy* (1974, Vol. IV)
174 parameters	
$w = 1/\sigma^2(F_o)$	

Table 2.6.2. Fractional atomic coordinates and equivalent isotropic displacement parameters (Å^2) of **2.3**.

$B_{eq} = (8\pi^2/3)(U_{11}(aa^*)^2 + U_{22}(bb^*)^2 + U_{33}(cc^*)^2 + 2U_{12}aa^*bb^*\cos\gamma + 2U_{13}aa^*cc^*\cos\beta + 2U_{23}bb^*cc^*\cos\alpha)$

	x	y	z	B_{eq}
F(1)	0.0295(2)	–0.1197(5)	0.8146(6)	11.1(2)
F(2)	0.0876(2)	0.0779(7)	0.9089(8)	14.7(3)
C(1)	0.0000	0.0945(4)	0.5743(4)	2.6(1)
C(2)	0.03668(9)	0.0474(2)	0.5371(2)	2.47(6)
C(3)	0.07908(9)	0.0762(3)	0.5598(2)	2.54(7)
C(4)	0.09921(10)	0.1585(3)	0.6234(3)	3.05(8)
C(5)	0.14180(9)	0.1643(3)	0.6283(3)	2.95(8)
C(6)	0.16620(9)	0.0836(3)	0.5659(3)	2.83(7)
C(7)	0.20944(10)	0.0793(3)	0.5631(3)	3.70(9)
C(8)	0.2296(2)	0.0000	0.5000	4.2(1)
C(9)	0.1033(1)	0.0000	0.5000	2.37(9)
C(10)	0.1459(1)	0.0000	0.5000	2.34(9)
C(11)	0.16202(10)	0.2554(3)	0.7010(3)	4.12(9)
C(12)	0.1302(1)	0.3321(4)	0.7566(4)	7.1(1)
C(13)	0.1866(1)	0.1987(4)	0.7942(3)	6.6(1)
C(14)	0.1893(1)	0.3355(3)	0.6325(4)	5.8(1)
C(15)	0.0206(2)	–0.0226(5)	0.8499(5)	11.2(3)
C(16)	0.0417(2)	0.0757(6)	0.8672(6)	10.8(2)
C(17)	0.0209(2)	0.1760(6)	0.8858(5)	9.6(2)
H(1)	0.0000	0.161(4)	0.625(3)	3(1)
H(2)	0.0826(9)	0.210(3)	0.662(3)	4.8(9)

H(3)	0.2255(10)	0.129(3)	0.609(3)	5.1(10)
H(4)	0.261(1)	0.0000	0.5000	5(1)
H(5)	0.1145	0.3700	0.7022	8.5265
H(6)	0.1126	0.2871	0.8010	8.5265
H(7)	0.1439	0.3866	0.8010	8.5265
H(8)	0.1685	0.1554	0.8389	7.9302
H(9)	0.1995	0.2556	0.8374	7.9302
H(10)	0.2069	0.1501	0.7637	7.9302
H(11)	0.1730	0.3737	0.5796	6.9341
H(12)	0.2019	0.3898	0.6794	6.9341
H(13)	0.2099	0.2925	0.5963	6.9341
H(14)	0.040(1)	0.243(5)	0.886(4)	10(1)

Table 2.6.3. Selected geometric parameters (Å, °) of **2.3**

F(1)—C(15)	1.256(7)	C(15)—C(15*)	1.34(1)
F(2)—C(16)	1.581(9)	C(15)—C(16)	1.361(8)
C(1)—C(2)	1.394(3)	C(16)—C(17)	1.379(7)
C(1)—C(2*)	1.394(3)	C(17)—C(17*)	1.36(1)
C(2)—C(2*)	1.437(5)	C(1)—H(1)	1.00(4)
C(2)—C(3)	1.450(4)	C(4)—H(2)	0.94(3)
C(3)—C(4)	1.404(4)	C(7)—H(3)	0.97(3)
C(3)—C(9)	1.399(4)	C(8)—H(4)	1.01(4)
C(4)—C(5)	1.391(4)	C(12)—H(5)	0.950
C(5)—C(6)	1.453(4)	C(12)—H(6)	0.950
C(5)—C(11)	1.540(4)	C(12)—H(7)	0.950
C(6)—C(7)	1.411(4)	C(13)—H(8)	0.950
C(6)—C(10)	1.433(3)	C(13)—H(9)	0.950
C(7)—C(8)	1.377(4)	C(13)—H(10)	0.950
C(9)—C(10)	1.389(5)	C(14)—H(11)	0.950
C(11)—C(12)	1.533(5)	C(14)—H(12)	0.950
C(11)—C(13)	1.542(5)	C(14)—H(13)	0.950
C(11)—C(14)	1.543(5)	C(17)—H(14)	1.01(5)

C(2)—C(1)—C(2*)	118.1(4)	C(3)—C(9)—C(10)	124.3(2)
C(1)—C(2)—C(2)*	120.9(2)	C(6)—C(10)—C(6*)	125.0(4)
C(1)—C(2)—C(3)	131.5(3)	C(6)—C(10)—C(9)	117.5(2)
C(2*)—C(2)—C(3)	107.6(2)	C(5)—C(11)—C(12)	112.0(3)
C(2)—C(3)—C(4)	135.4(3)	C(5)—C(11)—C(13)	110.2(3)
C(2)—C(3)—C(9)	106.8(3)	C(5)—C(11)—C(14)	111.1(3)
C(4)—C(3)—C(9)	117.8(3)	C(12)—C(11)—C(13)	106.3(3)
C(3)—C(4)—C(5)	121.6(3)	C(12)—C(11)—C(14)	105.6(3)
C(4)—C(5)—C(6)	119.4(3)	C(13)—C(11)—C(14)	111.4(3)
C(4)—C(5)—C(11)	119.1(3)	F(1)—C(15)—C(15*)	103.3(5)
C(6)—C(5)—C(11)	121.5(3)	F(1)—C(15)—C(16)	135.3(7)
C(5)—C(6)—C(7)	125.7(3)	C(15*)—C(15)—C(16)	120.3(4)
C(5)—C(6)—C(10)	119.3(3)	F(2)—C(16)—C(15)	122.7(7)
C(7)—C(6)—C(10)	115.0(3)	F(2)—C(16)—C(17)	113.5(7)
C(6)—C(7)—C(8)	121.0(4)	C(15)—C(16)—C(17)	120.3(7)
C(7)—C(8)—C(7*)	122.9(5)	C(16)—C(17)—C(17*)	119.4(4)
C(3)—C(9)—C(3*)	111.3(4)		

The data was corrected for Lorentz and polarization factors. The structure was solved by direct methods and refined by full-matrix least squares calculations with anisotropic displacement factors for C-atoms. The ring H atoms in the molecule were located experimentally and the positions of the *tert*-butyl H atoms were calculated from an idealized geometry with standard bond length and angles. Calculations were carried out using the MITHRIL90 programs.

2.6.2 TCNQ complex of TTB-IDPL 2.3

The 1:1 complex formed between 7,7,8,8-tetracyanoquinodimethane (TCNQ) and **2.3** crystallized as deep green needles in space group $P\bar{1}$ with one molecule in the unit cell by recrystallization from a CH_2Cl_2 solution at 5 °C. The solvents entered the composition in a disordered way. The crystal structure consisted of infinite columns of alternate TCNQ and **2.3** molecules stack in a plane-to-plane manner in columns along to the *c* axis of the unit cell. A TCNQ molecule lay on the phenalenyl unit corresponding to the redox site of **2.3** with an interplanar distance between TCNQ and **2.3** rings of 3.33 Å. The bond lengths and angles of **2.3** and TCNQ were found to be similar to those of neutral **2.3** and neutral TCNQ, [30] respectively.

Degree of charge transfer for TCNQ complexes can be estimated from the ratio $c/(b + d)$ (Figure 2.6.4). [31] The application of this equation to the **2.3** – TCNQ complex leads to the value of 0.474, which is identical with that of neutral TCNQ. A frequency of the CN stretching mode can also estimate the charge on TCNQ. [32] The IR spectra of the **2.3** – TCNQ complex exhibited a peak at 2214 cm^{-1}, from which the charge on TCNQ could be estimated to be about 0.3. The electronic absorption spectra of the complex gave intense peaks at 790 and 364 nm, which were assignable to local π–π^* transitions of neutral **2.3**. In addition to these intense bands, weak charge-transfer bands were observed in 1200 – 2600 nm. In a CH_2Cl_2 solution of the complex, any charge-transfer bands could not be observed (Figure 2.6.5). The weak charge-transfer interaction suggests that the each component molecules in the complex should retain a similar structure to that of neutral state. Thus the ground state of the complex should be nearly neutral.

(a)

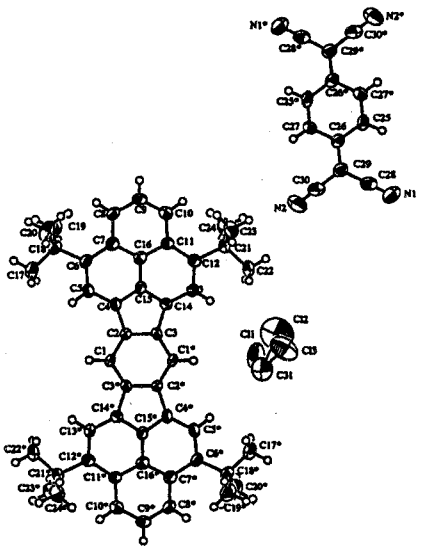

(b)

(c)

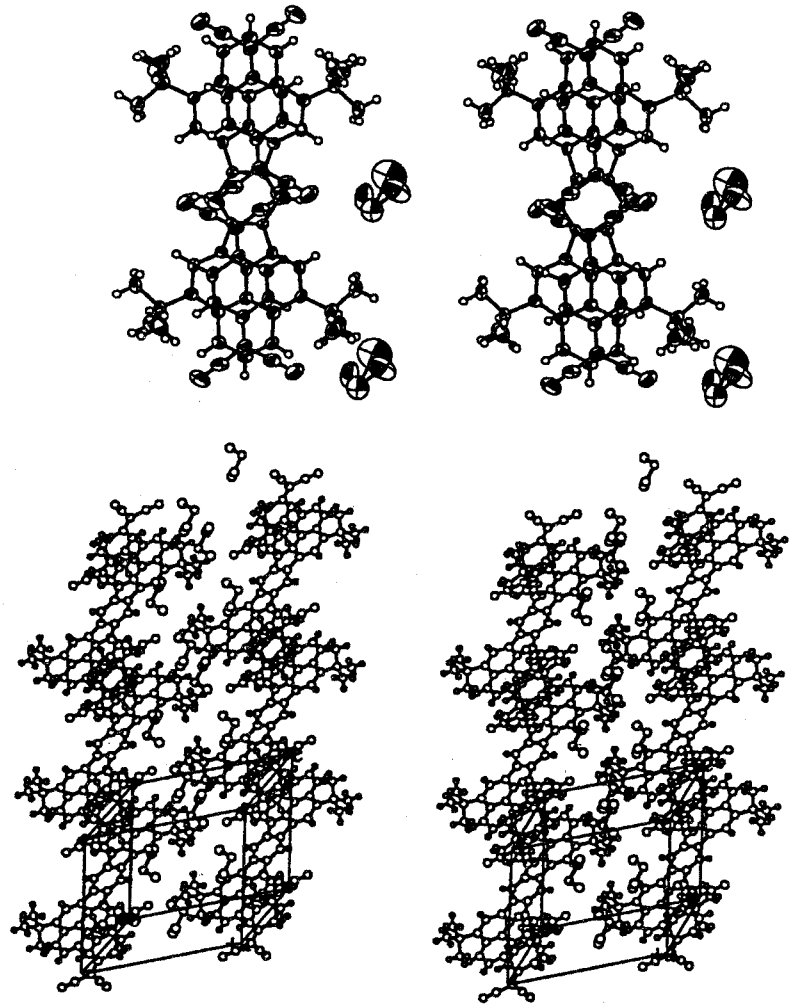

Figure 2.6.3. (a) The moleculer structure of **2.3** – TCNQ complex, (b) the molecular overlap in columns of alternating **2.3** and TCNQ, and (c) the stereoscopic view of the molecular packing. Displacement ellipsoids are drawn at the 50% probability level.

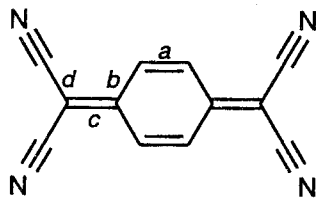

	a	*b*	*c*	*d*	*c*/(*b*+*d*)	CT%
$TCNQ^0$	1.346(3)	1.448(4)	1.374(3)	1.441(3)	0.476	0
TMPD–$(TCNQ)_2$	1.353(2)	1.431(2)	1.394(2)	1.423(3)	0.488	50
$TCNQ^-$	1.373(4)	1.423(4)	1.420(4)	1.416(4)	0.500	100
2.3–TCNQ	1.34	1.45	1.37	1.44	0.474	0

Figure 2.6.4. TCNQ molecular geometry.

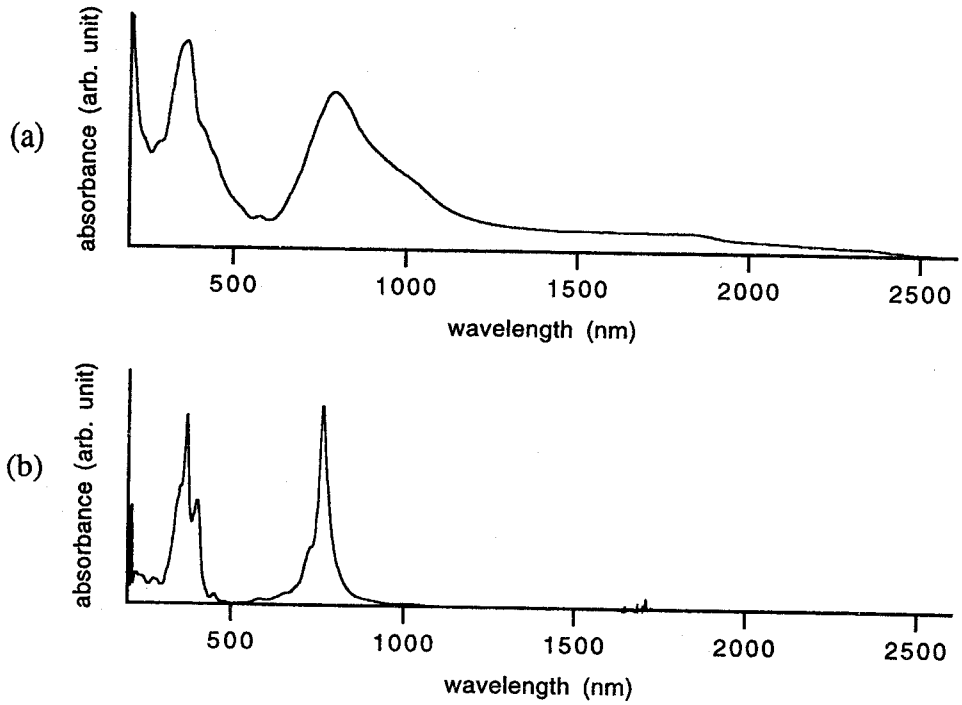

Figure 2.6.5. Electronic absorption spectra of the **2.3**–TCNQ complex. (a) In KBr pellet and (b) in CH_2Cl_2.

Table 2.6.4. Experimental X-ray data of the **2.3**–TCNQ complex.

Crystal data

$C_{62}H_{56}N_4Cl_4$
$M_r = 998.96$
Triclinic
$P\bar{1}$
$a = 11.570(3)$ Å
$b = 12.697(4)$ Å
$c = 10.722(2)$ Å
$\alpha = 103.12(2)°$
$\beta = 112.18(1)°$
$\gamma = 69.02(2)°$
$V = 1354.1(6)$ Å^3
$Z = 1$
$D_x = 1.225$ Mg m^{-3}

Mo$K\alpha$ radiation
$\lambda = 0.71070$ Å
Cell parameters from
3 stills @ 5 min
Detector distance = 143.2 mm
Detector swing angle = 0.00°
Pixel mode = 0.1 mm
$\mu = 0.261$ mm^{-1}
$T = 288$ K
Prismatic
0.20 x 0.10 x 0.10 mm
Green

Data collection

R-Axis CS diffractometer
16 exposures @ 30 min
Absorption correction: none
2745 measured reflections
2736 observed reflections
$[I > 3.00\sigma(I)]$

$2\theta_{max} = 59.7°$

Refinement

Refinement on F
$R = 0.102$
$wR = 0.105$
$S = 2.84$

$(\Delta/\sigma)_{max} = 0.06$
$\Delta\rho_{max} = 0.44$ e Å^{-3}
$\Delta\rho_{min} = -0.51$ e Å^{-3}
Extinction correction: none

2736 reflections
349 parameters
$w = 1/\sigma^2(F_O)$

Atomic scattering factors
from *International Tables for X-ray crystallograpy* (1974, Vol. IV)

Table 2.6.5. Fractional atomic coordinates and equivalent isotropic displacement parameters (Å^2) of the **2.3**–TCNQ complex.

$B_{eq} = (8\pi^2/3)(U_{11}(aa^*)^2+U_{22}(bb^*)^2+U_{33}(cc^*)^2+2U_{12}aa^*bb^*\cos\gamma+2U_{13}aa^*cc^*\cos\beta+2U_{23}bb^*cc^*\cos\alpha)$

	x	*y*	*z*	B_{eq}
Cl(1)	0.1406(3)	0.4066(2)	0.4342(3)	8.77(8)
Cl(2)	–0.013(2)	0.436(2)	0.168(2)	15.1(6)
Cl(3)	–0.0776(9)	0.4393(9)	0.1772(10)	10.7(2)
N(1)	0.1587(6)	1.1137(5)	0.1841(6)	5.4(2)
N(2)	0.4132(7)	0.7637(6)	0.2132(6)	6.4(2)
C(1)	0.5943(5)	–0.1119(5)	0.5080(5)	2.4(1)
C(2)	0.6004(5)	–0.0302(4)	0.4449(5)	2.5(1)
C(3)	0.5058(5)	0.0809(4)	0.4354(5)	2.4(1)
C(4)	0.6924(6)	–0.0350(4)	0.3803(5)	2.6(1)
C(5)	0.8072(6)	–0.1146(5)	0.3619(6)	2.9(1)
C(6)	0.8789(5)	–0.0908(5)	0.2997(5)	2.8(1)
C(7)	0.8301(6)	0.0189(5)	0.2447(5)	3.0(1)
C(8)	0.8874(6)	0.0526(5)	0.1726(6)	3.2(2)
C(9)	0.8345(7)	0.1583(5)	0.1268(7)	3.6(2)
C(10)	0.7270(6)	0.2396(6)	0.1549(6)	3.6(2)
C(11)	0.6609(6)	0.2150(5)	0.2259(5)	2.9(1)
C(12)	0.5468(6)	0.2938(5)	0.2634(6)	3.1(1)
C(13)	0.4891(6)	0.2563(5)	0.3299(6)	2.9(1)
C(14)	0.5396(6)	0.1449(5)	0.3654(5)	2.6(1)
C(15)	0.6503(5)	0.0708(4)	0.3328(5)	2.7(1)
C(16)	0.7150(6)	0.1020(5)	0.2674(5)	2.9(1)
C(17)	1.0497(7)	–0.2791(6)	0.3735(7)	5.6(2)
C(18)	1.0108(6)	–0.1795(5)	0.2928(5)	3.1(1)
C(19)	1.1219(7)	–0.1267(6)	0.3571(7)	4.9(2)
C(20)	1.0003(7)	–0.2297(6)	0.1444(7)	5.4(2)
C(21)	0.4907(6)	0.4185(5)	0.2297(6)	3.4(2)
C(22)	0.3762(8)	0.4881(5)	0.2857(7)	5.4(2)
C(23)	0.4317(7)	0.4234(6)	0.0752(7)	5.0(2)
C(24)	0.5963(8)	0.4785(6)	0.2948(7)	5.1(2)
C(25)	0.3921(6)	1.0876(5)	0.0201(6)	3.3(1)
C(26)	0.4300(6)	0.9796(5)	0.0721(5)	3.0(1)
C(27)	0.5417(6)	0.8924(5)	0.0461(6)	3.5(2)
C(28)	0.2485(7)	1.0448(6)	0.1637(6)	3.9(2)
C(29)	0.3602(6)	0.9583(5)	0.1370(6)	3.5(2)
C(30)	0.3905(7)	0.8505(7)	0.1818(6)	4.1(2)
C(31)	0.0044(9)	0.3684(8)	0.3177(9)	7.9(3)
H(1)	0.663(4)	–0.183(4)	0.521(4)	1.2(9)
H(2)	0.832(4)	–0.182(4)	0.398(4)	0.9(9)
H(3)	0.961(5)	0.004(4)	0.152(4)	1.3(10)
H(4)	0.876(6)	0.180(5)	0.088(5)	3(1)
H(5)	0.698(5)	0.310(4)	0.119(4)	2(1)
H(6)	0.413(5)	0.306(4)	0.348(4)	2(1)
H(7)	0.4065	0.4886	0.3814	6.5452
H(8)	0.3447	0.5636	0.2630	6.5452
H(9)	0.3074	0.4543	0.2469	6.5452
H(10)	0.6243	0.4799	0.3905	6.1468
H(11)	0.6688	0.4385	0.2635	6.1468
H(12)	0.5616	0.5538	0.2709	6.1468
H(13)	0.3998	0.5001	0.0564	6.0265
H(14)	0.4973	0.3820	0.0345	6.0265
H(15)	0.3618	0.3911	0.0396	6.0265
H(16)	1.2013	–0.1813	0.3499	5.9359
H(17)	1.1032	–0.0635	0.3115	5.9359
H(18)	1.1308	–0.1023	0.4499	5.9359
H(19)	0.9359	–0.2682	0.1097	6.4391
H(20)	0.9761	–0.1701	0.0910	6.4391

H(21)	1.0825	–0.2814	0.1417	6.4391
H(22)	0.9838	–0.3160	0.3379	6.7920
H(23)	1.1304	–0.3314	0.3666	6.7920
H(24)	1.0593	–0.2518	0.4658	6.7920
H(25)	0.5684	0.8198	0.0761	4.1161
H(26)	0.3174	1.1459	0.0335	3.9989

Table 2.6.6. Selected geometric parameters (Å, °) of the **2.3**–TCNQ complex.

Cl(1)—C(31)	1.751(9)	C(10)—C(11)	1.407(7)
Cl(2)—Cl(3)	0.77(2)	C(11)—C(12)	1.476(8)
Cl(2)—C(31)	1.90(2)	C(11)—C(16)	1.443(7)
Cl(3)—C(31)	1.70(1)	C(12)—C(13)	1.386(7)
N(1) —C(28)	1.152(8)	C(12)—C(21)	1.551(7)
N(2) —C(30)	1.137(8)	C(13)—C(14)	1.403(7)
C(1) —C(2)	1.395(7)	C(14)—C(15)	1.405(7)
C(1) —C(3*)	1.399(7)	C(15)—C(16)	1.393(7)
C(2) —C(3)	1.440(7)	C(17)—C(18)	1.531(9)
C(2) —C(4)	1.453(7)	C(18)—C(19)	1.522(9)
C(3) —C(14)	1.452(7)	C(18)—C(20)	1.549(8)
C(4) —C(5)	1.404(7)	C(21)—C(22)	1.555(8)
C(4) —C(15)	1.398(7)	C(21)—C(23)	1.542(8)
C(5) —C(6)	1.382(7)	C(21)—C(24)	1.530(9)
C(6) —C(7)	1.472(7)	C(25)—C(26)	1.454(8)
C(6) —C(18)	1.556(8)	C(25)—C(27*)	1.338(8)
C(7) —C(8)	1.401(7)	C(26)—C(27)	1.443(8)
C(7) —C(16)	1.439(8)	C(26)—C(29)	1.370(7)
C(8) —C(9)	1.379(8)	C(28)—C(29)	1.441(9)
C(9) —C(10)	1.387(9)	C(29)—C(30)	1.434(9)

Cl(1)—C(31)—Cl(2)	98.3(7)	C(26)—C(29)—C(30)	123.5(6)
Cl(1)—C(31)—Cl(3)	116.7(6)	C(11)—C(12)—C(21)	120.8(5)
Cl(2)—C(31)—Cl(3)	23.9(8)	C(13)—C(12)—C(21)	119.5(5)
C(2)—C(1)—C(3*)	117.4(5)	C(12)—C(13)—C(14)	121.0(5)
C(1)—C(2)—C(3)	121.4(4)	C(3)—C(14)—C(13)	134.8(5)
C(1)—C(2)—C(4)	130.6(5)	C(3)—C(14)—C(15)	105.9(5)
C(3)—C(2)—C(4)	107.9(4)	C(13)—C(14)—C(15)	119.2(5)
C(1*)—C(3)—C(2)	121.2(4)	C(4)—C(15)—C(14)	112.5(5)
C(1*)—C(3)—C(14)	131.0(5)	C(4)—C(15)—C(16)	124.0(5)
C(2)—C(3)—C(14)	107.8(4)	C(14)—C(15)—C(16)	123.4(5)
C(2)—C(4)—C(5)	135.8(5)	C(7)—C(16)—C(11)	124.6(5)
C(2)—C(4)—C(15)	105.9(5)	C(7)—C(16)—C(15)	117.6(5)
C(5)—C(4)—C(15)	118.2(5)	C(11)—C(16)—C(15)	117.8(5)
C(4)—C(5)—C(6)	122.0(5)	C(6)—C(18)—C(17)	111.9(5)
C(5)—C(6)—C(7)	119.2(5)	C(6)—C(18)—C(19)	110.5(5)
C(5)—C(6)—C(18)	119.2(5)	C(6)—C(18)—C(20)	110.6(5)
C(7)—C(6)—C(18)	121.6(5)	C(17)—C(18)—C(19)	105.3(5)
C(6)—C(7)—C(8)	125.9(5)	C(17)—C(18)—C(20)	107.0(6)
C(6)—C(7)—C(16)	118.8(5)	C(19)—C(18)—C(20)	111.3(5)
C(8)—C(7)—C(16)	115.3(5)	C(12)—C(21)—C(22)	112.1(5)
C(7)—C(8)—C(9)	121.2(6)	C(12)—C(21)—C(23)	110.6(5)
C(8)—C(9)—C(10)	122.8(6)	C(12)—C(21)—C(24)	110.4(5)
C(9)—C(10)—C(11)	120.9(6)	C(22)—C(21)—C(23)	105.3(5)
C(10)—C(11)—C(12)	126.2(5)	C(22)—C(21)—C(24)	106.4(5)
C(10)—C(11)—C(16)	115.1(5)	C(23)—C(21)—C(24)	111.9(5)
C(12)—C(11)—C(16)	118.7(5)	C(26)—C(25)—C(27)	122.4(5)
C(11)—C(12)—C(13)	119.7(5)	C(25)—C(26)—C(27)	116.9(5)
C(25)—C(26)—C(29)	122.3(6)	C(28)—C(29)—C(30)	115.3(6)
C(27)—C(26)—C(29)	120.7(5)	N(2) —C(30)—C(29)	177.9(7)
C(25*)—C(27)—C(26)	120.7(5)	C(26)—C(29)—C(28)	121.2(6)
N(1)—C(28)—C(29)	179.6(7)		

The data was corrected for Lorentz and polarization factors. The structure was solved by direct methods and refined by full-matrix least squares calculations with anisotropic displacement factors for C-atoms. The ring H atoms in **2.3** were located

experimentally. The positions of the *tert*-butyl H atoms of **2.3** and ring H atoms of TCNQ were calculated from an idealized geometry with standard bond length and angles. Calculations were carried out using the MULTAN88 programs.

2.7 Conclusion

As expected, IDPL was found to behave as a four-stage amphoteric redox compound. In particular, tetra-*tert*-butyl derivative (TTB-IDPL, **2.3**) showed enough stability to give many reliable data for five redox states of **2.3**. The ^{13}C NMR and ESR spectra suggested that the charges and spin of four charged species of **2.3** are delocalized over the whole of the molecules and distribute like phenalenyl species on the two phenalenyl units of **2.3**. The similarity of the distribution pattern supports the NBMO character for HOMO and LUMO of **2.3**. The NBMO character of frontier orbitals should be responsible for the small HOMO–LUMO gap, *i.e.* the small E_1^{sum} value, which is consistent with low-energy transition at 755 nm observed in UV/Vis/NIR spectrum of neutral **2.3**. In conclusion, phenalenyl units contribute largely to higher amphotericity of **2.3** and the stability of the five redox states of **2.3**.

2.8 Experimental

General remarks. All experiments with moisture- or air-sensitive compounds were performed in anhydrous solvents under argon atmosphere in flame-dried glassware. Solvents were dried and distilled according to the standard procedures. Column chromatography were performed with silicagel [Wako gel C-200 (Wako)] or basic alumina [200 mesh (Wako)]. Infrared spectra were recorded on a Perkin Elmer FT 1640 IR spectrometer. Electronic spectra were measured at room temprature in a 10 mm-pathlength quartz cell by a Shimadzu UV-3100PC spectrometer. ^1H and ^{13}C NMR spectra were obtained on JEOL EX-270, JEOL GSX-400, JEOL GSX-500, and Varian UNITY plus 600 spectrometers. Chemical shifts are reported relative to TMS (0.00 ppm) as an internal standard. Positive EI, FAB, and FD mass spectra were taken by using JEOL JMS SX-102 and Shimadzu QP-5000 mass spectrometers. ESR spectra were obtained with a JEOL JES-FE2XG spectrometer. The *g*-value was determined by the use of Li-TCNQ (g = 2.0026) as external standard. Cyclic voltammetric measurements were made with a Yanagimoto P1100 spectrometer. Cyclic voltammograms of the compound were recorded with glassy carbon working electrode and Pt counter electrode in CH_2Cl_2 containing 0.1 M $(n\text{-Bu})_4NClO_4$ as the supporting

electrolyte. The experiments employed a SCE reference electrode. Electrochemical experiments were done under an argon atmosphere at 0 °C.

4,8,12,16-tetra-*tert*-butyl-*s*-indaceno[1,2,3-*cd*:5,6,7-*c'd'*]diphenalene (2.3).[6] A mixture of **2.8** (41.6 mg, 66.4 μmol) and *p*-chloranil (18.1 mg, 73.6 μmol) in benzene (70 mL) was refluxed for 40 min. The mixture was cooled on ice-bath and concentrated *in vacuo*. The crude product was purified by column chromatography on silica gel [benzene/hexane (1:4, v/v)] to give **2.3** (32.2 mg, 78%): mp >300 °C. ^{1}H NMR [400 MHz, CS_2 / acetone-d_6 (4:1, v/v)] δ 7.69 (d, J = 8.4 Hz, 2H), 7.10 (s, 2H), 7.04 (s, 4H), 6.98 (t, J = 8.4 Hz, 4H), 1.51 (s, 36H). FD MS *m/z* 624 (M^+). Anal. Calcd for $C_{48}H_{48}$: C, 92.26; H, 7.74. Found: C, 92.29; H, 7.79.

Dication (2.3^{2+}). The hydrocarbon **2.3** (5mg, 8 μmol) was added to 0.5 ml of concentrated D_2SO_4 to give a dication species. A reddish purple color appeared immediately. The dication was also obtained by the reaction of **2.3** (22.5 mg, 36 μmol) with excess $SbCl_5$ (0.05 M, 2.88 ml, 144 μmol) in 22.5 ml of CH_2Cl_2.

Radical cation ($2.3^{(\bullet)(+)}$). Radical cation was generated by the reaction of **2.3** (22.5 mg, 36 μmol) with an equimoler amount of $SbCl_5$ (0.05 M, 0.72 ml, 36 μmol) in 22.5 ml of CH_2Cl_2. A solution turned to greenish blue immediately.

Radical anion ($2.3^{(\bullet)(-)}$). Radical anion was generated under vacuum (*ca.* 10^{-4} torr) in sealed cell B (Figure 2.8.2) by the reaction of **2.3** with a potassium mirror in DME or THF. For the detailed procedure, see below.

Dianion (2.3^{2-}). The reaction of dihydro compounds **2.8** (7.5 mg, 12 μmol) with a potassium mirror in THF-d_8 (0.5 ml) in a sealed degassed tube afforded dianion species. The dianion was also obtained by the reaction of **2.3** with a potassium mirror in THF in a sealed degassed tube. For the detailed procedure, see below.

2.3–TCNQ complex. The solution of **2.3** (11.4 mg, 18.3 μmol) and TCNQ (7.3 mg, 36.5 μmol) in CH_2Cl_2 (11 mL) was allowed to stand at 5 °C for 4 days. The resulting green needles (10.5 mg, 70%) were collected: mp >300 °C. IR (KBr) 2214 cm^{-1}. Anal. Calcd for $C_{60}H_{52}N_4$: C, 86.92; H, 6.32; N, 6.76. Found: C, 86.31; H, 6.14; N, 6.83. The material for elemental analysis was dried under vacuum at 100 °C for a day.

NMR spectroscopy.

Dianion (2.3^{2-}). Figure 2.8.1 shows the cell used for the generation of 2.3^{2-}.

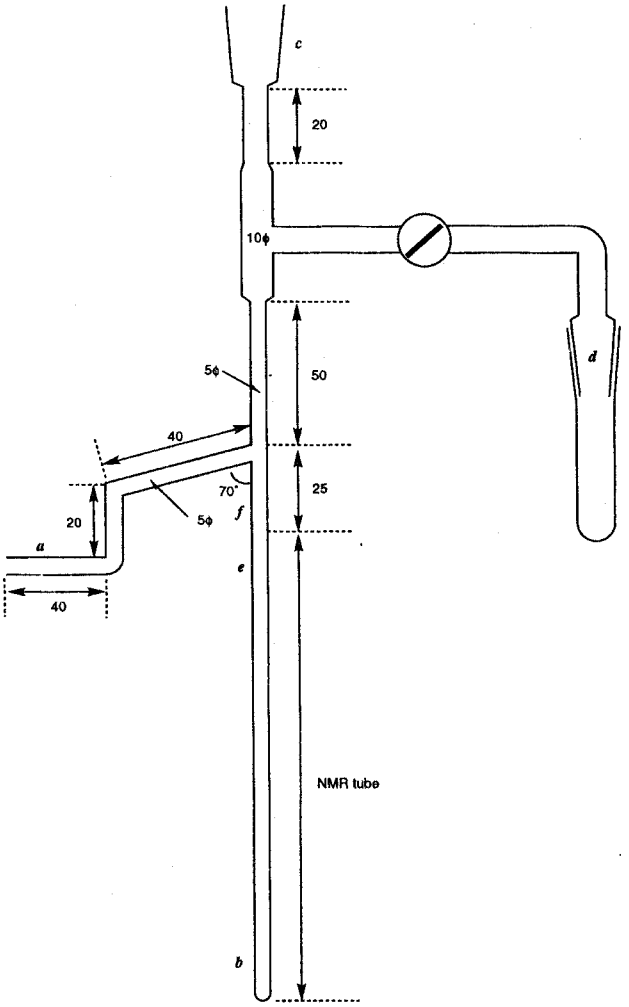

Figure 2.8.1. Cells for NMR measurements of dianion.

A clean peace of potassium was passed into the side arm and sealed at ***a***. The dihydro compounds **2.8** was introduced into NMR tube ***b***. A test-tube containing 1 mL of THF-d_8 with a drop of Na-K alloy was attached to ***c*** and the cell was connected to a vacuum line at ***d***. The solvent was degassed by a repeated freeze-pump-thaw method (5 times) and distilled into ***b*** by 0.5 mL. The side arm was warmed with a luminous flame to distill the metal as a mirror onto the walls at ***e***. Finally, the cell was sealed at ***f***. The contact of the solution with a potassium mirror at – 78 °C for a week gave a deep blue solution, whose NMR spectrum supported the generation of 2.3^{2-}.

ESR spectroscopy.

Neutral (2.3). The cell A (Figure 2.8.2) was used for the ESR measurement of **2.3**. The compound **2.3** was purified by column chromatography (silica gel) and then recrystallized from benzene to give green prisms. For the solution state studies, a soltion of **2.3** (2×10^{-4} M, 0.2 ml) in toluene was introduced into the cell ***a*** by a syringe. The cell was connected to a vacuum line at ***b*** and the solvent was degassed by

a repeated freeze-pump-thaw method (5 times). The cell was sealed at ***c*** and the ESR spectra of **2.3** were recorded. For the solid state studies, the solid **2.3** (5 mg) was introduced into the cell ***a*** and the cell was connected to a vacuum line at ***b***. The cell was sealed at ***c*** and the ESR spectra of the solid **2.3** were recorded.

Radical cations ($2.3^{(\bullet)(+)}$). The cell A (Figure 2.8.2) was used for the ESR measurement of $2.3^{(\bullet)(+)}$. A soltion of $2.3^{(\bullet)(+)}$ (2×10^{-4} M, 0.2 ml) in CH_2Cl_2 was introduced into the cell ***a*** by a syringe. The cell was connected to a vacuum line at ***b*** and the solvent was degassed by a repeated freeze-pump-thaw method (5 times). The cell was sealed at ***c*** and the ESR spectra of radical cations were recorded.

Radical anions ($2.3^{(\bullet)(-)}$). The cell B (Figure 2.8.2) was used for the generation of $2.3^{(\bullet)(-)}$. A clean peace of potassium was passed into the side arm and sealed at ***a***. A solution of **2.3** (5×10^{-4} M, 0.2 ml) in DME was introduced into the cell ***b*** by a syringe. The cell was connected to a vacuum line at ***c*** and then the solvent was degassed by a repeated freeze-pump-thaw method (5 times). The side arm was warmed with a luminous flame to distill the metal as a mirror onto the walls at ***d***. The side arm was removed by sealing at ***e***. Finally, the cell was sealed at ***f***. The contact of the solution with a potassium mirror at ***d*** at room temperature gave the radical anion.

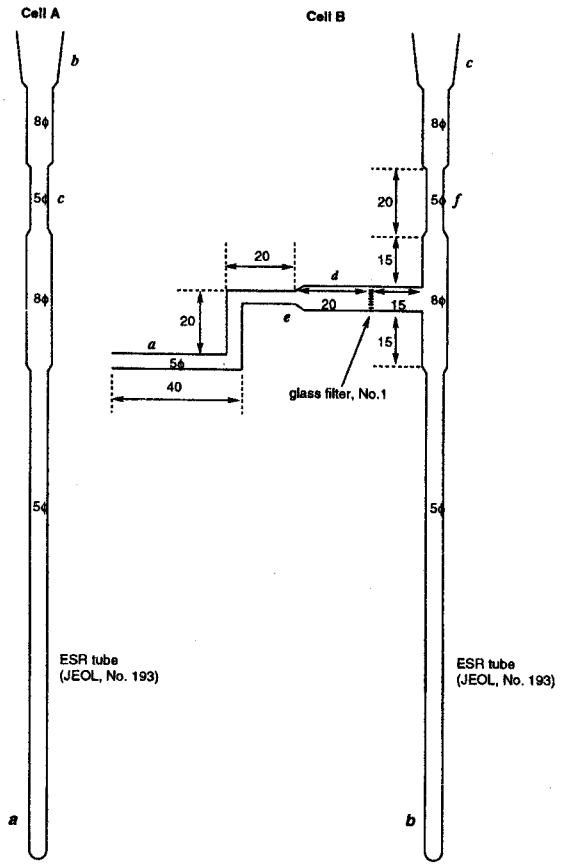

Figure 2.8.2. Cells for ESR meaurements.

UV/Vis/NIR specroscopy.

Dication (2.3^{2+}). The quantitative electronic spectrum of 2.3^{2+} was obtained by the dissolution of the solid **2.3** (1.0859 mg, 1.7377 μmol) in D_2SO_4 (100 mL) at room temperature.

Radical cation ($2.3^{(\bullet)(+)}$). The qualitative measurement was carried out in the CH_2Cl_2 solution of $2.3^{(\bullet)(+)}$ at room temperature.

Neutral (2.3). The compound **2.3** was purified by a column chromatography (silica gel) and then recrystallized from benzene to give green prisms. The pure **2.3** was dissolved in a mixture of CH_2Cl_2 and cyclohexane (100 mL, 1:100) and the quantitative measurement was carried out at room temperature.

Dianion (2.3^{2-}) and radical anion ($2.3^{(\bullet)(-)}$). Figure 2.8.3 shows the cell used for the generation of 2.3^{2-} and $2.3^{(\bullet)(-)}$.

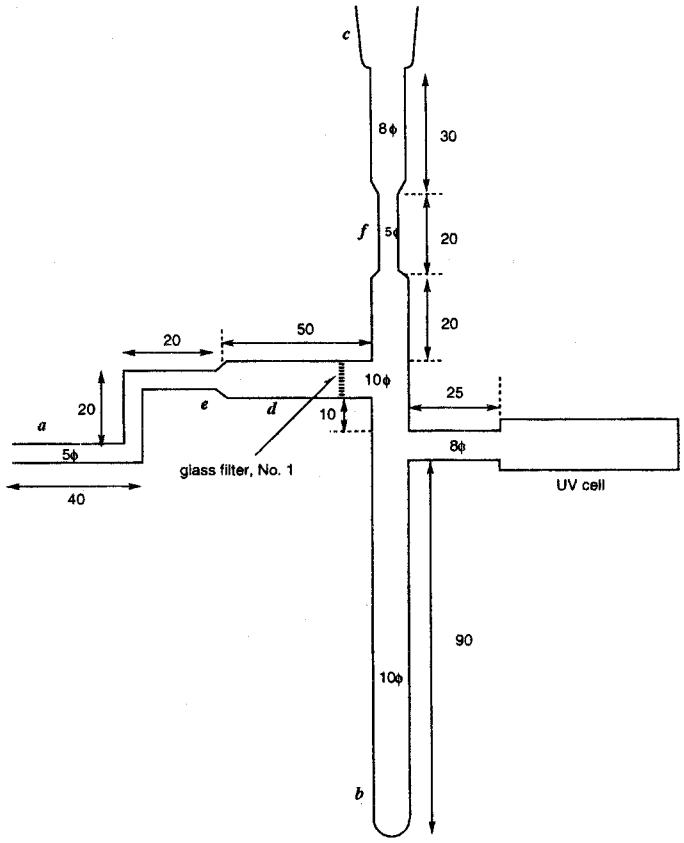

Figure 2.8.3. Cells for UV/Vis/NIR measurements of anions.

A clean peace of potassium was passed into the side arm and sealed at ***a***. The soltion of **2.3** in THF was introduced into the cell ***b*** by a syringe. The cell was connected to a vacuum line at ***c*** and then the solvent was degassed by a repeated freeze-pump-thaw method (5 times). The side arm was warmed with a luminous flame to distill the metal as a mirror onto the walls at ***d***. The side arm was removed by sealing at ***e***. Finally, the

cell was sealed at *f*. The contact of the solution with a potassium mirror at ***d*** at room temperature exhibited the gradual decrease of absorption of **2.3** and the new absorption attributable to **2.3**$^{(\bullet)(-)}$ appeared. Further contact with a potassium-mirror caused the gradual decrease of the absorption of **2.3**$^{(\bullet)(-)}$ with the gradual increase of the absorption of **2.3**$^{2-}$.

2.9 References

1) K. Nakasuji, K. Yoshida, I. Murata, *J. Am. Chem. Soc.* **1982**, *104*, 1432.

2) K. Nakasuji, K. Yoshida, I. Murata, *Chem. Lett.* **1982**, 969.

3) K. Nakasuji, K. Yoshida, I. Murata, *J. Am. Chem. Soc.* **1983**, *105*, 5136.

4) I. Murata, S. Sasaki, K.-U. Klabunde, J. Toyoda, K. Nakasuji, *Angew. Chem. Int. Ed. Engl.* **1991**. *30*, 172.

5) T. Masui, Master's Thesis, Osaka University, Japan, 1992.

6) K.Ohashi, Master's Thesis, Osaka University, Japan, 1995.

7) F. London, *J. Phys. Radium.* **1937**, *8*, 397; J. A. Pople, *Mol. Phys.* **1958**, *1*, 175; R. McWeeny, *Mol.Phys.* **1958**, *1*, 311; R. B. Mallion, *Mol. Phys.* **1973**, *25*, 1415; J. Aihara, *Bull. Chem. Soc. Jpn.* **1985**, *58*, 1045. See also section 3.4.4.

8) H. Spiesecke, W. G. Schneider, *Tetrahedron Lett.* **1961**, 468.

9) I. Sethson, D. Johnels, U. Edlund, A. Sygula, *J. Chem. Soc. Perkin Trans 2*. **1990**, 1339.

10) Another peripheral 28C-30π system is dindenoperilene dianion. See A. Minsky, M. Rabinovitz, *Tetrahedron Lett.* **1981**, *22*, 5341.

11) H. M. McConnell, *J. Chem. Phys.* **1956**, *24*, 764.

12) A. D. McLachlan, *Mol. Phys.* **1960**, *3*, 233.

13) F. Gerson, *Helv. Chim. Acta,* **1966**, *49*, 1463.

14) J. Kolc, J. Michl, *J. Am. Chem. Soc.* **1973**, *95*, 7391.

15) J. Kolc, J. W. Downing, A. P. Manzara, J. Michl, *J. Am. Chem. Soc.* **1976**, *98*, 930; R. P. Steiner, J. Michl, *ibid.* **1978**, *100*, 6413; A. Castellan, J. Kolc, J. Michl, *ibid* **1978**, *100*, 6687.

16) a) A. E. Chichibabin, *Ber. Dtsch. Chem. Ges.* **1907**, *40*, 1810. b) L. K. Montgomery, J. C. Huffman, E. A. Jurczak, M. P. Grendze, *J. Am. Chem. Soc.* **1986**, *108*, 6004, and references cited therein.

17) J. E. Wertz, R. Bolton, *Electron Spin Resonance*, McGraw-Hill, New York, 1972.

18) D (in G)= 27890 / r^3 (in Å).

19) A. de Meijere, F. Gerson, B. König, O. Reiser, T. Wellauer, *J. Am. Chem. Soc.* **1990**. *112*, 6827; F. Gerson, W. Huber, W. B. Martin, Jr., P. Caluwe, T. Pepper, M. Szwarc, *Helv. Chim. Acta,* **1984**, *67*, 416; F. Gerson, T. Wellhauser, A. M.

Oliver, M. N. Paddon-Row, *ibid.* **1990**, *73*, 1586; S. S. Eaton, K. M. More, B. M. Sawant, G. R. Eaton, *J. Am. Chem. Soc.* **1983**, *105*, 6560.

20) B. Bleaney, K. D. Bowers, *Proc. R. Soc. London, A* **1952**, 214; D. Bijl, H. Kainer, A. C. Rose-Innes, *J. Chem. Phys.* **1959**, *30*, 765.

21) L. Salem, *The molecular orbital theory of conjugated systems*, Benjamin, New York, 1966, p. 427.

22) J. Michl and E. W. Thulstrup have referred to the importance of the molecular exchange integral K_{ab} for the electronic excitation energy when they offered a simple explanation for the fact that azulene is blue and anthracene colorless, although the orbital energies of both structure are very similar. See *Tetrahedron* , **1976**. *32*, 205.

23) M. Kasha, *Disc. Faraday Soc.* **1950**. *9*, 14.

24) H. Angliker, F. Gerson, J. Lopez, J. Wirz, *Chem. Phys. Lett.* **1981**, *81*, 242; H. Angliker, E. Rommel, J. Wirz, *Chem. Phys. Lett.* **1982**, *87*, 208.

25) K. Lahlil, A. Moradpour, C. Bowlas, F. Menou, P. Cassoux, J. Bonvoisin, J-P. Launay, G. Dive, D. Dehareng, *J. Am. Chem. Soc.* **1995**, *117*, 9995.

26) T. H. Jozefiak, L. L. Miller, *J. Am. Chem. Soc.* **1987**, *109*, 6560; T. H. Jozefiak, J. E. Almlöf, M. W. Feyereisen, L. L. Miller, *ibid.* **1989**, *111*, 4105; J. E. Almöf, M. W. Feyerisen, T. H. Jozefiak, L. L. Miller, *ibid.* **1990**, *112*, 1206; L. L. Miller, C. A. Liberko, *Chem. Mater.* **1994**, *2*, 339; S. F. Rak, L. L. Miller, *J. Am. Chem. Soc.***1992**, *114*, 1388.

27) The properties of mixed valence compounds depend on the extent of the electronic interaction between the redox centers and range, in accordance with the common classification, from small (or nonexisting) (class I), sight (class II), to strong interaction (class III, which includes the completely delocalized molecules). See M. B. Robin, P. Day, *Adv. Inorg. Radiochem.* **1967**, *10*, 247.

28) See section 3.4.4.

29) S. Seth, H. Sur, S. Chakraborty, *Acta Crystallogr.* **1988**, *C44*, 1011.

30) J. D. Dunitz, C. Krüger, H. Irngartinger, E. F. Maverick, Y. Wang, M. Nixdorf, *Angew. Chem. Int. Ed. Engl.* **1988**, *27*, 387.

31) T. J. Kistenmacher, T. J. Emge, A. N. Bloch, D. O. Cowan, *Acta Crystallogr.* **1982**, *B38*, 1193.

32) J. S. Chappell, A. N. Bloch, W. A. Bryden, M. Maxfield, T. O. Poehler, D. O. Cowan, *J. Am. Chem. Soc.* **1981**, *103*, 2442.

– Chapter 3 –

Synthesis and Properties of tetra-*tert*-butyl-*as*-indaceno[1,2,3-*cd*;6,7,8-*c'd'*]diphenalene (TTB-*as*-IDPL)

3.1 Introduction

In chapter 2, I discussed the properties of TTB-IDPL **2.3** as a four-stage amphoteric redox compound. As shown in Figure 3.1.1, *as*-IDPL **3.1** containing an unstable *as*-indacene structure in the neutral state is also expected to exhibit a high amphotericity and to behave as a four-stage amphoteric redox system. This idea is supported by the HMO calculations (Figure 3.1.2), which indicate the smaller HOMO–LUMO gap than that of **2.1**; *higher* HOMO and *lower* LUMO in comparison with **2.1**. The LUMO with no longer maintaining NBMO character becomes weakly bonding.

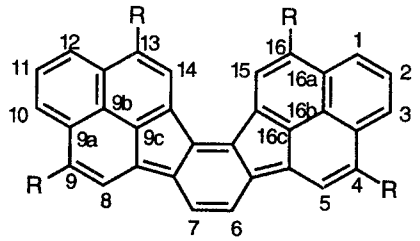

α-position : 1,3,4,5a,7b,9,10, 12,13,14a,14d,16
β-position : 2,5,8,11,14,15

3.1 R = H
3.2 R = ^{t}Bu

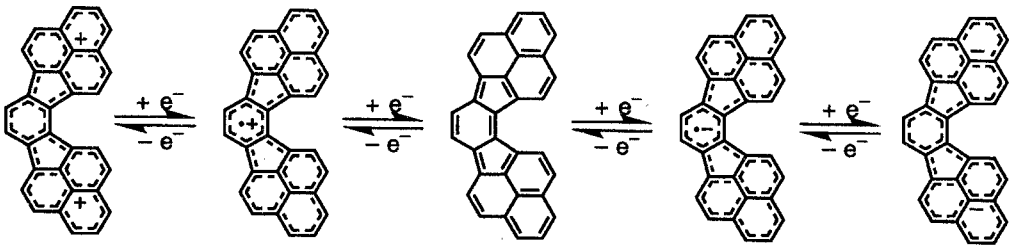

Figure 3.1.1. Four-stage amphoteric redox behavior of *as*-IDPL **3.1**

On the basis of the calculations, the following properties will be expected in comparison with **2.1**.

1. Smaller E_1^{sum} value due to the smaller HOMO–LUMO gap.
2. Instability due to higher oxidation and reduction abilities.

3. Upper-field shifts in ^{1}H NMR spectrum of neutral state due to a larger paramagnetic ring current effect.

The *as*-IDPL **3.1**, which is an isomer of IDPL **2.1**, has C_{2v} symmetry, while **2.1** belongs to higher symmetry, D_{2h}. In this chapter, I will compare the properties of TTB-*as*-IDPL **3.2** and TTB-IDPL **2.3** from the view point of the symmetry differences.

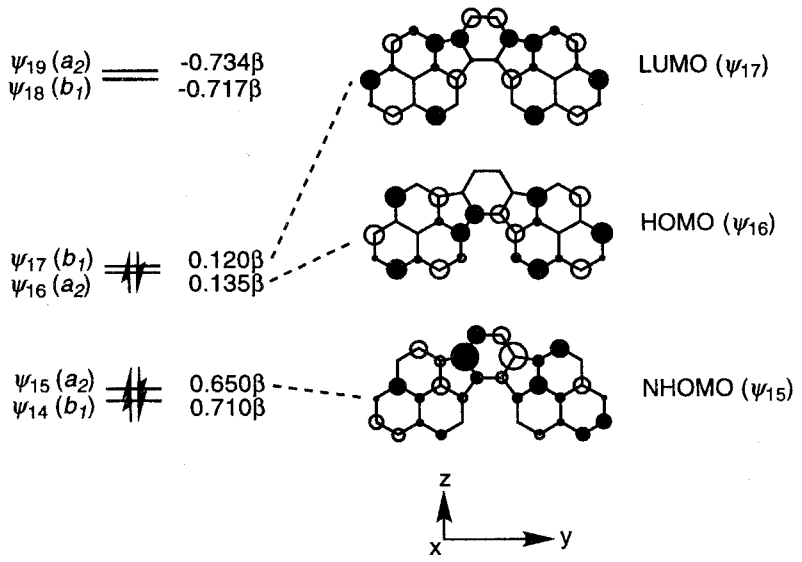

Figrure 3.1.2. Selected molecular orbitals of **3.1** calculated by the HMO method.

3.2 Synthesis

TTB-*as*-IDPL **3.2** was synthesized following scheme 3.1.1. The key intermediates are **3.5**, which were comprised of three isomers by the reaction of **2.5** with sulfur, followed by the Diels–Alder reaction and decarboxylation. [1] The hydrocarbons **3.5** were pale yellow and had a lighter color than **2.7**. The dihydro derivatives **3.10** were obtained readily by the synthetic procedure similar to that for TTB-IDPL **2.3**. The reaction of **3.10** with an equimolar *p*-chloranil afforded the target hydrocarbon **3.2** as a greenish brown oil. The hydrocarbon **3.2** was found to be extremely unstable compared to **2.3**. FAB MS (NBA) spectra supported the generation of **3.2** to give a peak at *m/z* 624 (M^+). However, an unexpected additional peak was found at *m/z* 640, which would arise from the oxidation of **3.2**. Unfortunately, ^{1}H NMR spectra could not give any important information about the structure of **3.2** due to the absence of signals in the aromatic regions.

Scheme 3.1.1. Synthetic procedure of **3.2**

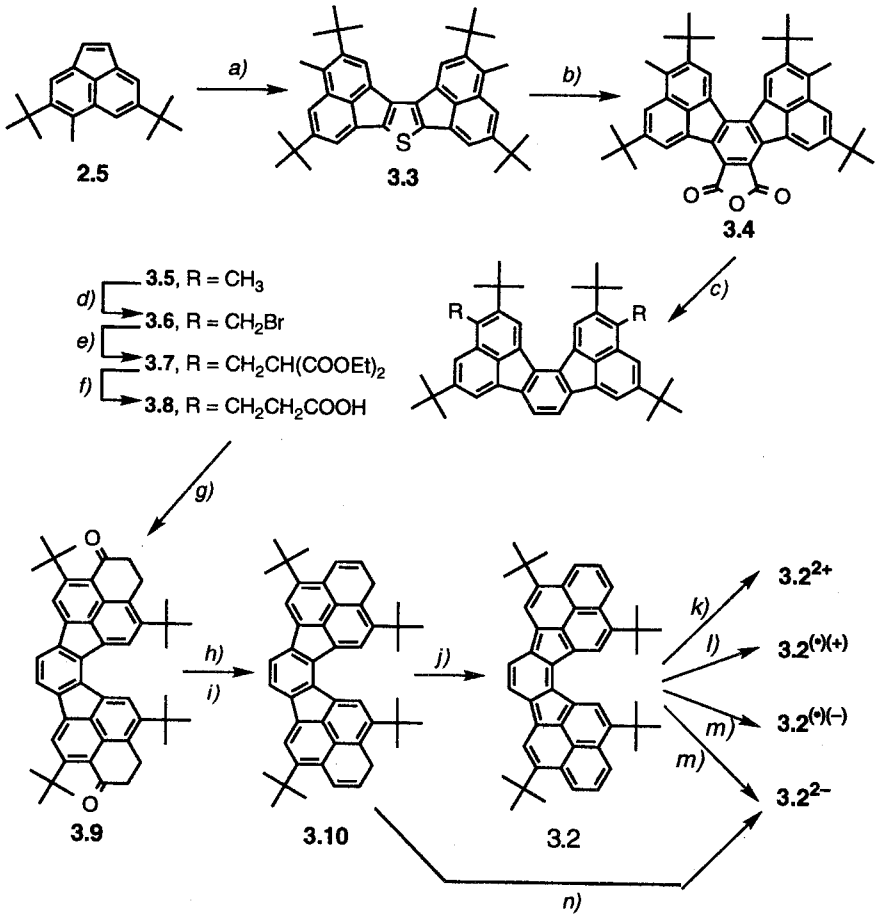

Reaction conditions : *a)* S_8, DMF, 135°C, 3 h, 65%. *b)* maleic anhydride, 225°C, 30 min, 79%. *c)* basic $CuCO_3$, quinoline, reflux, 6 h, 75%. *d)* NBS, benzoyl peroxide, benzene, reflux, 10 min. *e)* NaOEt, $CH_2(COOEt)_2$, EtOH + benzene, rt, 1 d, 62% (2 steps). *f)* 1) aqueous KOH, EtOH, reflux, 3 h, 2) 4 N HCl, 3) reflux, H_2O, 8 h, 91%. *g)* 1) $(COCl)_2$, reflux, 2 h, 2) $AlCl_3$, CH_2Cl_2, -40°C, 3 h, 80%. *h)* LAH, THF, rt, 1 h, 97%. *i)* cat. *p*-toluenesulfonic acid, benzene, reflux, 3 min, 90%. *j)* *p*-chloranil, benzene, reflux, 10 min. *k)* D_2SO_4 or excess $SbCl_5$, CH_2Cl_2. *l)* 1 eq $SbCl_5$, CH_2Cl_2. *m)* K-mirror, under vacuum, THF. *n)* K-mirror, under vacuum, THF-d_8.

3.3 Electrochemistry

The cyclic voltammogram of **3.2** exhibited four reversible redox waves as shown in Figure 3.3.1. This behavior provides the evidence for the formation of the stable singly and doubly charged species. Expectedly, TTB-*as*-IDPL **3.2** was also found to behave as a four stage amphoteric redox compound. Table 3.3.1 lists the electrochemical data for **3.2** obtained by the CV measurement along with those of **2.3**.

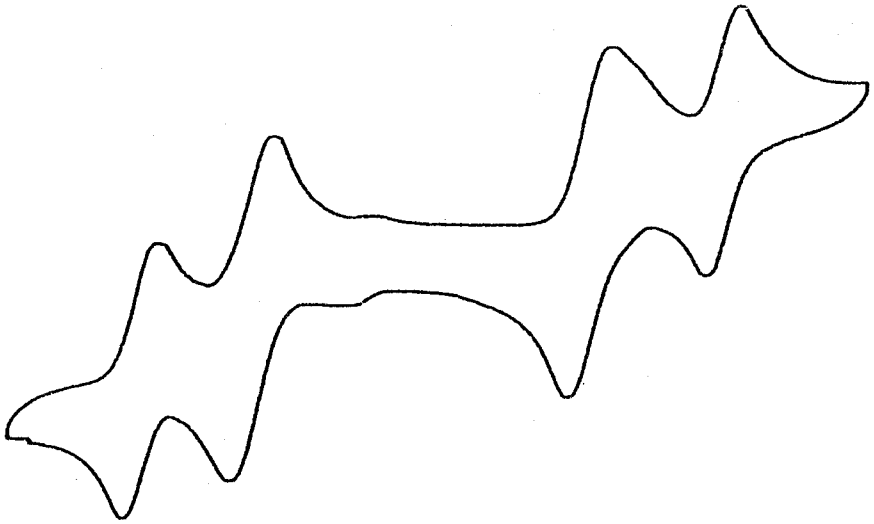

Figure 3.3.1. Cyclic voltammogram of **3.2**

compound	E_2^{ox}	E_1^{ox}	E_1^{red}	E_2^{red}	E_1^{sum}	E_2^{sum}
TTB-*as*-IDPL **3.2**	+0.75	+0.42	-0.58	-0.96	1.00	1.71
TTB-IDPL **2.3**	+0.84	+0.48	-0.67	-1.25	1.16	2.09

Table 3.3.1. Cyclic voltammetric data (V vs SCE) of **3.2** and **2.3** in dichloromethane with 0.1 M $(^n\text{Bu})_4\text{NClO}_4$ as supporting electrolyte at room temperature; sweep rate = 100 mv/s.

The oxidation potentials (E_1^{ox} and E_2^{ox}) of **3.2** appear in more negative regions than those of **2.3**. In contrast, the reduction potentials (E_1^{red} and E_2^{red}) of **3.2** are more positive than those of **2.3**. Compared to **2.3**, the higher oxidation and reduction ability of **3.2** cause the smaller E_1^{sum} (1.00 V) and E_2^{sum} (1.71 V). The E_1^{sum} of **3.2** is comparable to that of PDPL with the smallest E_1^{sum} (0.99 V) among the closed-shell hydrocarbons, whereas the E_2^{sum} of **3.2** is the smallest value among them. These findings are consistent with the HMO calculations.

The compound **3.2** are extremely sensitive to oxygen relative to the isomer **2.3**. The instability of **3.2** should be caused by the larger extent of biradicaloid character due to the smaller HOMO–LUMO gap relative to **2.3**. In the cannonical forms of **3.2**, not only *p*-quinoid but also *o*-quinoid structure appear in the central *as*-indacene unit, while **2.3** has only *p*-quinoid structre in the *s*-indacene unit.

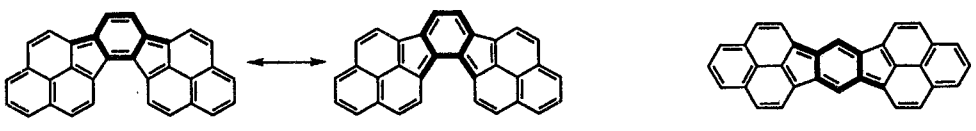

p-quinoid *o*-quinoid *p*-quinoid

Although both *o*- and *p*-quinodimethane are known to be highly reactive compounds, the heat of formation of *o*-quinodimethane (53 kcal/mol) is slightly larger than that of *p*-quinodimethane (50 kcal/mol).[2] Furthermore, the HMO calculations indicate the smaller HOMO–LUMO gap of *o*-quinodimethane (0.59β) relative to *p*-quinodemethane (0.62β). These findings suggest the contribution of the *o*-quinoid structure to the smaller E_1^{sum} and the instability of **3.2**.

3.4 NMR spectroscopy

3.4.1 Neutral 3.2

The ^{1}H NMR spectra of **3.2** gave rise to no peaks in aromatic region and showed only broad peaks at 1 - 2 ppm (Figure 3.4.1). At lower temperature, even –90 °C, these peaks were not changed dramatically. These broadening would be caused by the paramagnetic species formed by the oxidation of **3.2**. Mass spectroscopy supported the presence of the oxidized species giving a peak at *m/z* 640 (M^+ + 16). Unidentifiable radical species are also detected by ESR spectroscopy.

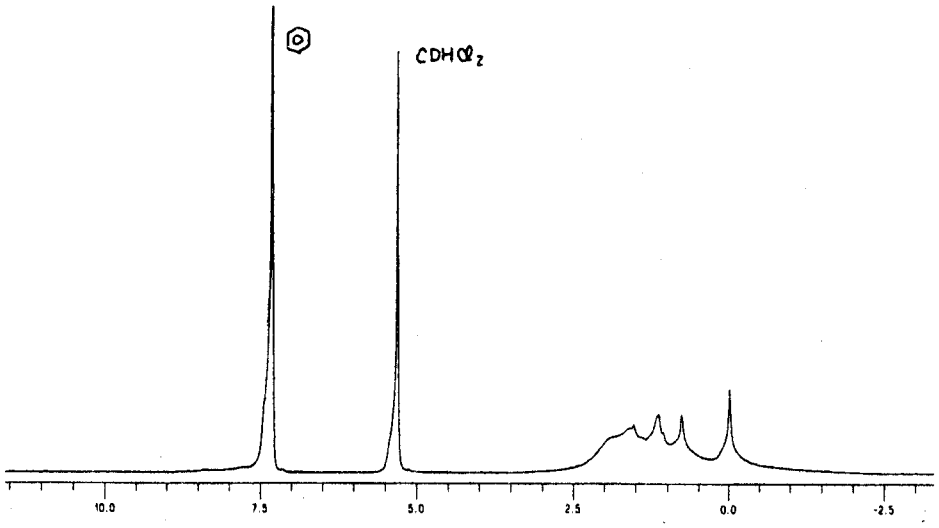

Figure 3.4.1. ^{1}H NMR spectrum of **3.2** in CD_2Cl_2 at –90 °C.

3.4.2 Dication 3.2^{2+}

Dissolution of **3.2** in concentrated D_2SO_4 gave dication species **3.2**$^{2+}$ as a red purple solution. Figure 3.4.2 shows the aromatic region of the ^{1}H NMR spectrum of the solution. The ^{1}H and ^{13}C NMR chemical shifts are given in Figure 3.4.3.

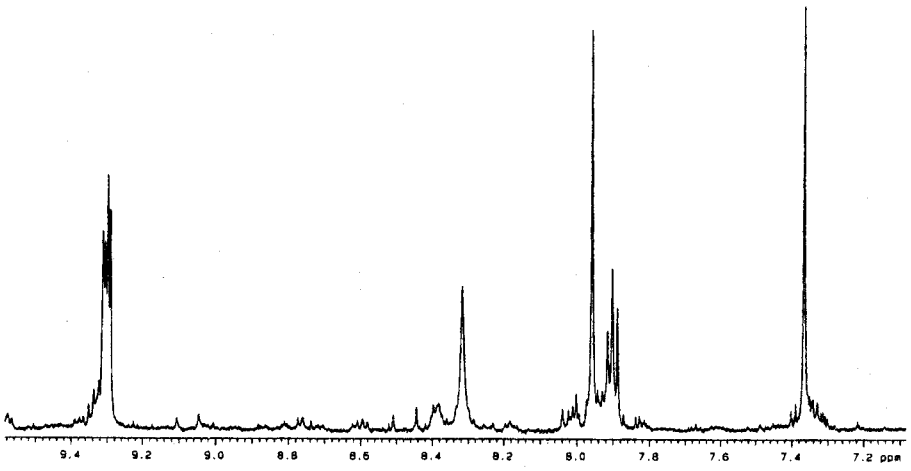

Figure 3.4.2. ^{1}H NMR spectrum of $\mathbf{3.2}^{2+}$ in D_2SO_4 at 60 °C.

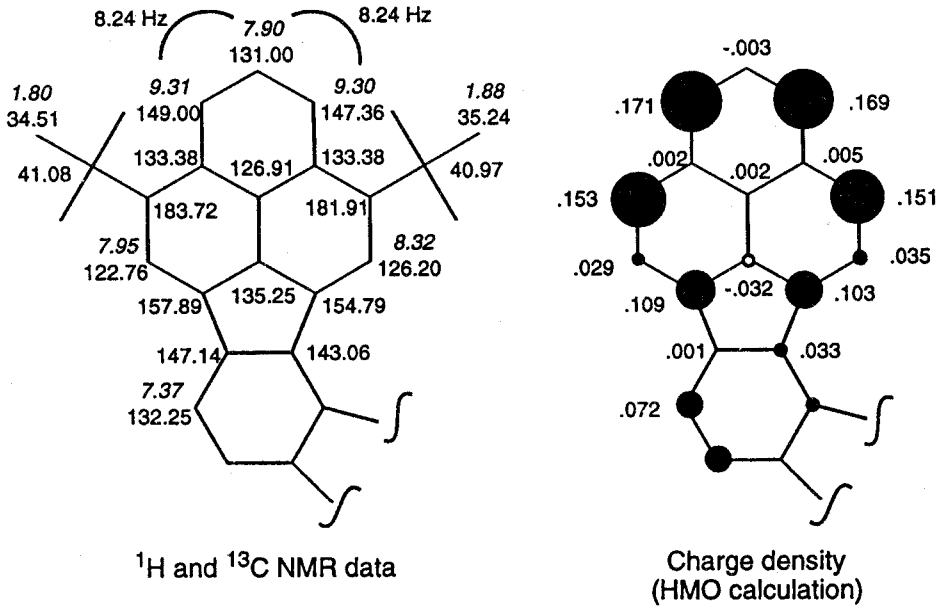

^{1}H and ^{13}C NMR data

Charge density
(HMO calculation)

Figure 3.4.3. NMR data and charge density of $\mathbf{3.2}^{2+}$

The ^{13}C NMR spectra reveals only minor differences in chemical shifts in comparison with those of $\mathbf{2.3}^{2+}$. This finding suggests the similar charge distribution in both dication species and a large contribution of the two phenalenyl units to the stability of $\mathbf{3.2}^{2+}$. In contrast, the ring protons of $\mathbf{3.2}^{2+}$ are more deshielded by about 0.5 ppm than those of $\mathbf{2.3}^{2+}$ except for H^{14} and H^{15}, which move to more downfield by the steric compression effect. The ring current calculations indicate the more weakly paramagnetic ring current on the *as*-indacene unit and the more strongly diatropic ring current on the two phenalenyl units than those of $\mathbf{2.3}^{2+}$ (Figure 3.4.4). The reason for the downfield shifts of the ring protons of $\mathbf{3.2}^{2+}$ compared to $\mathbf{2.3}^{2+}$ will be discussed in section 3.4.4.

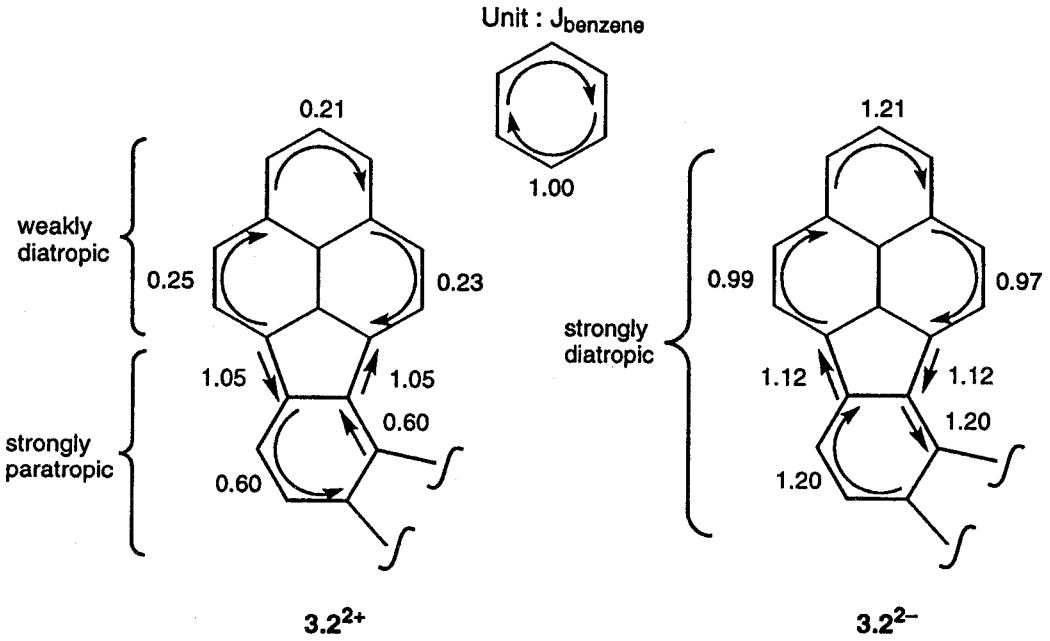

Figure 3.4.4. Ring current calculation of 3.2^{2+} and 3.2^{2-}

3.4.3 Dianion 3.2^{2-}

Treatment of dihydro compounds **3.10** with a potassium mirror in a sealed degassed tube at –78 °C yielded dianion species 3.2^{2-} as a deep yellowish red solution with yellow fluoresence. Figure 3.4.5 shows the aromatic region of the ^1H NMR spectrum of the solution. The ^1H and ^{13}C NMR chemical shifts are given in Figure 3.4.6.

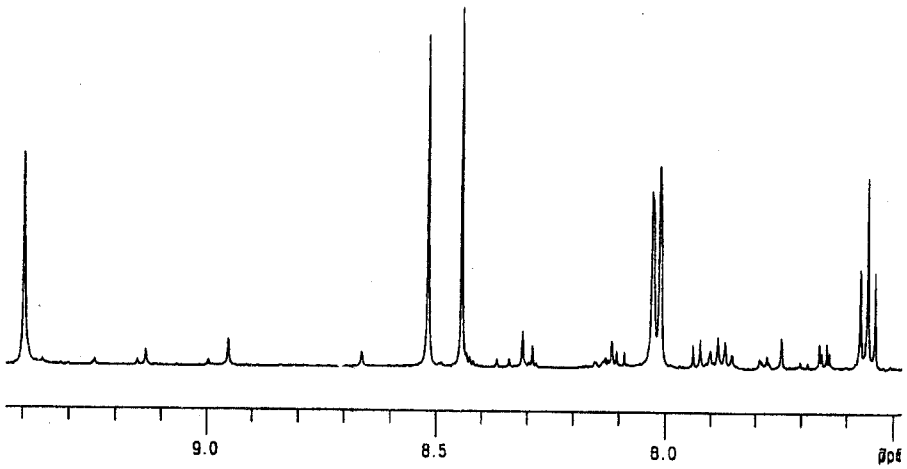

Figure 3.4.5. ^1H NMR spectrum of 3.2^{2-} in THF-d_8 at 30 °C.

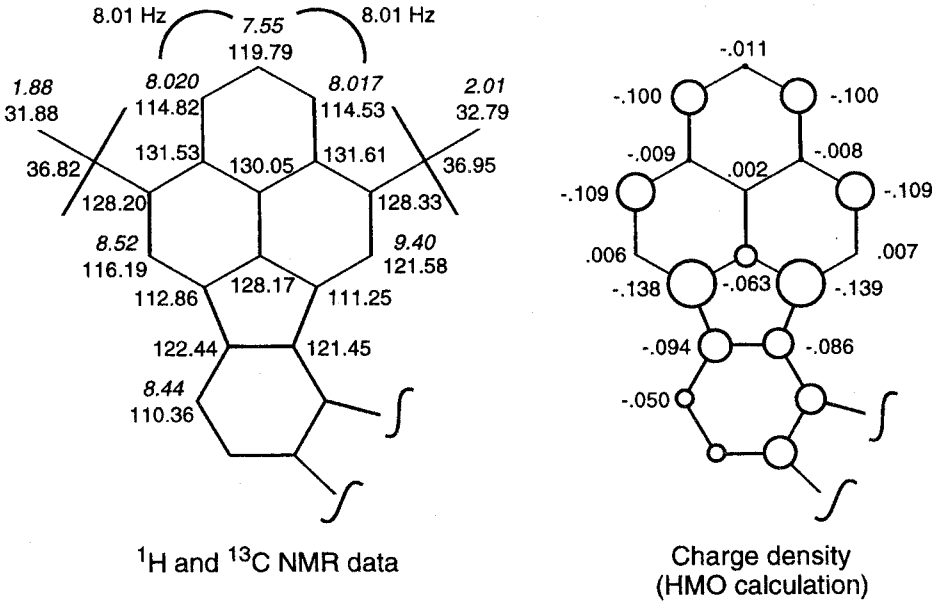

Figure 3.4.6. NMR data and charge density of $\mathbf{3.2^{2-}}$

The total ^{13}C chemical shift change of the sp^2 carbon on going from $\mathbf{3.2^{2+}}$ to $\mathbf{3.2^{2-}}$ is 725.68 ppm (or 181.42 ppm per electron), which supports the idea of complete generation of the dication and the dianion. Figure 3.4.7 shows the shift changes for the individual carbons on going from $\mathbf{3.2^{2+}}$ to $\mathbf{3.2^{2-}}$ and from $\mathbf{2.3^{2+}}$ and $\mathbf{2.3^{2-}}$.

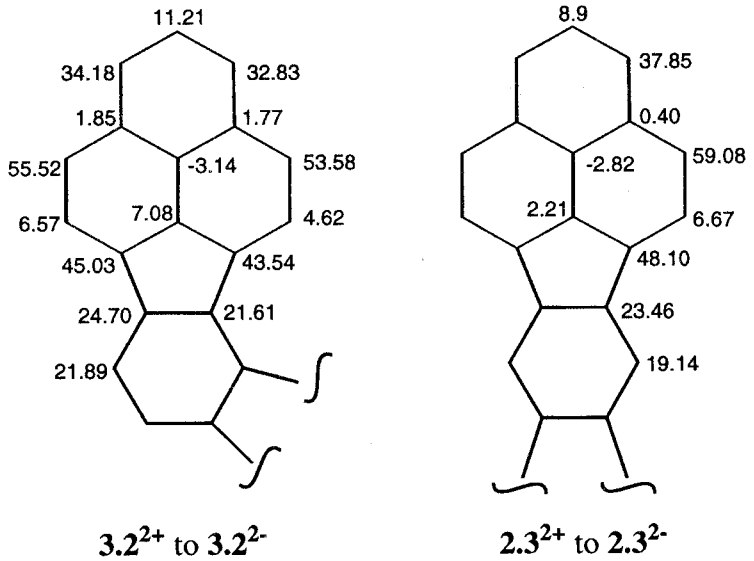

Figure 3.4.7. ^{13}C chemical shift changes on going from $\mathbf{3.2^{2+}}$ to $\mathbf{3.2^{2-}}$ and from $\mathbf{2.3^{2+}}$ and $\mathbf{2.3^{2-}}$.

The shift changes for **3.2** are similar to those for **2.3** : large at α-position and central benzene ring, and small at others. This finding clearly suggests that the charges mainly

reside on the α-position of the phenalenyl units, which largely contribute to the stability of not only **3.2**$^{2+}$ but also **3.2**$^{2-}$.

3.4.4 London–McWeeny ring current calculations [3]

Ring current calculations were performed by the computer software programmed by J. Aihara based on the equation (1), which gave the induced bond current, J_{ij}, in a bond i–j.

$$J_{lm} = 9I_0/S_0 \underbrace{[K_{lm}P_{lm}S_{lm}}_{\text{diamagnetic}} + \underbrace{K_{lm}\sum_{(l'm')}^{G} K_{l'm'}\bar{\pi}_{lm,l'm'}S_{l'm'}]}_{\text{paramagnetic}} \qquad (1)$$

G : an entire conjugated system of a planer mono- or poycyclic molecule
K_{lm} : resonance integral in bond l–m
P_{lm} : bond order in bond l–m
S_{lm} : signed area
$\bar{\pi}_{lm,l'm'}$: mutual imaginary bond–bond polarizability between bonds l–m and l'–m'

$$\bar{\pi}_{lm,l'm'} = \pi_{lm,l'm'} - \pi_{lm,m'l'} + \pi_{ml,l'm'} - \pi_{ml,m'l'} \qquad (2)$$

$$\pi_{lm,l'm'} = 2\sum_{J}^{occ}\sum_{K(\neq J)} \frac{C_{lJ}C_{mK}C_{l'K}C_{m'J}}{E_J - E_k} \qquad (3)$$

J : occupied orbital
K : unoccupied orbital

Equation (1) means " in any given molecules, the net ring current effect on a particular proton chemical shift may be a combination of both a paramagnetic and a diamagnetic contribution". Coulson and Mallion [4] applied this ring current model to test Trost's experimental deduction that the upfield shifts of pyracylene relative to the corresponding dihydro derivatives are due to a net paramagnetic current or, at least, a greatly diminished diamagnetic one.

Here I will apply this model to the ^{1}H NMR chemical shifts observed in IDPL and PDPL.

In general, paramagnetic ring current is known to be sensitive to the HOMO–LUMO gap, which is derived from the equation (3). Figure 3.4.8 shows the ^{1}H NMR spectra and the selected energy levels of diisopropyl IDPL **2.2** and PDPL. Clearly, PDPL exhibited ^{1}H NMR signals in higher-field region than **2.2**. However, the HOMO–LUMO gap of PDPL is larger than that of **2.2**.

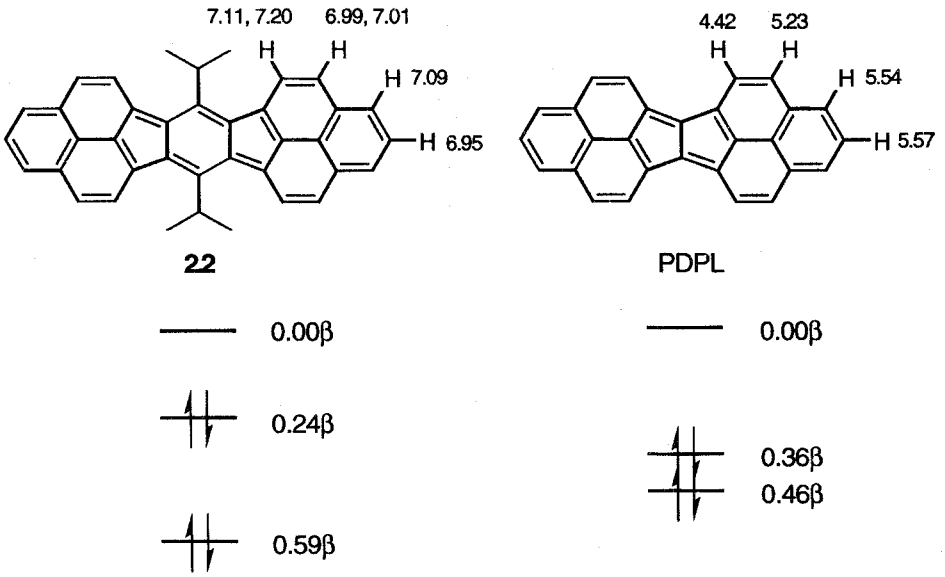

Figure 3.4.8. ^{1}H NMR spectra and the selected energy levels of diisopropyl IDPL **2.2** and PDPL

To remove contradiction to the "general rule" – *smaller HOMO–LUMO gap is responsible for more strongly paramagnetic effect,* the numerator of the equation (3) must be taken into consideration. The numerator, $C_{lJ}C_{mK}C_{l'K}C_{m'J}$, should represent the degree of the "movement" of an electron to a next atom in a transition from J to K; in other words, the degree of the deformation of electronic clouds in the transition (Figure 3.4.9).

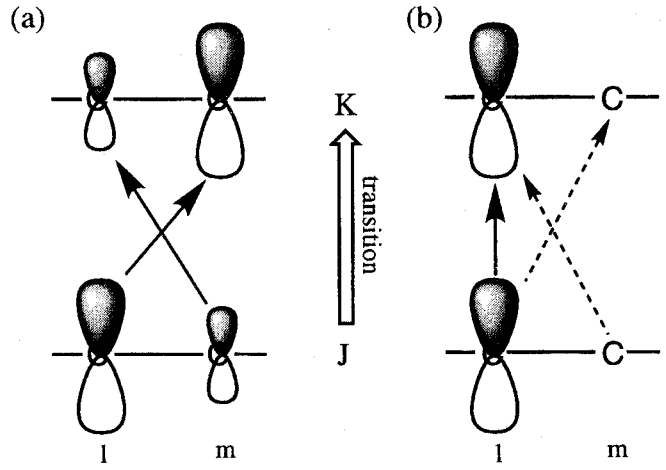

Figure 3.4.9. "movement" of an electron to a next atom in a transition from J to K

For IDPL and PDPL, since HOMO and LUMO retain NBMO character and spread over similar region in the phenalenyl units [corresponding to Figure 3.4.9 (b)], an electron can hardly "move" to neighbor atoms. In contrast, because NHOMO and

LUMO is localized largely in different parts of space [Figure 3.4.9 (a)], the deformation of electronic clouds should be large. Thus the transition with a large contribution to a paramagnetic ring current in IDPL and PDPL should be not HOMO→LUMO but NHOMO→LUMO accompanied with a large deformation of electronic clouds. The ring current calculations also support the evidence that ^{1}H NMR signals of PDPL with a smaller NHOMO–LUMO gap appear at higher field region than those of IDPL (Figure 3.4.10).

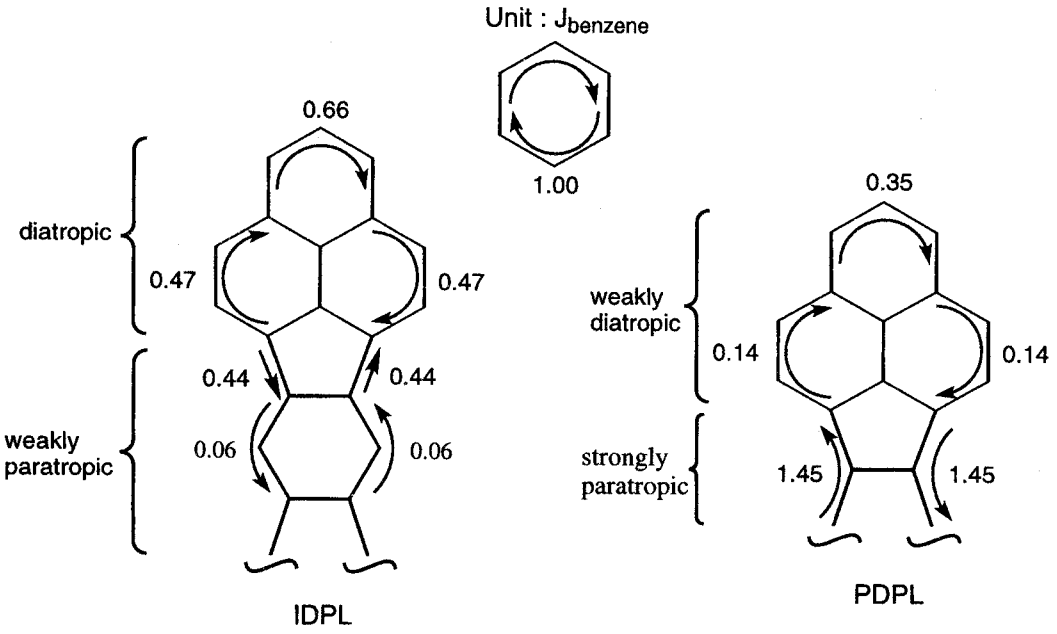

Figure 3.4.10. Ring current calculation of IDPL and PDPL

This model also can help to understand the lower-field shifts of the ring protons of **3.2**$^{2+}$ compared to **2.3**$^{2+}$ (Section 3.4.2). The larger HOMO(ψ_{15})–LUMO(ψ_{16}) gap of 0.515β for **3.2**$^{2+}$ should be responsible for a small contribution of paramagnetic effect than those of 0.352β for **2.3**$^{2+}$.

3.5 ESR spectroscopy

3.5.1 Radical cation 3.2$^{(\bullet)(+)}$

The CV data for **3.2** suggested the stability of **3.2**$^{(\bullet)(+)}$ and **3.2**$^{(\bullet)(-)}$ as the radical cation and the radical anion of **2.3**. The reaction of **3.2** with $SbCl_5$ in CH_2Cl_2 generated the radical cation **3.2**$^{(\bullet)(+)}$, which was found to be stable even at room temperature and gave rise to the well-resolved ESR spectra as shown in Figure 3.5.1. No detectable changes were observed in the spectra in the range of 213 – 273 K.

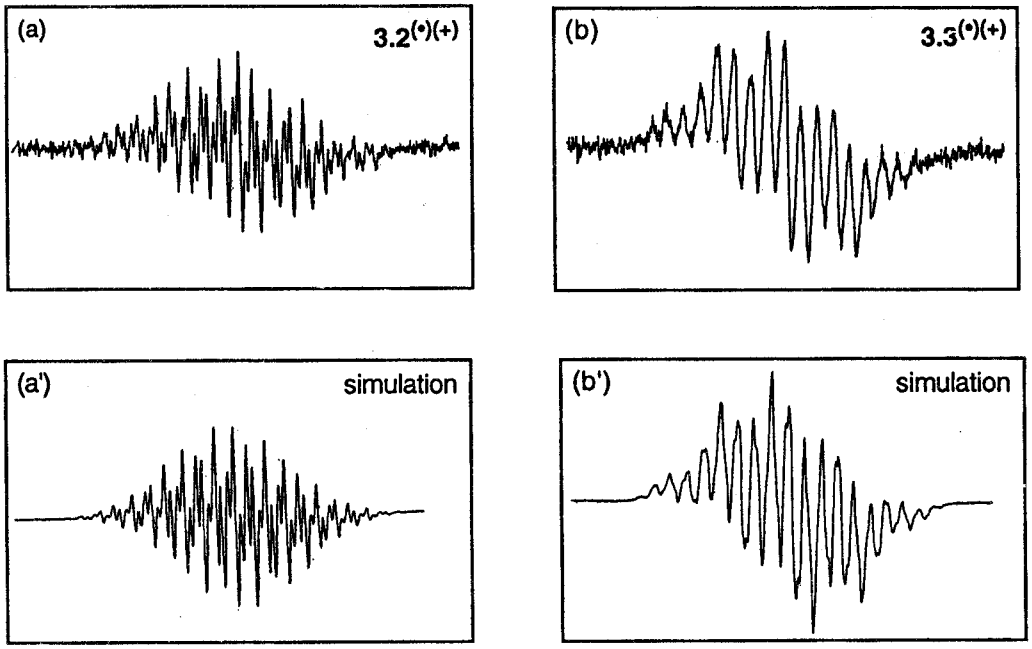

Figure 3.5.1. ESR spectra of (a) the radical cations of **3.2** and (b) deuterated derivative **3.3** generated with $SbCl_5$ in CH_2Cl_2 at - 70 °C, and the correspondig simulated spectra (a') and (b'), respectively.

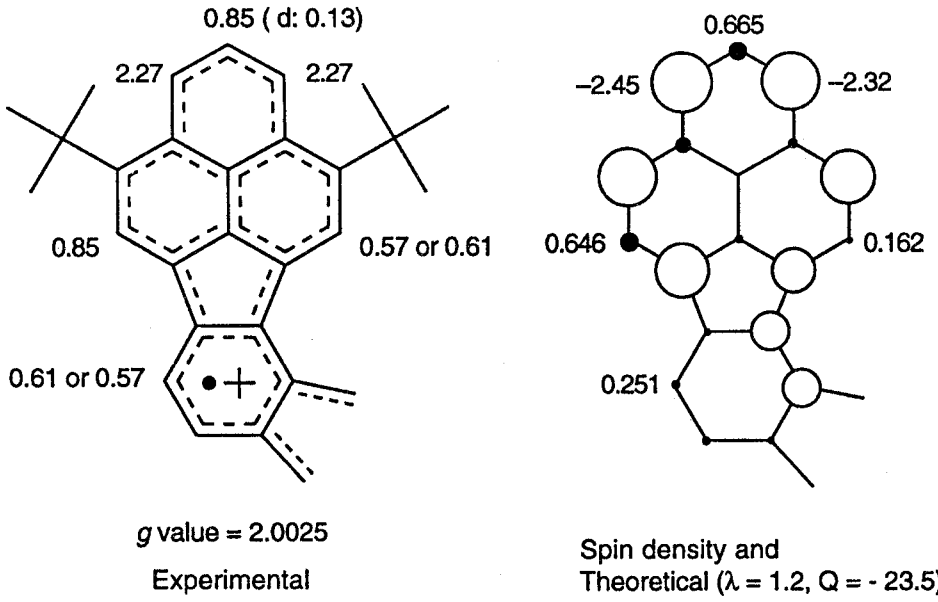

Figure 3.5.2. Experimental and theoretical hyperfine coupling constants (in G) along with spin density of **3.2**$^{(•)(+)}$ and **3.3**$^{(•)(+)}$. In parentheses, a coupling constant of deuteron. Open-circle and closed-circle represent positive and negative spin density, respectively.

The coupling constants of the ring protons are given in Figure 3.5.2 along with the spin density calculated by the HMO–McLachlan method ($\lambda = 1.2$). The assignment of the coupling constants is based on the calculated spin density, although the relatively

small magnitudes of $a_{H\mu}$ make such an assignment somewhat uncertain. However, the constants of H^2 and H^{11} could be confirmed by studies of the radical cation of the 2,10-dideuterated derivatives **3.3**. The deuterated compounds were synthesized following Scheme 3.5.1.

Scheme 3.5.1

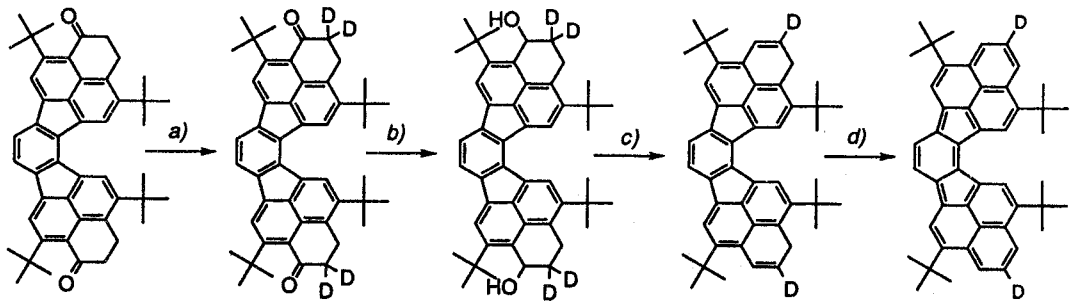

3.3

Reaction condition : *a)* CF_3COOD, CH_2Cl_2, rt, 1 d, 97%. *b)* $LiAlH_4$, THF, rt, 1 h, 73%. *c)* *p*-toluenesulfonic acid, benzene, reflux, 3 min, 90%. *d)* *p*-chloranil, benzene, reflux, 10 min.

3.5.2 Radical anion 3.2(•)(–)

The radical anion **3.2**$^{(\bullet)(-)}$ was obtained by the treatment of **3.2** with a K-mirror in THF. The radical anion was also stable and gave rise to the ESR spectra as shown in Figure 3.5.3. No detectable changes were observed in the spectra in the range of 213 – 273 K.

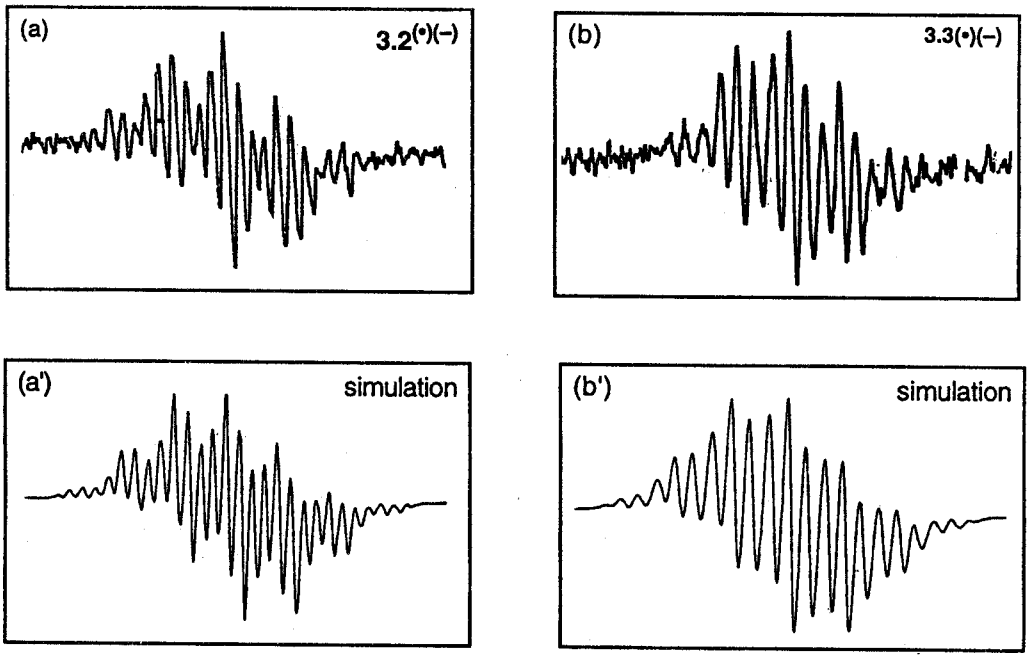

Figure 3.5.3. ESR spectra of (a) the radical anions of **3.2** and (b) deuterated derivative **3.3** generated with K–mirror in THF at - 30 °C, and the correspondig simulated spectra (a') and (b'), respectively.

Figure 3.5.4 shows the hyperfine coupling constants and the calculated spin density of **3.2**$^{(\bullet)(-)}$.

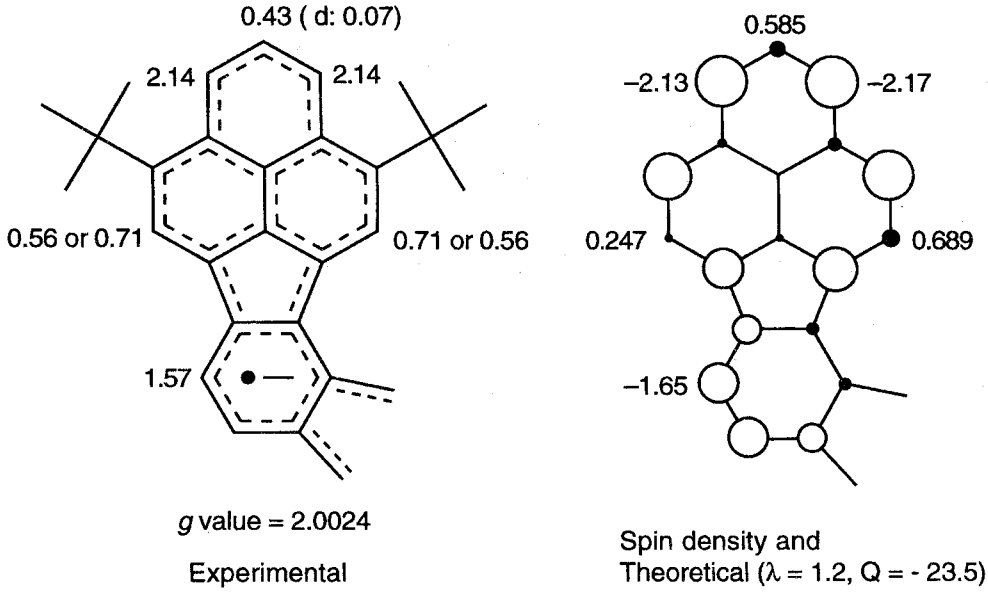

Figure 3.5.4. Experimental and theoretical hyperfine coupling constants (in G) along with spin density of **3.2**$^{(\bullet)(-)}$ and **3.3**$^{(\bullet)(-)}$. In parentheses, a coupling constant of deuteron. Open-circle and closed-circle represent positive and negative spin density, respectively.

In both radical species, the large coupling constants can be assigned to the α-positions, and the small ones to the β-positions; these are comparable to those of radical ions of **2.3**. However, uncertain assignments of the small coupling constants at the β-positons prevent the discussion about the electronic states of **3.2**$^{(\bullet)(+)}$ and **3.2**$^{(\bullet)(-)}$ in detail. On the basis of the HMO–McLachlan calculations, 87% and 77% of the π-spin resides on the two phenalenyl units in **3.2**$^{(\bullet)(+)}$ and **3.2**$^{(\bullet)(-)}$, respectively. Although π-spin density of **3.2**$^{(\bullet)(-)}$ is slightly smaller than that of **2.3**$^{(\bullet)(-)}$, the similalities of spin distribution between **3.2**(•)(+) and **2.3**(•)(+) or between **3.2**$^{(\bullet)(-)}$ and **2.3**$^{(\bullet)(-)}$ suggest that HOMO and LUMO of **3.2** should also retain a NBMO character to some extent.

3.5.3 neutral 3.2

The benzene solution of **3.2** gave rise to an intense ESR signal. The mass spectrum of **3.2** suggests that the species giving the ESR spectrum should be oxidized compounds of **3.2**. The computer simulation for this spectrum yielded three kinds of coupling constants, 4.70 G (2H), 1.58 G (4H), and 1.00 G (2H). Although ESR spectroscopy can not give any information to determine the structure of the radical in question, the radical observed may be generated by oxidation on a phenalenyl units of **3.2** (Figure 3.5.5). The spin distribution pattern will be similar to that of phenalenyl radical; 4.70 G at α-positon, and others at β-postion and central benzene ring.

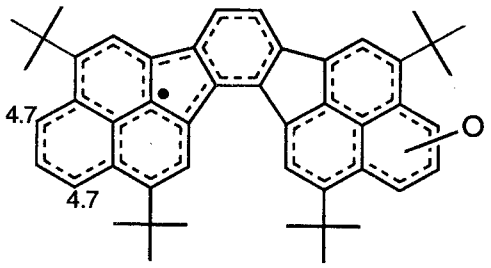

Figure 3.5.5. Suggested structure of paramagnetic species to give ESR signal in benzene solution of **3.2**

3.6 UV/Vis/NIR

3.6.1 Neutral 3.2

As described in section 2.4.1, TTB-IDPL **2.3** shows a beautiful green color and relatively simple electronic absorption spectrum. The simplicity of the spectrum suggests that allowed-transitions led to fobidden-ones due to the high symmetry, because many energy levels generally give a large number of transitions and make electronic spectrum complicated. In contrast to **2.3**, TTB-*as*-IDPL **3.2** was found to show a dark greenish brown color and the complicated UV spectrum. The lower symmetry of **3.2** would cause changes from forbidden to allowed transitions and give rise to many transitions in the UV spectrum. Figure 3.6.1 shows the electronic absorption spectra of the five redox states of **3.2**, while table 3.6.1 lists the wavelengths of the band maxima.

Table 3.6.1 Maxima, λ_{max} (in nm), of electronic bands for the five redox states of **3.2**

3.2^{2+}	**3.2**$^{(\bullet)(+)}$	**3.2**	**3.2**$^{(\bullet)(-)}$	**3.2**$^{2-}$
419	361	270	280	276
495	469	304	328	320
535	625	326	374	370
664	787	352	514	484
752	880	406	578	520
	~1120	442	628	
	~1250	496	706	
		572	862	
		618	~940	
		658		
		726		
		1054		
		1242		

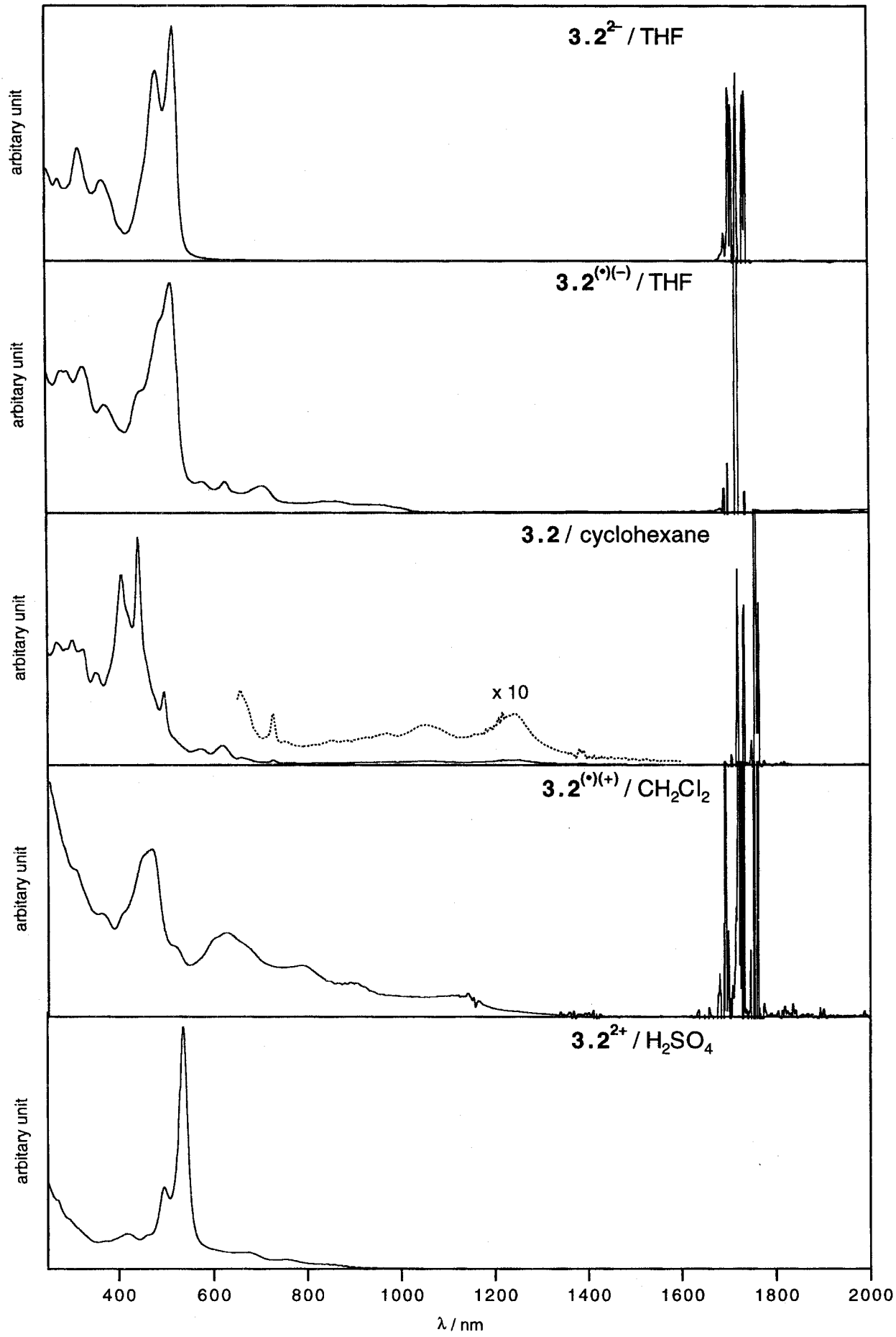

Figure 3.6.1. Electronic absorprion spectra of the five redox states of **3.2**

The electronic spectra of **3.2** contains the broad and weak terminal absorption at 1242 nm, which should correspond to the HOMO–LUMO transition. In order to assign the electronic bands to transition between orbitals, INDO/S CI calculations were performed (Table 3.6.2). In each case, the ten highest occupied and ten lowest unoccupied orbitals were used for configuration interaction. Figure 3.6.2 presents schematically the calculated SCF energy levels fo the six relevant highest occupied or lowest unoccupied orbitals for the five redox states of **3.2**.

Table 3.6.2. Selected electronic transition data for five redox states of **3.2** calculated by the INDO/S CI method and assignments of the observed electronic bands.

	theoretical				experimental
	symmetry label [e]	ΔE, eV	oscillator strength	substantial contribution [a], %	λ, nm; ΔE,eV
3.2^{2+}	B_2 (y)	2.05	0.00	b_1 (ψ_{17}), ← a_2 (ψ_{15}), 64	*b*
				a_2 (ψ_{16}), ← b_1 (ψ_{14}), 26	
	A_1 (z)	2.09	0.06	a_2 (ψ_{16}), ← a_2 (ψ_{15}), 72	*b*
				b_1 (ψ_{17}), ← b_1 (ψ_{14}), 16	
3.2$^{(\bullet)(+)}$ [c]		0.86	0.00	b_1 (ψ_{17}) ← a_2 (ψ_{16}), 78	
				b_1 (ψ_{17}) ← b_1 (ψ_{14}), 12	
3.2	B_2 (y)	1.05	0.31	b_1 (ψ_{17}) ← a_2 (ψ_{16}), 86	1242; 1.00
				b_1 (ψ_{17}) ← b_1 (ψ_{14}), 9	
	B_2 (y)	2.02	0.09	b_1 (ψ_{17}) ← a_2 (ψ_{15}), 91	726; 1.71
3.2$^{(\bullet)(-)}$ [c]		0.79	0.00	b_1 (ψ_{17}) ← a_2 (ψ_{16}), 76	
				b_1 (ψ_{17}) ← b_1 (ψ_{14}), 6	
3.2^{2-}	B_2 (y)	2.62	0.94	b_1 (ψ_{18}) ← a_2 (ψ_{16}), 74	520; 2.38
	B_2 (y)	2.70	0.58	a_2 (ψ_{19}) ← b_1 (ψ_{17}), 66	*d*
	A_1 (z)	2.73	0.09	b_1 (ψ_{18}) ← b_1 (ψ_{17}), 53	*d*
				a_2 (ψ_{19}) ← a_2 (ψ_{16}), 34	

[a] In parentheses, the molecular orbitals calculated by the HMO method. See Figure 3.1.2. [b] Could not be assigned due to the weak and broad peaks. [c] The optimized strucure routine of INDO/S predicted the deviation of the strucuture from C_{2v} and localization of the unpaired electron on a phenalenyl unit. [d] Could not be observed due to the intense band at 520 nm. [e] In parentheses, the direction of the induced transition dipole. The choice of the axes in C_{2v} symmetry is specified in Fiugre 3.1.2.

Although the NHOMO–LUMO transition should correspond to the absorption at 726 nm on the basis of the calculations, the presence of many weak absorption at 490 – 730 nm prevents the certain assignment of the peak. In contrast to **2.3**, the longest-wavelength absorption is due to HOMO→LUMO excitation and NHOMO→LUMO

absorption with larger energy differences appears in shorter wavelength region. Compared to **2.3**, the smaller HOMO–LUMO gap of **3.2**, which is supported by the smaller E_1^{sum}, should be responsible for the bathochromic shift of HOMO–LUMO transition, while the hypsochromic shift of NHOMO–LUMO transition would be caused by the larger ovelap integral, *i.e.* larger K_{ab}, between ψ_{15} and ψ_{17} due to the lower symmetry; large overlaps are mainly found at the central benzene unit.

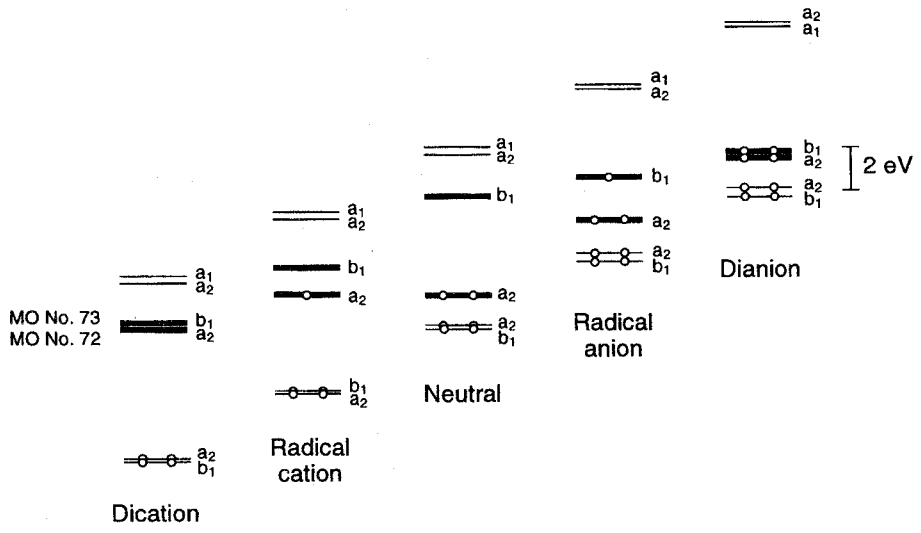

Figure 3.6.2 Energy levels of several occupied and unoccupied MOs in the five redox stages of *as*-IDPL **3.1**, as calculated by the MOPAC6/PM3 method. The optimized structures are in C_{2v} symmetry for all states. The bold lines represent HOMO and LUMO of neutral state.

3.6.2 Radical cation **3.2**$^{(\bullet)(+)}$ *and radical anion* **3.2**$^{(\bullet)(-)}$

Although **2.3**$^{(\bullet)(+)}$ and **2.3**$^{(\bullet)(-)}$ gave rise to intense absorptions in considerably long-wavelength region, the absorption of **3.2**$^{(\bullet)(+)}$ and **3.2**$^{(\bullet)(-)}$ terminated at relatively shorter-wavelength region as shown in Figure 3.6.1. On the other hand, the INDO/S calculations predicted relatively weak absorptions near 1500 nm. However, this prediction remains still questionable, because optimized structure by the INDO/S calculations deviated from C_{2v} symmetry and the unpaired electron "localized" on a phenalenyl unit, which contradicted the ESR studies suggesting the delocalization of the spin over the entire molecule. In contrast, the PM3 calculations predicted the C_{2v} structure and the delocalization of the spin over the entire molecule. The CI calculations by the INDO/S method using the structure optimized by the INDO/S method indicated that the NIR band should be a "forbidden" transition (oscillator strength, f = 0.00), while those using the structure optimized by the PM3 method suggested a "partially allowed" NIR transition ($f \approx 0.05$).

In conclusion, the ESR studies of **3.2**$^{(\bullet)(+)}$ and **3.2**$^{(\bullet)(-)}$ at 210 – 273 K indicate that these radicals should have an effective C_{2v} symmetry, whereas no or considerably weak

absorptions near 1600 nm support the idea that the spin should essentially "localize" on a phenalenyl unit and the time-averaged C_{2v} structure might give the ESR spectra observed. At present, we must await detailed studies for further discussions.

3.6.3 Dication $\mathbf{3.2^{2+}}$ *and dianion* $\mathbf{3.2^{2-}}$

The divalent species, $\mathbf{3.2^{2+}}$ and $\mathbf{3.2^{2-}}$, exhibited the relatively simple absorption spectra as shown in Figure 3.6.1. However, the assignment of each absorptions with unresolved spectra remains still uncertain.

The intense band of $\mathbf{3.2^{2+}}$ at 535 nm is flanked on the long-wave side by weak bands at 550 – 900 nm, which terminate at longer-wavelength region than those of $\mathbf{2.3^{2+}}$. The INDO/S calculations predict two nearly degenerate transitions at 593 and 606 nm; the former is due to HOMO (ψ_{15}) → LUMO (ψ_{16}) transition and the latter HOMO (ψ_{15}) → NLUMO (ψ_{17}). Although this prediction is also supported by the PPP CI methods, the assignment of the longest-wavelength absorption to the HOMO → NLUMO transition remains still questionable. However, the small energy differences between S_2 and S_1 state suggest the small gap between ψ_{16} and ψ_{17}, which correspond to HOMO and LUMO of neutral **3.2**, respectively.

The THF solution of $\mathbf{3.2^{2-}}$ exhibited a bright orange color and an intense band at 520 nm. These absorptions terminated at the shortest-wavelength among five redox states of **3.2**. This finding suggests the large HOMO–LUMO gap for $\mathbf{3.2^{2-}}$ and is consistent with the down-field shifts of the ring protons in the ^{1}H NMR spectrum.

On the basis of the calculations, the NHOMO→LUMO transition should contribute largely to the longest wavelength absorption. The calculated oscillator strength (f = 0.91) will make this assignment undoubted, because the calculated intensity is generally a good guide for the identification of the observed bands. Furthermore, the calculations indicated that the transition in which both HOMO and LUMO of $\mathbf{3.2^{2-}}$ participate should be z-polarized and partially allowed (f = 0.09). In contrast, the longest-wavelength bands of $\mathbf{2.3^{2-}}$ due to the HOMO–LUMO transition is x-polarized and fully allowed (f = 1.37) as shown in Table 2.5.2. The HOMO (b_1)→LUMO (b_1) transition of $\mathbf{3.2^{2-}}$ is theoretically predicted to be polarized parallel to the *short* axis of the molecule (z-polarized), and thus the transition dipole moment will hardly be large. Unfortunately, the weak absorption predicted could not be observed due to the intense first band.

3.7 Conclusion

In chapter 2 and 3, I discussed the properties of TTB-IDPL **2.3** and TTB-*as*-IDPL **3.2** as four-stage amphoteric redox systems. In spite of differences in the shape and symmetry (D_{2h} and C_{2v}), the feature of the basic π-electronic structure in ground state

was essentially maintained on going from **2.3** to **3.2**. The physical and chemical properties as redox systems primarily depended on the NBMO character of the frontier orbitals. The NBMO character was shown by the charge or spin distributions extracted from ^{13}C NMR or ESR studies, respectively. These studies indicated that the charges and the spin mainly resided on α-position in phenalenyl units and the distribution pattern of them was similar to that of phenalenyl species.

The small E_1^{sum} value of **3.2** was also related to the NBMO character of the frontier orbitals, because the large extent of NBMO character would be responsible for the small HOMO–LUMO gap.

However, the electronic spectra exhibited the large differences between **2.3** and **3.2**. The five redox states of **2.3** gave the relatively simple spectra and the assignment of the peaks is undoubted. In contrast, those of **3.2** showed complicated spectra, which make the assignment of the peaks uncertain. The occurrence of many weak and broad absorptions was in line with the lowering of the symmetry ($D_{2h} \rightarrow C_{2v}$), which caused the change from "forbidden" to "allowed " or "partially allowed" transitions.

Thus in spite of the differences in the symmetry, both **2.3** and **3.2** were found to behave as four-stage amphoteric redox systems, in which phenalenyl units played a most important role in exhibiting amphoteric redox properties. The both compounds showed similar properties in ground state. However, in the case of mixing a ground state configuration with some excited state configurations, the both compounds exhibited largely different properties.

3.8 Experimental section

Scheme 3.8.1 shows the synthetic procedure for 4,7-di-*tert*-butyl-5-methylacenaphthylene (**2.5**).

Scheme 3.8.1. Synthetic procedure of **2.5**

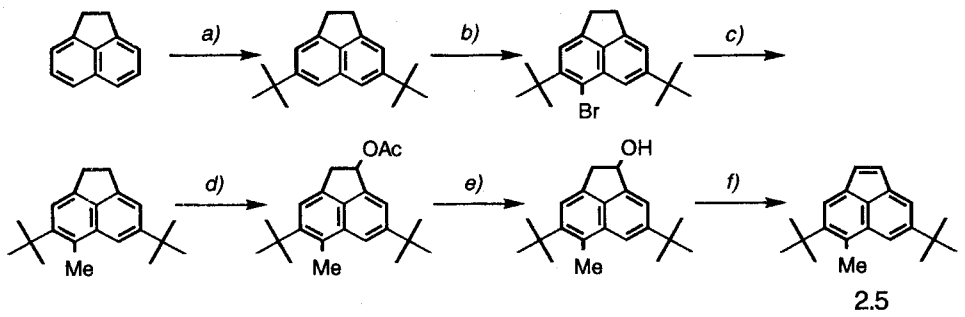

Reaction conditions : a) ^{t}BuCl, $AlCl_3$, CH_2Cl_2, rt, 3 h, 64%. *b)* NBS, DMF, rt, 38 h, 43%. *c)* 1) ^{n}BuLi, 2) MeI,THF, -78°C to rt, 12 h, 94%. *d)* Pb_3O_4, AcOH+benzene, reflux, 2 h, 93%. *e)* KOH, EtOH+H_2O, reflux, 1 h, 94%. *f)*cat. *p*-toluenesulfonic acid, benzene, reflux, 20 min, 91%.

2,7-Di-*tert*-butylacenaphthene. To a mixture of acenaphthene (50.0 g, 324 mmol) and *tert*-butyl chloride (76 mL, 699 mmol) in dichloromethane (200 mL) was added $AlCl_3$ (7.6 g, 57 mmol) and the mixture was stirred for 90 min at room temperature. Additional *tert*-butyl chloride (5 mL, 46 mmol) was added and the mixture was stirred for 90 min. The mixture was poured into ice-water and the organic layer was separated. The aqueous layer was extracted repeatedly with CH_2Cl_2. The combined organic layers were washed with saturated aqueous $NaHCO_3$, dried over $MgSO_4$ and filtered. After the solvent was removed, pure di-*tert*-butylacenaphthene (54.9 g, 64%) was obtained by column chromatography on silica gel [benzene/hexane (1:4, v/v)] and subsequent recrystallization (ethanol + hexane). ^1H NMR (270 MHz, $CDCl_3$) δ 7.51 (s, 2H); 7.32 (s, 2H); 3.37 (s, 4H); 1.40 (s, 18H).

4,7-Di-*tert*-butyl-5-bromoacenaphthene. A suspension of *N*-bromosuccinimide (36.2 g, 203 mmol) and di-*tert*-butylacenaphthene (44.9 g, 168 mmol) in DMF (900 mL) was stirred for 26 h. Additional *N*-bromosuccinimide (10.4 g, 58 mmol) was added and the mixture was stirred for 12 h. The mixture was poured into a mixture of hexane (300 mL) and water (300 mL) and the organic layer was separated, washed with saturated aqueous $NaHCO_3$, dried over $MgSO_4$, and filtered. Pure di-*tert*-butylbromoacenaphthene (25.2 g, 43%) was obtained by column chromatography on silica gel (hexane) and subsequent recrystallization (hexane): mp 148.5 – 150.0 °C. ^1H NMR (270 MHz, $CDCl_3$) δ 7.97 (br s, 1H); 7.42 (s, 1H); 7.37 (d, J = 1.3 Hz, 1H); 3.40 – 3.26 (m, 4H); 1.64 (s, 9H); 1.43 (s, 9H). EI MS *m/z* 344, 346 (M^+). Anal. Calcd for $C_{20}H_{25}Br$: C, 69.56; H, 7.30. Found: C, 69.71; H, 7.37.

4,7-Di-*tert*-butyl-5-methylacenaphthene. *n*-Butyllithium (18.5 mL, 29.6 mmol, 1.6 M in hexane) was added to a solution of di-*tert*-butylbromoacenaphthene (9.64 g, 27.9 mmol) in 160 mL of THF at –78 °C. After the mixture was stirred for 30 min, methyl iodide (3.8 mL, 61.1 mmol) was added. The reaction mixture was allowed to warm to room temperature over 12h. Saturated aqueous ammonium chloride solution (20 mL) and benzene (50 mL) were added to the reaction mixture. The organic layer was separated and the aqueous layer was extracted repeatedly with benzene. The combined organic layers were washed with brine, dried over Na_2SO_4 and filtered. After evaporation of the solvent, purification by column chromatography on silica gel (hexane) followed by recrystallization (hexane) gave pure di-*tert*-butylmethylacenaphthene (7.38 g, 94%): mp 179.0 – 180.5 °C. ^1H NMR (270 MHz, $CDCl_3$) δ 7.67 (s, 1H); 7.38 (s, 1H); 7.33 (s, 1H); 3.31 (br s, 4H); 2.79 (s, 3H); 1.51 (s, 9H); 1.42 (s, 9H). EI MS *m/z* 280 (M^+). Anal. Calcd for $C_{21}H_{28}$: C, 89.94; H, 10.06. Found: C, 89.80; H, 10.10.

A mixture of 4,7-di-*tert*-butyl-1-acetoxy-5-methylacenaphthene and 4,7-di-*tert*-butyl-1-acetoxy-6-methylacenaphthene. A suspension of di-*tert*-butylmethylacenaphthene (10.0 g, 35.7 mmol) in acetic acid (75 mL) and benzene (50 mL) was heated at 90 °C. To the mixture was added Pb_3O_4 (25.90 g, 37.8 mmol) over 20 min and the mixture was refluxed for 2 h. After cooling, the mixture was poured into 200 mL of water and extracted with ether. The organic layer was washed with saturated aqueous $NaHCO_3$ and brine, dried over Na_2SO_4, and filtered. After evaporation of the solvent, the crude product was purified by column chromatography on silica gel (hexane) to give di-*tert*-butylacetoxymethylacenaphthene (10.9 g, 93%) as an yellow oil . ^1H NMR (270 MHz, $CDCl_3$) δ 7.88, 7.75 (br s, br s, 1H); 7.60, 7.38 (br s, d, J = 1.3 Hz, 1H); 7.65, 7.43 (s, s, 1H); 6.62–6.54 (m, 1H); 3.87–3.75 (m, 1H); 3.37–3.20 (m, 1H); 2.86, 2.83 (s, s, 3H); 2.09 (s, 3H); 1.53, 1.52 (s, s, 9H); 1.43, 1.42 (s, s, 9H).

A mixture of 4,7-di-*tert*-butyl-5-methylacenaphthen-1-ol and 4,7-di-*tert*-butyl-6-methylacenaphthen-1-ol. A mixture of di-*tert*-butylacetoxymethylacenaphthene (9.43 g, 33.6 mmol) in 10% aqueous KOH solution (50 mL) and ethanol (120 mL) was refluxed for 1h. After cooling, the mixture was poured into 150 mL of water. The resulting precipitate was collected, washed with water, and dried to yield crude di-*tert*-butylmethylacenaphthenol (7.73 g, 94%): mp 170.0 – 175.0 °C. ^1H NMR (270 MHz, $CDCl_3$) δ 7.85, 7.74 (br s, br s, 1H); 7.66, 7.42 (s, s, 1H); 7.62, 7.38 (br s, br s, 1H); 5.68 (m, 1H); 3.77 (dd, J = 17.5, 6.9 Hz, 1H); 3.21(br d, J = 17.5 Hz, 1H); 2.86, 2.84 (s, s, 3H); 1.54, 1.53 (s, s, 9H); 1.44, 1.43 (s, s, 9H). EI MS *m/z* 296 (M^+). Anal. Calcd for $C_{21}H_{28}O$: C, 85.08; H, 9.52. Found: C, 84.94; H, 9.59.

4,7-Di-*tert*-butyl-5-methylacenaphthylene (2.5). To a refluxing solution of di-*tert*-butylmethylacenaphthenol (201 mg, 678 μmol) in benzene (70 mL) was added *p*-toluenesulfonic acid monohydrate (15 mg) and the reaction mixture was stirred for 20 min. The mixture was cooled on ice-bath, washed with saturated aqueous $NaHCO_3$ and brine, dried over $MgSO_4$, and filtered. After evaporation of the solvent, the crude product was purified by column chromatography on silica gel (hexane) to give **2** (172 mg, 91%). ^1H NMR (270 MHz, $CDCl_3$) δ 7.98 (d, J = 1.0 Hz, 1H); 7.76 (s, 1H); 7.73 (d, J = 1.0 Hz, 1H); 6.98 (d, J=5.1 Hz, 1H); 6.93 (d, J=5.1 Hz, 1H); 2.97 (s, 3H); 1.53 (s, 9H); 1.45 (s, 9H). EI MS *m/z* 278 (M^+).

A mixture of 2,6,9,12-tetra-*tert*-butyl-1,7-dimethyldiacenaphtho[1,2-*b*: 1',2'-*d*]thiophene, 2,6,9,12-tetra-*tert*-butyl-1,8-dimethyldiacenaphtho[1,2-*b*: 1',2'-*d*]thiophene, and 2,6,9,12-tetra-*tert*-butyl-8,13-dimethyldiacenaphtho[1,2-*b*: 1',2'-*d*]thiophene (3.3).

A suspention of **2.5** (4.16 g, 14.9 mmol) and sulfur (1.92 g, 7.45 mmol) in 70 mL of DMF was heated at 135 °C for 3h. The reaction mixture was cooled and dichloromethane was added to the mixture. The organic layer was separated and the aqueous layer was extracted repeatedly with a small amount of dichloromethane. The combined organic layers were dried over $MgSO_4$ and filtered. After evaporation of the solvent, column chromatography on silica gel [benzene/hexane (1:20, v/v)] followed by recrystallization from CH_2Cl_2+hexane gave pure **3.3** (2.82 mg, 65%) .

A mixture of 2,7,10,13- tetra-*tert*-butyl-1,8-dimethyl-4,5-acenaphtho[1,2-*j*]fluoranthenedicarboxylic anhydride, 2,7,10,13-tetra-*tert*-butyl-1,9-dimethyl-4,5-acenaphtho[1,2-*j*]fluoranthenedicarboxylic anhydride, and 2,7,10,13-tetra-*tert*-butyl-9,14-dimethyl-4,5-acenaphtho[1,2-*j*]fluoranthenedicarboxylic anhydride (3.4). A mixture of **3.3** (1.60g, 2.74 mmol) and maleic anhydride (4.8g, 48.9 mmol) was heated at 230 °C for 30 minutes. The reaction mixture was cooled and heated with water. The undissolved solid was filtered off, dried, and boiled with 10 ml of potassium hydroxide solution (5%). The yellow compound **3.4** (1.41g, 2.17 mmol) was filtered and dried. Yield 79 %. m.p. >300°C. ^{1}H NMR (270 MHz, $CDCl_3$) δ 9.41, 9.38, 9.36, 9.32 (s, s, s, s, 2H); 9.03, 9.01, 8.95, 8.88 (s, s, s, s, 2H); 8.29, 8.23 (s, s, 2H); 3.14, 3.12, 3.10 (s, s, s, 6H); 1.80, 1.74, 1.68, 1.67, 1.66, 1.57, 1.53 (s, s, s, s, s, s, s, 36H). FAB MS (NBA) *m/z* 648 (M^+). IR (KBr) 2961, 1827, 1806, 1764 cm^{-1}.

A mixture of 2,7,10,13- tetra-*tert*-butyl-1,8-dimethylacenaphtho[1,2-*j*]fluoranthene, 2,7,10,13-tetra-*tert*-butyl-1,9-dimethylacenaphtho[1,2-*j*]fluoranthene, and 2,7,10,13-tetra-*tert*-butyl-9,14-dimethylacenaphtho[1,2-*j*]fluoranthene (3.5). A mixture of **3.4** (416 mg, 641 mmol) and basic $CuCO_3$ (168 mg) in 4.2 ml of quinoline was refluxed for 3 hour. The reaction mixture was cooled and poured into 2N hydrochloric acid. Dichloromethane was added to the mixture, and the organic layer was separated and the aqueous layer was extracted repeatedly with a small amount of dichloromethane. The combined organic layers were dried over Na_2SO_4 and filtered. After evaporation of the solvent, the crude product was purified by column chromatography on silica gel [benzene/hexane (1:10, v/v)] to give **3.5** (280 mg, 55%) . m.p. >300°C. ^{1}H NMR (270 MHz, $CDCl_3$) δ 8.79, 8.71, 8.66 (s, s, s, 2H); 7.82-8.09 (m, 6H); 3.06, 3.05, 3.03 (s, s, s, 6H); 1.76, 1.72, 1.65, 1.63, 1.62, 1.54 (s, s, s, s, s, s, 36H). FAB MS (NBA) *m/z* 578 (M^+). Anal. Calcd for $C_{44}H_{50}$: C, 91.29; H, 8.31. Found: C, 91.15; H, 8.66.

A mixture of 2,7,10,13- tetra-*tert*-butyl-1,8-bis(bromomethyl)acenaphtho[1,2-*j*]fluoranthene, 2,7,10,13-tetra-*tert*-butyl-1,9-bis(bromomethyl)acenaphtho[1,2-

***j*]fluoranthene, and 2,7,10,13-tetra-*tert*-butyl-9,14-bis(bromomethyl)acenaphtho [1,2-*j*]fluoranthene (3.6).** A mixture of compound **3.5** (143 mg, 247 μmol), *N*-bromosuccinimide (96.6 mg, 543 μmol), and benzoylperoxid (13.2 mg, 54 μmol) in 21 ml of benzene was refluxed for 10 min. The reaction mixture was concentrated *in vacuo* and 5 ml of *n*-hexane was added. The resulting colorless precipitate was removed by filtration and the filtrate was concentrated *in vacuo* to give crude **3.6.** ^{1}H NMR (270 MHz, $CDCl_3$) δ 8.72, 8.71, 8.63, 8.58 (s, s, s, s, 2H); 8.26, 8.20, (s, s, 2H); 8.03, 8.02 (s, s, 2H); 7.94, 7.92, 7.90 (s, s, s, 2H); 5.50, 5.49 (s, s, 4H); 1.81, 1.77, 1.68, 1.66, 1.63, 1.55 (s, s, s, s, s, s, 36H).

A mixture of 2,7,10,13- tetra-*tert*-butyl-1,8-bis[2,2-bis(ethoxycarbonyl) ethyl]acenaphtho[1,2-*j*]fluoranthene, 2,7,10,13-tetra-*tert*-butyl-1,9-bis[2,2-bis(ethoxycarbonyl) ethyl]acenaphtho[1,2-*j*]fluoranthene, and 2,7,10,13-tetra-*tert*-butyl-9,14-bis[2,2-bis(ethoxycarbonyl) ethyl]acenaphtho [1,2-*j*]fluoranthene (3.7). Diethyl malonate (0.16 ml, 1.05 mmol) was added to a sodium ethoxide solution freshly prepared from 11 ml of anhydrous ethanol and sodium (23.6 mg, 1.03 mmol). To the clear solution was added **3.6** dissolved in benzene (11 ml). After stirring for 17 h, the reaction mixture was washed with water. The organic layer was separated and the aqueous layer was extracted repeatedly with a small amount of *n*-hexane. The combined organic layers were dried over $MgSO_4$ and filtered. After evaporation of the solvent, the crude product was purified by column chromatography on silica gel (benzene) to give **3.7** (137 mg, 62%) . ^{1}H NMR (270 MHz, $CDCl_3$) 8.81, 8.76, 8.70, 8.67 (s, s, s, s, 2H); 8.12, 8.03, 8.02–7.91 (s, d, m, 6H); 4.24 (dd, 4H); 4.17–3.93 (m, 8H); 3.84–3.77 (m,2H); 1.75, 1.72, 1.63, 1.62, 1.60, 1.52 (s, s, s, s, s, s, 36H); 1.05, 1.04 (t,t, 12H). FAB MS (NBA) *m/z* 894 (M^+). IR (KBr) 2964, 1749, 1733 cm^{-1}.

A mixture of 2,7,10,13- tetra-*tert*-butyl-1,8-bis(2-carboxyethyl)acenaphtho[1,2-*j*]fluoranthene, 2,7,10,13-tetra-*tert*-butyl-1,9-bis[(2-carboxyethyl)acenaphtho[1,2-*j*]fluoranthene, and 2,7,10,13-tetra-*tert*-butyl-9,14-bis(2-carboxyethyl)acenaphtho [1,2-*j*]fluoranthene (3.8). A suspension of **3.7** (137 mg) in ethanol (14 ml) and 10% aqueous potassium hydroxide solution (7 ml) was refluxed for 3 h. The reaction mixture was cooled and concentrated *in vacuo*. A suspension of obtained yellow solid in 4 N hydrochloric acid (20 ml) was heated with refluxing for 8 h. The resulting yellow precipitate was filtered and washed with water to give crude **3.8** (96.3 mg, 91%). m.p. >300°C. FAB MS *m/z* 694 (M^+). IR (KBr) 3441, 2961, 1709 cm^{-1}.

A mixture of 4,9,13,16-tetra-*tert*-butyl-1,2,3,10,11,12-hexahydro-1,10-dioxo-*as*-indaceno[1,2,3-*cd*:6,7,8-*c'd'*]diphenalene, 4,9,13,16- tetra-*tert*-butyl-1,2,3,10,11,12-hexahydro-1,13-dioxo-*as*-indaceno[1,2,3-*cd*:6,7,8-*c'd'*]diphenalene, and 4,9,13,16-

tetra-*tert*-butyl-1,2,3,10,11,12-hexahydro-3,10-dioxo-*as*-indaceno[1,2,3-*cd*:6,7,8-*c'd'*]diphenalene (3.9). A mixture of compound **3.8** (81.4 mg, 117 μmol) and oxalyl chloride (5 ml) was heated with refluxing for 2 h. The reaction mixture was cooled and concentrated *in vacuo*. The resulting orange solid was dissolved in CH_2Cl_2 (9 ml) and cooled to -78 °C. Anhydrous $AlCl_3$ (100 mg, 750 μmol) was added to the solution and the reaction mixture was allowed to warm to -50 °C over 2 h, and stirred at -50 °C for 2 h. 2 N hydrochloric acid was added to the mixture and the organic layer was separated. The aqueous layer was extracted with small portions of CH_2Cl_2. The combined organic layers were washed with brine and dried over Na_2SO_4 and filtered. After column chromatography on silica gel (CH_2Cl_2), pure **3.9** (61.5 mg, 80%) was obtained as an orange powder. ^{1}H NMR (270 MHz, $CDCl_3$) δ 8.87, 8.82, 8.74, 8.69 (s, s, s, s, 2H); 8.26, 8.25, 8.15, 8.13 (s, s, s, s, 2H); 8.02, 7.99, 7.95, 7.93 (s, s, s, s, 2H); 3.88 (t, 4H); 3.21, 3.20, 3.16 (t, t, t, 2H); 1.74, 1.73, 1.72, 1.71, 1.66, 1.63 (s, s, s, s, s, s, 36H). FAB MS (NBA) *m/z* 659 (M^++H). IR (KBr) 2965, 1697 cm^{-1}.

A mixture of 4,9,13,16-tetra-*tert*-butyl-1,2,3,10,11,12-hexahydro-1,10-dihydroxy-*as*-indaceno[1,2,3-*cd*:6,7,8-*c'd'*]diphenalene, 4,9,13,16-tetra-*tert*-butyl-1,2,3,10,11,12-hexahydro-1,13-dihydroxy-*as*-indaceno[1,2,3-*cd*:6,7,8-*c'd'*]diphenalene, and 4,9,13,16-tetra-*tert*-butyl-1,2,3,10,11,12-hexahydro-3,10-dihydroxy-*as*-indaceno[1,2,3-*cd*:6,7,8-*c'd'*]diphenalene.

A mixture of **3.9** (78.8 mg, 120 μmol) and lithium aluminim hydride (10 mg, 263 μmol) in THF (16 ml) was stirred for 2 h. Dichloromethane was added and washed with brine. The organic layer was separated and the aqueous layer was extracted repeatedly with small portions of CH_2Cl_2. The combined organic layers were dried over Na_2SO_4 and filtered. After column chromatography on silica gel [CH_2Cl_2 / ether (1:10, v/v)], pure diols (77 mg, 97 %) were obtained as a yellow powder. ^{1}H NMR (270 MHz, $CDCl_3$) δ 8.71 (s, 2H); 8.12, 8.11, 8.106 (s, s, s, 2H); 7.92, 7.91, 7.90, 7.89 (s, s, s, s, 2H); 5.88 (m, 2H); 3.62 (m, 4H); 2.56 (m, 2H); 2.16 (m, 2H); 1.80, 1.798, 1.75, 1.70, 1.695, 1.65 (s, s, s, s, s, s, 36H). FAB MS *m/z* 662 (M^+). IR (KBr) 3425, 2956 cm^{-1}.

A mixture of 4,9,13,16- tetra-*tert*-butyl-1,10-dihydro-*as*-indaceno[1,2,3-*cd*:6,7,8-*c'd'*]diphenalene, 4,9,13,16- tetra-*tert*-butyl-1,13-dihydro-*as*-indaceno[1,2,3-*cd*:6,7,8-*c'd'*]diphenalene, and 4,9,13,16- tetra-*tert*-butyl-3,13-dihydro-*as*-indaceno[1,2,3-*cd*:6,7,8-*c'd'*]diphenalene (3.10).

Diols (15.9 mg, 24 μmol) in benzene (3 ml) was heated with refluxing. *p*-Toluene sulfonic acid monohydrate (1 mg, 5.2 μmol) was added to the solution, and the reaction mixture was stirred for 5 min. The mixture was cooled on ice-bath and concentrated *in vacuo*. The crude product was purified by column chromatography on silica gel

[benzene/hexane (1:4, v/v)] to give **3.10** (12.2 mg, 81%). ^{1}H NMR (270 MHz, $CDCl_3$) δ 8.81, 8.76 (s, s, 2H); 8.21, 8.16 (s, s, 2H); 8.03 (s, 2H); 7.61, 7.58 (dt, dt, *J*=10.23, 1.97 Hz, 2H); 6.43, 6.48 (dt, dt, *J*=10.23, 4.62 Hz, 2H); 4.21 (m, *J*=1.97, 4.29Hz, 2H); 1.76, 1.75, 1.67, 1.65 (s, s, s, s, 36H). FD MS *m/z* 626 (M^+)

Deutrated derivatives of 3.10. A solution of **3.9** (102 mg, 155 μmol) in CF_3COOD (2mL) + CH_2Cl_2 (1mL) was heated at 50 °C for 18 h. After cooling, the mixture was extracted with benzene, the benzene solution was washed with saturated aqueous $NaHCO_3$ and brine, dried over $MgSO_4$ and filtered. Purification with column chromatography on silica gel (benzene) gave deuterated **3.9** (98 mg, 95%). The same procedures as non-deuterated compounds affroded deuterated **3.10** (%D > 98%).

4,9,13,16- tetra-*tert*-butyl-*as*-indaceno[1,2,3-*cd*:6,7,8-*c'd'*]diphenalene (3.2).
A mixture of **9** (7 mg, 11.2 μmol) and *p*-chloranil (3 mg, 12.2 μmol) in benzene (2 ml) was refluxed for 10 min. The mixture was cooled on ice-bath and concentrated *in vacuo*. The crude product was purified by column chromatography on silica gel [benzene/hexane (1:2, v/v)] to give **3.2.**

Dication (3.2^{2+}). The hydrocarbon **3.2** (ca. 10 mg, 16 μmol) was added to 0.5 ml of concentrated D_2SO_4 to give the dication species. A reddish purple color appeared immediately. The dication was also obtained by the reaction of **2.3** with excess $SbCl_5$ in CH_2Cl_2.

Radical cation ($3.2^{(\bullet)(+)}$). The radical cation was generated by the reaction of **3.2** (ca. 3 mg, 4.8 μmol) with an equimoler amount of $SbCl_5$ (0.01 M, 0.5 ml, 5 μmol) in 10 ml of CH_2Cl_2. A solution turned green immediately.

Radical anion ($3.2^{(\bullet)(-)}$). The radical anion was generated under vacuum (*ca.* 10^{-4} torr) in sealed the cell B (Figure 2.8.1) by the reaction of **3.2** with a potassium mirror in DME.

Dianion (3.2^{2-}). The reaction of dihydro compounds **3.10** (10 mg, 16 μmol) with a potassium mirror in THF-d_8 (0.5 ml) in a sealed degassed tube afforded the dianion species. The dianion was also obtained by the reaction of **3.2** with a potassium mirror in THF in a sealed degassed tube.

NMR spectroscopy.

Dianion (3.2^{2-}). The procedure for the generation of 3.2^{2-} is similar to that of 2.3^{2-}. The contact of the THF-d_8 solution of **3.10** with a potassium mirror at - 78 °C for a week gave the orange solution, whose NMR spectra supported the generation of 3.2^{2-}.

ESR spectroscopy.

Neutral (3.2). The cell A (Figure 2.8.2) was used for the ESR measurement of **3.2**. *p*-Chloranil (1 mg, 4 μmol) was introduced into the ESR tube ***a*** and 1 mL of the benzene solution of **3.2** (10^{-3} M) was added by a syringe. The cell was connected to a vacuum line at ***b*** and the solvent was degassed by a repeated freeze-pump-thaw method (5 times). The cell was sealed at ***c*** and heated at 60 °C for 5 min. The ESR spectra of **3.2** were recorded at 20 °C.

Radical cations and radical anions ($3.2^{(\bullet)(+)}$ and $3.2^{(\bullet)(-)}$). The procedures for the generation of $3.2^{(\bullet)(+)}$ and $3.2^{(\bullet)(-)}$ (1.4×10^{-4} M) are similar to those of $2.3^{(\bullet)(+)}$ and $2.3^{(\bullet)(-)}$, respectively.

UV/Vis/NIR specroscopy.

Dication (3.2^{2+}). The qualitative electronic spectrum of 3.2^{2+} was obtained by the dissolution of **3.2** in D_2SO_4 at room temperature.

Radical cation ($3.2^{(\bullet)(+)}$). The qualitative measurement was carried out in the CH_2Cl_2 solution of $3.2^{(\bullet)(+)}$ at room temperature.

Neutral (3.2). The compound **3.2** was purified by column chromatography (silicagel). The pure **3.2** was dissolved in cyclohexane and the qualitative measurement was carried out at room temperature.

Dianion (3.2^{2-}) and radical anion ($3.2^{(\bullet)(-)}$). The procedures for the generation of 3.2^{2-} and $3.2^{(\bullet)(-)}$ are similar to those of 2.3^{2-} and $2.3^{(\bullet)(-)}$. The contact of the solution with a K-mirror at ***d*** at room temperature exhibited the gradual decrease of absorption of **3.2** and the new absorptions attributable to $3.2^{(\bullet)(-)}$ appeared. Further contact with a potassium mirror caused the gradual decrease of the absorption of $3.2^{(\bullet)(-)}$ with gradual increase of the absorption of 3.2^{2-}.

3.9 References

1) D. B. Clapp, *J. Am. Chem. Soc.* **1939**, *61*, 2733.

2) S. K. Pollack, B. V. Raine, W. J. Hehre, *J. Am. Chem. Soc.* **1981**, *103*, 6308.

3) F. London, *J. Phys. Radium.* **1937**, *8*, 397; R. McWeeny, *Mol. Phys.* **1958**, *1*, 311; R. B. Mallion, *Mol. Phys.* **1973**, *25*, 1415; J. Aihara, *Bull. Chem. Soc. Jpn*, **1985**, *58*, 1045.

4) C. A. Coulson, R. B. Mallion, *J. Am. Chem. Soc.* **1976**, *98*, 592.

– Chapter 4 –

Synthesis and Properties of Tribenzodecacyclenyl Species (TBzD)

4.1 Introduction

In Chapter 2 and 3, the properties of IDPL and *as*-IDPL containing two phenalenyl units were discussed. To study properties of higher amphoteric hydrocarbons, I designed tribenzodecacyclenyl (TBzD, **4.1**) containing three phenalenyl units. The compound **4.1** is expected to behave as a six-stage amphoteric redox compound (Figure 4.1). To my knowledge, limited examples have been studied exhibiting six-stage amphoteric redox properties. [1]

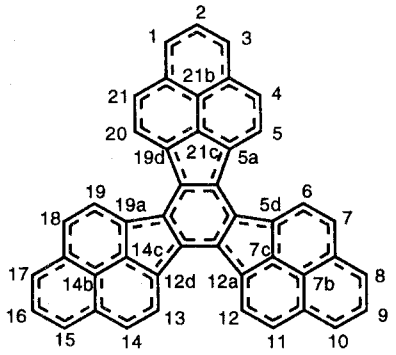

α^1: 1,3,8,10,15,17
α^2: 4,7,11,14,18,21
α^3: 5a,5d,12a,12d,19a,19d
β^1: 2,9,16
β^2: 5,6,12,13,19,20

Figure 4.1. Tribenzodecacyclenyl (TBzD)

While neutral IDPL and *as*-IDPL have relatively stable closed-shell structures, neutral TBzD **4.1** is a monoradical species (open-shell structure). However, neutral **4.1** is expected to be stable, because the unpaired electron will delocalize on the whole of the molecule having three phenalenyl units, which can potentially enjoy thermodynamically stable phenalenyl radical structure. Furthermore, **4.1** is expected to exhibit small E^{sum} values and to generate both trication and trianion species easily. Simple HMO calculations of TBzD **4.1** support these ideas (Figure 4.2).

The molecular orbitals ψ_{22}, ψ_{23}, and ψ_{24} correspond to the frontier orbitals of TBzD **4.1**. Large LCAO coefficients are found at the α-positions of phenalenyl units in the frontier orbitals. The distribution pattern of the coefficients is similar to that of phenalenyl species. This finding suggests that the phenalenyl units should contribute to the stability of the seven redox states of TBzD **4.1**.

The MO ψ_{23} and ψ_{24} are degenerate in energy. The presence of the degenerated MO in the frontier orbital constitutes a feature of TBzD **4.1**. As shown in Figure 4.2,

two unpaired electrons occupy ψ_{23} and/or ψ_{24} in the monoanion state. The monoanion state provides an interesting issue, whether this species will be singlet or triplet.

The orbital energies are $\alpha + 0.1130\ \beta$ (ψ_{22}) and $\alpha + 0.1492\ \beta$ (ψ_{23} and ψ_{24}). The small energy gap between ψ_{22} and ψ_{24} suggests **4.1** shows high amphotericity and has small E^{sum} values.

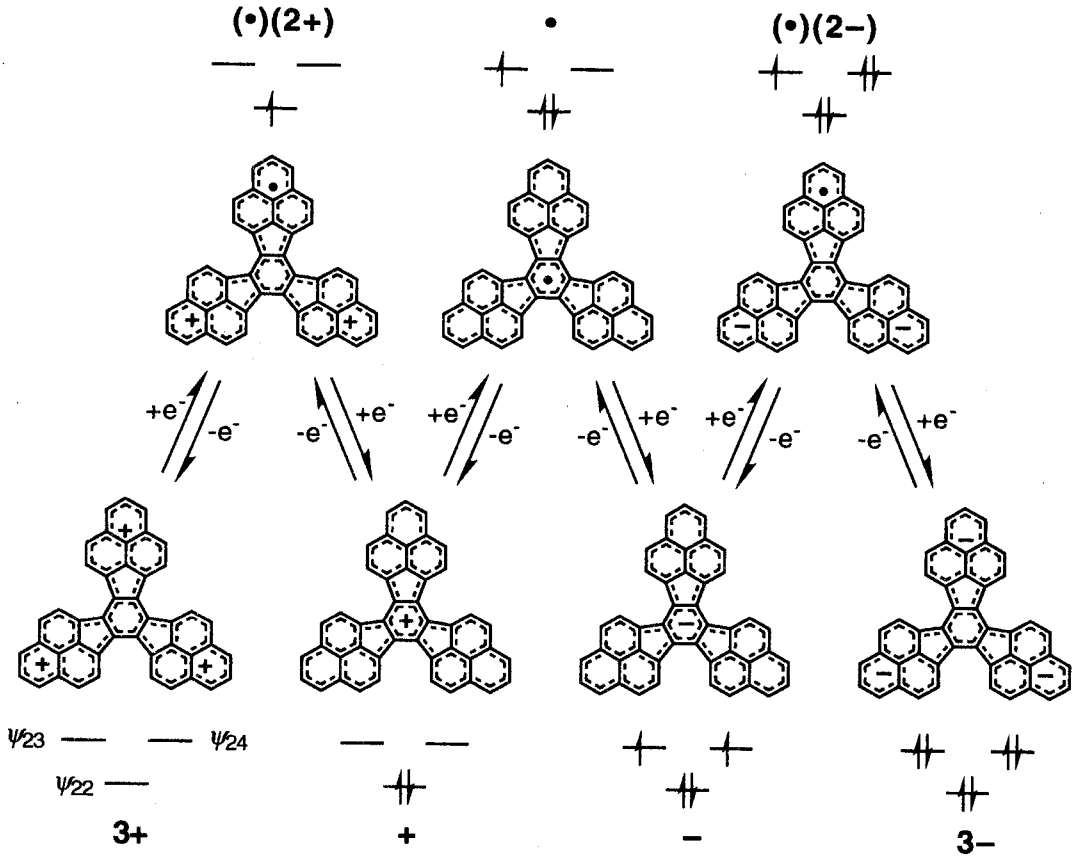

Figure 4.2. Six-stage amphoteric redox behavior of TBzD **4.1**

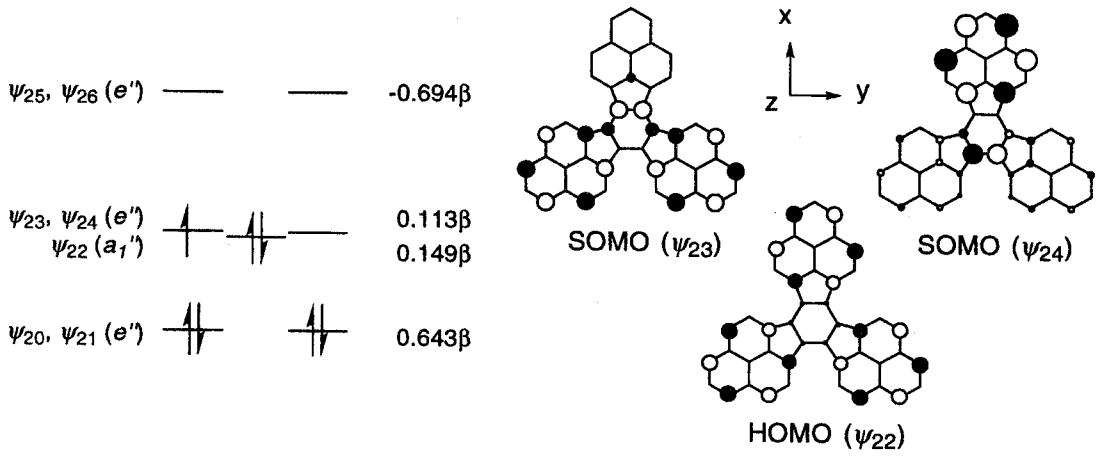

Figure 4.3. Selected molecular orbitals of **4.1**• calculated by the HMO method.

4.2 Synthesis of Tribenzodecacylenyl

An attempt to isolate the parent TBzD **4.1** failed due to the low solubility and the instability. In order to increase the solubility, simple alkyl substituents were introduced at the β-positions of phenalenyl units of **4.1**. Because the carbons at β-positions bear small LCAO coefficients in the frontier orbital, the parent compound will be only slightly perturbed by the alkyl substitution. The synthetic procedure is shown in Scheme 4.1.

Scheme 4.1. Synthetic procedure of **4.1** and **4.2**.

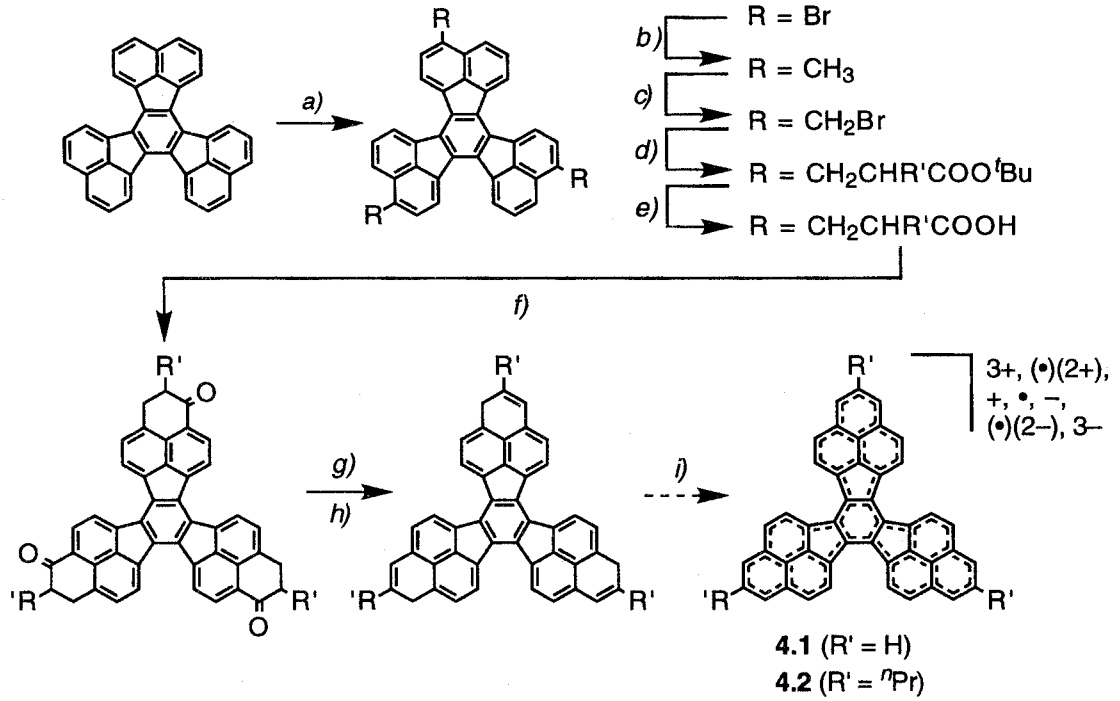

Reaction conditions : *a)* Br_2, I_2, PhCl, 3 d, rt, 63%. *b)* ^{n}BuLi, ^{t}BuLi, CH_3I, DME, -78°C to rt, 54%. *c)* NBS, benzoyl peroxide, benzene, reflux, 6 h, 70%. *d)* LDA, $CH_2R'COO^tBu$, -78°C, 6 h, 36%. *e)* PTSA, benzene, 86%. *f)* 1) $(COCl)_2$, 2) $AlCl_3$, CH_2Cl_2, -78 to -40°C, 2 h, 98%. *g)* $NaBH_4$, CH_2Cl_2 + ethanol, reflux, 1 d, 95%. *h)* cat. *p*-toluenesulfonic acid, benzene, reflux, 5 min, 9%. *i)* *p*-chloranil, benzene, reflux

Although **4.2** with three *n*-propyl groups increased solubility, **4.2** was found to be air-sensitive. The instability of **4.2** prevented the further investigation of the properties as a six-stage amphoteric redox compound. The failure to detect the unsubstituted and β-substituted TBzD species forced us to introduce substituents at the α-positions of phenalenyl units.

As the target of our efforts, we chose the symmetrical 4,7,11,14,18,21-hexa-*tert*-butyltribenzodecacyclenyl (HTB-TBzD) **4.3**. It seemed reasonable to build up this

compound from commercially available decacyclene following Scheme 4.2, previously developed in the synthesis of **4.1**, **4.2**, and phenalene.

Scheme 4.2. Synthesis of **4.3**$^{\bullet}$, **4.3**$^{3+}$, and **4.3**$^{3-}$.

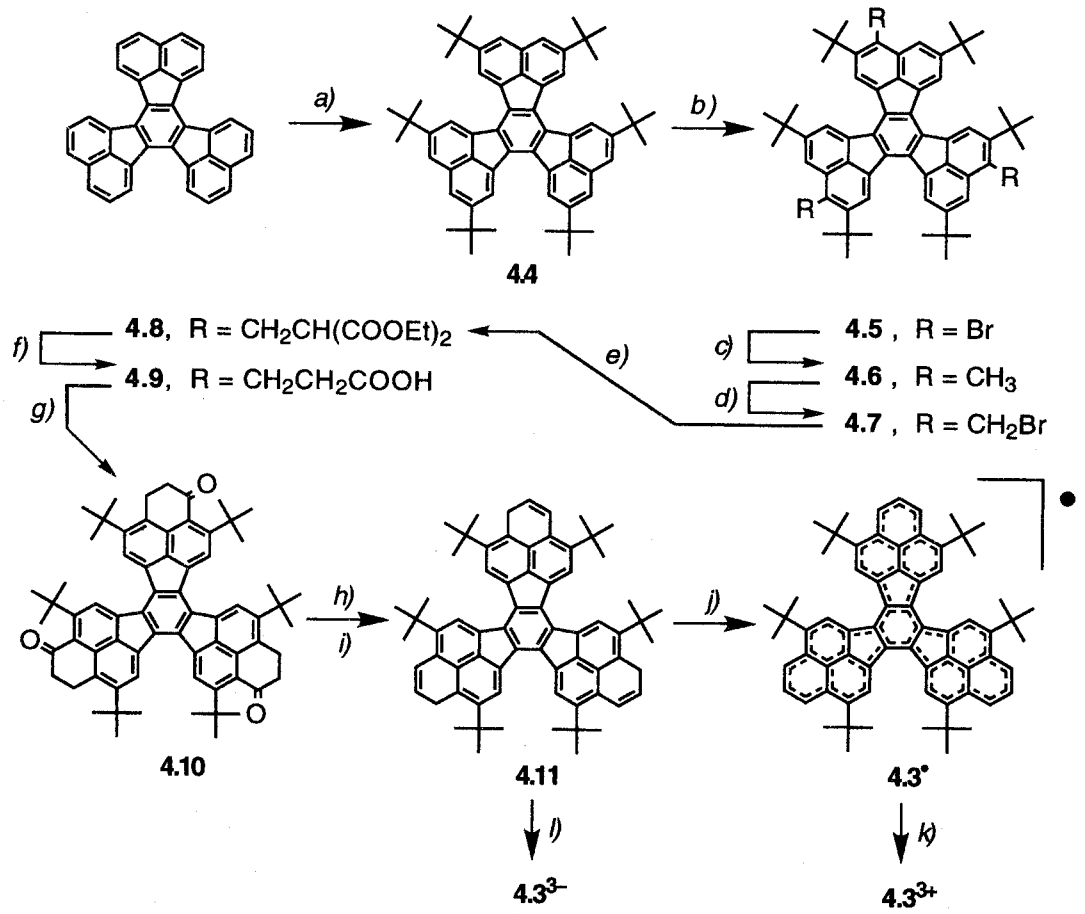

Reaction conditions : *a)* *t*BuCl, $AlCl_3$, CH_2Cl_2, rt, 2 h, 74% . *b)* Br_2, CH_2Cl_2, 2 h, rt, 76%. *c)* *n*BuLi, CH_3I, THF, -78°C to rt, 81%. *d)* NBS, benzoyl peroxide, benzene, reflux, 10 min, 96%. *e)* NaOEt, $CH_2(CO_2Et)_2$, benzene + ethanol, rt, 1 d, 36%. *f)* 1) aqueous KOH, EtOH, 2) 4 N HCl, 3) 100°C, 95%. *g)* 1) $(COCl)_2$, 2) $AlCl_3$, CH_2Cl_2, -50°C, 4 h, 99%. *h)* LAH, THF, rt, 2 h, 77%. *i)* cat. *p*-toluenesulfonic acid, benzene, reflux, 5 min, 90%. *j)* *p*-benzoquinone or *p*-chloranil, benzene, reflux, 10 min. *k)* conc. D_2SO_4 or 3eq. $(p\text{-}BrC_6H_4)_3N\ SbCl_6$ *l)* K-mirror, under vacuum, THF-d_8, -78°C, 1 week.

Firstly, six *tert*-butyl groups were introduced at the β-position of naphthalene units of decacyclene. It is well-known that the Friedel–Crafts alkylation of *tert*-butyl groups does not occur at sterically hindered positions. For example, the reaction of acenaphthene with *tert*-butyl chloride in the presence of a catalytic amount of $AlCl_3$ gives the 4,7-di-*tert*-butyl derivative in high yield. [2] In contrast, the reaction of decacyclene with *tert*-butyl chloride in the presence of *a catalytic amount* of $AlCl_3$ gave complicated mixtures, presumably mono, di, tri, tetra, penta, and hexa substituted

compounds. However, *tert*-butylation of decacyclene with *equimolar* $AlCl_3$ and a large excess of *tert*-butyl chloride afforded successfully 2,5,8,11,14,17-hexa-*tert*-butyldecacyclene **4.4** as yellow needles in 74%. Unambiguous structural proof for **4.4** was obtained by an X-ray analysis of an yellow needle grown by slow evaporating a solution of dichloromethane and *n*-hexane. Subsequent bromination in dichloromethane at room temperatue afforded tribromide **4.5** in 76% as an isomeric mixture. Two regioisomeric tribromides could not be separated by column chromatography or recrystallization. However, difficult separation of these compounds did not disturb our plan, because they were converted to a single symmetrical product in the final steps, **4.12** to **4.3**$^{\bullet}$, and **4.12** to **4.3**$^{3-}$. The lithiation of **4.5** with *n*-BuLi and subsequent methylation with MeI in THF afforded trimethyl compounds **4.6** in 81% yield. When DME was used instead of THF, considerable amounts of mono- and di-methyl derivatives were formed. Benzylic bromination of **4.6** was carried out with NBS and a catalytic amount of dibenzoyl peroxide. The resulting tris(bromomethyl) compounds **4.7** were used for the next reaction without purification due to the instability. The reaction of **4.7** with diethyl malonate afforded hexakis(ethoxycarbonyl) derivatives **4.8**, which were converted to tris(propionic acids) **4.9** by hydrolysis and subsequent decarboxylation. The Friedel–Crafts cyclization of the acid chlorides obtained by the reaction of **4.8** with oxalyl chloride afforded triketone compounds **4.10** in 99% yield. The cyclization reaction was done in dichloromethane at low temperature (- 50 – - 40°C), because aromatic compounds containing *tert*-butyl group tend to lose the *tert*-butyl group in the presence of Lewis acids at moderate temperature. The triketones **4.10** were reduced with lithium aluminum hydride to give triols. Reduction of **4.10** with $NaBH_4$ instead of lithium alminum hydride required long time (1 – 2 days) for completion. Dehydration of triols with a catalytic amount of *p*-toluenesulfonic acid afforded the compounds **4.11** with a low propensity to suffer air oxidation. The target neutral monoradical species **4.3** was obtained as an air-sensitive brown solid by the reaction of **4.11** with 1.5 equivalents of *p*-chloranil or *p*-benzoquinone.

Six redox states of TTB-TBzD, **4.3**$^{3+}$, **4.3**$^{(\bullet)(2+)}$, **4.3**$^{+}$, **4.3**$^{-}$, **4.3**$^{(\bullet)(2-)}$, and **4.3**$^{3-}$, were generated from the neutral species **4.3**. The trianion **4.3**$^{3-}$ were also obtained by the treatment of trihydro compounds **4.12** with potassium mirror.

4.3 Crystal structure of hexa-tert-butyldecacyclene

Hexa-*tert*-butyldecacyclene **4.4** was found to crystallize in space group P_{bcn} (#60) with eight molecules in the unit cell. As shown in Figure 4.3.1, **4.4** deviates from the D_{3h} symmetry and has torsion angles of 14.29, 14.34, and 7.56° between the central benzene unit and the naphthalene units. The inner protons (H^1, H^4, H^5, H^8, H^9, and

H^{12}) are in very close steric proximity to the other inner protons. The interatomic distance between the inner protons is 1.82 (H^1 – H^{12}), 2.01 (H^4 – H^5), and 1.84 (H^8 – H^9) Å, which are comparable to or smaller than the sum of van der Waals radii for the aromatic hydrogen atom (2.00 Å). These findings suggest that the steric hindrance of the inner protons causes deviation from the D_{3h} symmetry, the symmetrical feature of which is also borne out by a preliminary examination with a molecular model.

However, the simple ^1H NMR spectrum of **4.4** suggests the effective D_{3h} or C_3 symmetry in solution. The solution of **4.4** in CD_2Cl_2 at room temperature gave only three peaks at 1.55, 7.90, and 8.93 ppm, which exhibited no detectable changes of the line shapes even at -90°C. Figure 4.3.3 shows ^1H and ^{13}C NMR chemical shifts recorded in $CDCl_3$ at room temperature.

(a)

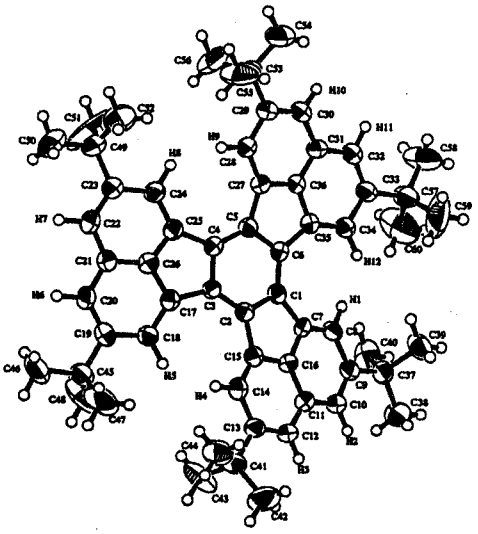

(b)

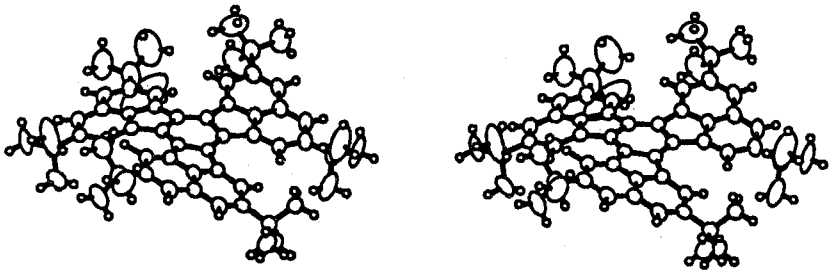

Figure 4.3.1. (a) The moleculer structure of **4.4** and (b) the stereoscopic view. Displacement ellipsoids are drawn at the 50% probability level.

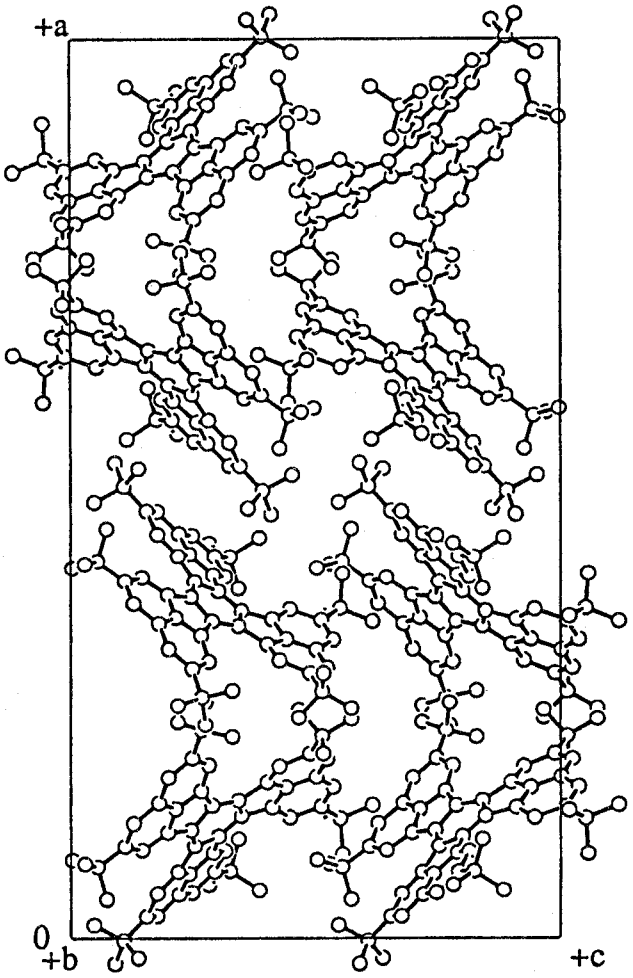

Figure 4.3.2. The crystal structure of **4.4** along the *c*-axis.

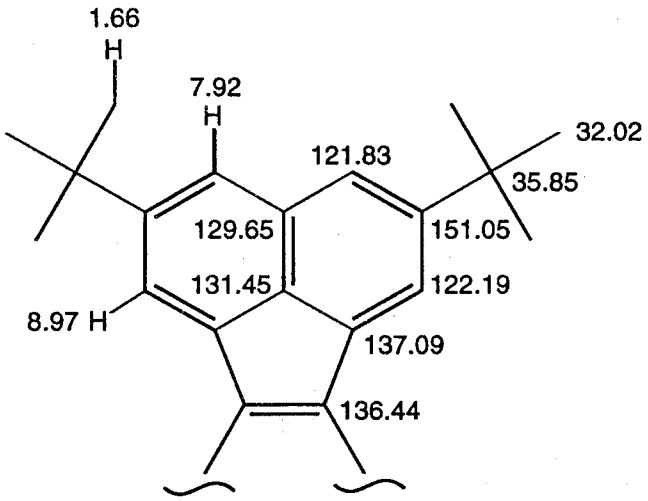

Figure 4.3.3. ^{1}H and ^{13}C NMR chemical shifts of **4.4** in $CDCl_3$ at room temperature

Table 4.3.1. Experimental X-ray data of **4.4.**

Crystal data

$C_{60}H_{66}$
$M_r = 787.18$
Orthorhombic
P_{bcn}
$a = 39.168(4)$ Å
$b = 11.793(3)$ Å
$c = 21.114(2)$ Å
$V = 9753(5)$ Å^3
$Z = 8$
$D_x = 1.072$ Mg m^{-3}

Cu$K\alpha$ radiation
$\lambda = 1.5418$ Å
Cell parameters from 25 reflections
$\theta = 24.8$–$43.5°$
$\mu = 0.446$ mm^{-1}
$T = 296$ K
Prismatic
0.40 x 0.20 x 0.80 mm
Yellow

Data collection

Rigaku AFC5R diffractometer
$\omega/2\theta$ scans
Absorption correction: refined from ΔF
8026 measured reflections
3590 observed reflections [$I > 3.00\sigma(I)$]

$2\theta_{max} = 120.1°$
$h = 0 \rightarrow 24$
$k = 0 \rightarrow 44$
$l = 0 \rightarrow 13$
3 standard reflections monitored
every 150 reflections
intensity decay: -1.12%

Refinement

Refinement on F
$R = 0.062$
$wR = 0.063$
$S = 1.88$
8026 reflections
589 parameters
$w = 1/\sigma^2(F_o)$

$(\Delta/\sigma)_{max} = 0.03$
$\Delta\rho_{max} = 0.22$ e Å^{-3}
$\Delta\rho_{min} = -0.27$ e Å^{-3}
Extinction correction: none
Atomic scattering factors from *International Tables for X-ray crystallograpy* (1974, Vol. IV)

Table 4.3.2. Fractional atomic coordinates and equivalent isotropic displacement parameters (Å^2).

$B_{eq} = (8\pi^2/3)(U_{11}(aa^*)^2+U_{22}(bb^*)^2+U_{33}(cc^*)^2+2U_{12}aa^*bb^*\cos\gamma+2U_{13}aa^*cc^*\cos\beta+2U_{23}bb^*cc^*\cos\alpha)$

	x	y	z	B_{eq}
C(1)	0.1040(1)	0.2354(4)	0.2526(2)	3.3(1)
C(2)	0.1148(1)	0.1580(4)	0.3009(2)	3.2(1)
C(3)	0.1370(1)	0.1930(4)	0.3478(2)	3.1(1)
C(4)	0.1536(1)	0.3015(4)	0.3417(2)	3.5(1)
C(5)	0.1482(1)	0.3674(4)	0.2881(2)	3.4(1)
C(6)	0.1214(1)	0.3380(4)	0.2451(2)	3.4(1)
C(7)	0.0748(1)	0.1815(4)	0.2187(2)	3.2(1)
C(8)	0.0501(1)	0.2159(5)	0.1767(2)	3.7(1)
C(9)	0.0245(1)	0.1389(4)	0.1549(2)	4.1(1)
C(10)	0.0248(1)	0.0289(5)	0.1762(2)	4.6(1)
C(11)	0.0492(1)	-0.0092(4)	0.2208(2)	4.1(1)
C(12)	0.0512(1)	-0.1182(4)	0.2475(3)	4.4(1)
C(13)	0.0751(1)	-0.1451(4)	0.2932(2)	3.9(1)
C(14)	0.0985(1)	-0.0584(4)	0.3145(2)	3.8(1)
C(15)	0.0965(1)	0.0487(4)	0.2905(2)	3.4(1)
C(16)	0.0726(1)	0.0706(4)	0.2420(2)	3.6(1)
C(17)	0.1460(1)	0.1468(4)	0.4109(2)	3.3(1)
C(18)	0.1351(1)	0.0565(4)	0.4474(2)	3.7(1)
C(19)	0.1470(1)	0.0449(4)	0.5115(2)	3.9(1)
C(20)	0.1684(1)	0.1240(5)	0.5366(2)	4.2(1)
C(21)	0.1793(1)	0.2188(4)	0.5017(2)	3.6(1)
C(22)	0.1988(1)	0.3103(5)	0.5240(3)	4.6(1)

C(23)	0.2047(1)	0.4045(5)	0.4883(3)	4.7(2)
C(24)	0.1908(1)	0.4118(4)	0.4260(2)	4.1(1)
C(25)	0.1735(1)	0.3219(4)	0.4009(2)	3.5(1)
C(26)	0.1679(1)	0.2265(4)	0.4397(2)	3.5(1)
C(27)	0.1638(1)	0.4743(4)	0.2657(2)	3.6(1)
C(28)	0.1922(1)	0.5387(4)	0.2813(2)	4.0(1)
C(29)	0.2000(1)	0.6394(4)	0.2478(3)	4.7(1)
C(30)	0.1785(2)	0.6740(5)	0.1993(3)	4.9(2)
C(31)	0.1508(1)	0.6072(4)	0.1796(2)	4.3(1)
C(32)	0.1287(2)	0.6310(5)	0.1281(3)	5.0(2)
C(33)	0.1035(1)	0.5567(5)	0.1107(2)	4.9(1)
C(34)	0.0992(1)	0.4524(5)	0.1454(2)	4.4(1)
C(35)	0.1190(1)	0.4303(4)	0.1979(2)	3.7(1)
C(36)	0.1444(1)	0.5094(4)	0.2137(2)	3.6(1)
C(37)	-0.0026(1)	0.1828(5)	0.1083(2)	4.6(1)
C(38)	-0.0281(1)	0.0924(5)	0.0906(3)	6.9(2)
C(39)	0.0149(1)	0.2226(5)	0.0475(3)	6.2(2)
C(40)	-0.0217(1)	0.2815(6)	0.1384(3)	6.9(2)
C(41)	0.0758(1)	-0.2623(4)	0.3243(3)	4.9(1)
C(42)	0.0601(2)	-0.3530(5)	0.2821(4)	8.7(2)
C(43)	0.0540(2)	-0.2545(5)	0.3849(3)	8.6(2)
C(44)	0.1117(2)	-0.2994(5)	0.3419(3)	7.0(2)
C(45)	0.1341(1)	-0.0558(5)	0.5504(3)	5.5(2)
C(46)	0.1485(2)	-0.0597(7)	0.6167(3)	9.5(2)
C(47)	0.1428(3)	-0.1653(6)	0.5174(4)	12.7(3)
C(48)	0.0951(2)	-0.0473(8)	0.5554(4)	13.2(3)
C(49)	0.2246(2)	0.5059(6)	0.5135(3)	7.6(2)
C(50)	0.2439(2)	0.4806(6)	0.5737(3)	9.8(3)
C(51)	0.2048(3)	0.6061(7)	0.5162(7)	20.9(5)
C(52)	0.2545(3)	0.526(1)	0.4656(4)	18.5(5)
C(53)	0.2313(2)	0.7103(5)	0.2673(3)	6.0(2)
C(54)	0.2406(2)	0.7994(6)	0.2184(3)	9.9(3)
C(55)	0.2627(2)	0.6347(6)	0.2746(4)	10.4(3)
C(56)	0.2238(2)	0.7690(7)	0.3295(4)	11.0(3)
C(57)	0.0805(2)	0.5805(5)	0.0544(3)	6.4(2)
C(58)	0.0839(2)	0.6964(7)	0.0287(4)	13.3(3)
C(59)	0.0884(3)	0.4963(9)	0.0028(4)	14.0(4)
C(60)	0.0438(2)	0.5649(8)	0.0731(4)	12.9(3)
H(1)	0.0508(9)	0.294(3)	0.162(2)	2.3(9)
H(2)	0.007(1)	-0.027(3)	0.162(2)	3(1)
H(3)	0.035(1)	-0.172(4)	0.233(2)	5(1)
H(4)	0.116(1)	-0.083(3)	0.346(2)	4(1)
H(5)	0.117(1)	0.000(3)	0.429(2)	3(1)
H(6)	0.176(1)	0.120(3)	0.580(2)	2.6(9)
H(7)	0.208(1)	0.305(3)	0.571(2)	3(1)
H(8)	0.194(1)	0.491(3)	0.401(2)	3(1)
H(9)	0.2060(8)	0.513(3)	0.318(2)	1.8(8)
H(10)	0.180(1)	0.744(4)	0.175(2)	6(1)
H(11)	0.138(1)	0.698(4)	0.105(2)	6(1)
H(12)	0.081(1)	0.397(4)	0.130(2)	5(1)

Table 4.3.3. Selected geometric parameters (Å, °)

C(1)—C(2)	1.433(6)	C(29)—C(30)	1.386(7)
C(1)—C(6)	1.398(6)	C(29)—C(53)	1.541(7)
C(1)—C(7)	1.491(6)	C(30)—C(31)	1.404(7)
C(2)—C(3)	1.380(6)	C(31)—C(32)	1.417(7)
C(2)—C(15)	1.490(6)	C(31)—C(36)	1.383(6)
C(3)—C(4)	1.441(6)	C(32)—C(33)	1.371(7)
C(3)—C(17)	1.483(6)	C(33)—C(34)	1.442(7)
C(4)—C(5)	1.388(6)	C(33)—C(57)	1.517(7)
C(4)—C(25)	1.492(6)	C(34)—C(35)	1.377(6)
C(5)—C(6)	1.432(6)	C(35)—C(36)	1.403(6)
C(5)—C(27)	1.480(6)	C(37)—C(38)	1.508(7)
C(6)—C(35)	1.478(6)	C(37)—C(39)	1.528(7)
C(7)—C(8)	1.372(6)	C(37)—C(40)	1.523(8)
C(7)—C(16)	1.401(6)	C(41)—C(42)	1.521(7)
C(8)—C(9)	1.431(6)	C(41)—C(43)	1.541(7)
C(9)—C(10)	1.374(7)	C(41)—C(44)	1.521(7)

C(9)—C(37)	1.534(7)	C(45)—C(46)	1.511(8)
C(10)—C(11)	1.414(6)	C(45)—C(47)	1.507(9)
C(11)—C(12)	1.407(7)	C(45)—C(48)	1.533(8)
C(11)—C(16)	1.388(6)	C(49)—C(50)	1.508(8)
C(12)—C(13)	1.382(7)	C(49)—C(51)	1.41(1)
C(13)—C(14)	1.442(6)	C(49)—C(52)	1.57(1)
C(13)—C(41)	1.531(6)	C(53)—C(54)	1.518(8)
C(14)—C(15)	1.364(6)	C(53)—C(55)	1.526(9)
C(15)—C(16)	1.412(6)	C(53)—C(56)	1.512(9)
C(17)—C(18)	1.382(6)	C(57)—C(58)	1.477(8)
C(17)—C(26)	1.409(6)	C(57)—C(59)	1.51(1)
C(18)—C(19)	1.438(6)	C(57)—C(60)	1.502(9)
C(19)—C(20)	1.361(7)	C(8)—H(1)	0.98(4)
C(19)—C(45)	1.531(7)	C(10)—H(2)	1.02(4)
C(20)—C(21)	1.406(7)	C(12)—H(3)	0.94(4)
C(21)—C(26)	1.388(6)	C(14)—H(4)	1.00(4)
C(22)—C(23)	1.362(7)	C(18)—H(5)	1.04(4)
C(23)—C(24)	1.426(6)	C(20)—H(6)	0.97(4)
C(23)—C(49)	1.525(7)	C(22)—H(7)	1.05(4)
C(24)—C(25)	1.366(6)	C(24)—H(8)	1.08(4)
C(25)—C(26)	1.409(6)	C(28)—H(9)	0.99(3)
C(27)—C(28)	1.385(6)	C(30)—H(10)	0.98(5)
C(27)—C(36)	1.399(6)	C(32)—H(11)	0.99(5)
C(28)—C(29)	1.416(7)	C(34)—H(12)	1.02(4)

C(2)—C(1)—C(6)	119.2(4)	C(10)—C(11)—C(12)	126.5(5)
C(2)—C(1)—C(7)	107.4(4)	C(10)—C(11)—C(16)	116.5(5)
C(6)—C(1)—C(7)	133.4(4)	C(12)—C(11)—C(16)	116.9(5)
C(1)—C(2)—C(3)	120.4(4)	C(11)—C(12)—C(13)	121.9(5)
C(1)—C(2)—C(15)	107.6(4)	C(12)—C(13)—C(14)	119.0(5)
C(3)—C(2)—C(15)	131.8(4)	C(12)—C(13)—C(41)	121.1(5)
C(2)—C(3)—C(4)	119.0(4)	C(14)—C(13)—C(41)	119.8(5)
C(2)—C(3)—C(17)	133.2(4)	C(13)—C(14)—C(15)	120.4(5)
C(4)—C(3)—C(17)	107.4(4)	C(2)—C(15)—C(14)	136.0(5)
C(3)—C(4)—C(5)	120.1(4)	C(2)—C(15)—C(16)	105.6(4)
C(3)—C(4)—C(25)	107.7(4)	C(14)—C(15)—C(16)	118.4(5)
C(5)—C(4)—C(25)	132.2(4)	C(7)—C(16)—C(11)	124.1(5)
C(4)—C(5)—C(6)	119.6(4)	C(7)—C(16)—C(15)	112.6(4)
C(4)—C(5)—C(27)	132.4(4)	C(11)—C(16)—C(15)	123.3(5)
C(6)—C(5)—C(27)	107.9(4)	C(3)—C(17)—C(18)	135.2(4)
C(1)—C(6)—C(5)	119.7(4)	C(3)—C(17)—C(26)	106.7(4)
C(1)—C(6)—C(35)	133.1(4)	C(18)—C(17)—C(26)	117.6(4)
C(5)—C(6)—C(35)	107.2(4)	C(17)—C(18)—C(19)	119.8(5)
C(1)—C(7)—C(8)	136.4(4)	C(18)—C(19)—C(20)	120.1(5)
C(1)—C(7)—C(16)	106.0(4)	C(18)—C(19)—C(45)	118.1(5)
C(8)—C(7)—C(16)	117.4(4)	C(20)—C(19)—C(45)	121.7(5)
C(7)—C(8)—C(9)	121.0(5)	C(19)—C(20)—C(21)	121.9(5)
C(8)—C(9)—C(10)	119.1(5)	C(20)—C(21)—C(22)	127.0(5)
C(8)—C(9)—C(37)	118.5(5)	C(20)—C(21)—C(26)	116.6(5)
C(10)—C(9)—C(37)	122.4(5)	C(22)—C(21)—C(26)	116.2(5)
C(9)—C(10)—C(11)	121.6(5)	C(21)—C(22)—C(23)	122.3(5)
C(22)—C(23)—C(24)	119.7(5)	C(6)—C(35)—C(34)	135.8(5)
C(22)—C(23)—C(49)	122.2(5)	C(6)—C(35)—C(36)	106.6(4)
C(24)—C(23)—C(49)	118.0(5)	C(34)—C(35)—C(36)	117.6(5)
C(23)—C(24)—C(25)	120.0(5)	C(27)—C(36)—C(31)	123.8(5)
C(4)—C(25)—C(24)	135.2(5)	C(27)—C(36)—C(35)	112.1(4)
C(4)—C(25)—C(26)	106.1(4)	C(31)—C(36)—C(35)	124.0(5)
C(24)—C(25)—C(26)	118.1(4)	C(9)—C(37)—C(38)	112.2(5)
C(17)—C(26)—C(21)	124.0(5)	C(9)—C(37)—C(39)	109.5(4)
C(17)—C(26)—C(25)	112.1(4)	C(9)—C(37)—C(40)	109.4(4)
C(21)—C(26)—C(25)	123.5(5)	C(38)—C(37)—C(39)	107.8(5)
C(5)—C(27)—C(28)	136.3(5)	C(38)—C(37)—C(40)	108.5(5)
C(5)—C(27)—C(36)	106.1(4)	C(39)—C(37)—C(40)	109.5(5)
C(28)—C(27)—C(36)	117.5(5)	C(13)—C(41)—C(42)	112.2(5)
C(27)—C(28)—C(29)	120.9(5)	C(13)—C(41)—C(43)	107.0(4)
C(28)—C(29)—C(30)	119.0(5)	C(13)—C(41)—C(44)	112.3(5)
C(28)—C(29)—C(53)	119.5(5)	C(42)—C(41)—C(43)	107.8(5)
C(30)—C(29)—C(53)	121.4(5)	C(42)—C(41)—C(44)	108.4(5)
C(29)—C(30)—C(31)	121.6(5)	C(43)—C(41)—C(44)	109.1(5)
C(30)—C(31)—C(32)	126.1(5)	C(19)—C(45)—C(46)	113.4(5)

C(30)—C(31)—C(36)	116.9(5)	C(19)—C(45)—C(47)	110.0(5)
C(32)—C(31)—C(36)	117.0(5)	C(19)—C(45)—C(48)	108.5(5)
C(31)—C(32)—C(33)	121.3(5)	C(46)—C(45)—C(47)	108.5(6)
C(32)—C(33)—C(34)	119.5(5)	C(46)—C(45)—C(48)	108.1(6)
C(32)—C(33)—C(57)	121.3(5)	C(47)—C(45)—C(48)	108.3(7)
C(34)—C(33)—C(57)	119.2(5)	C(23)—C(49)—C(50)	113.3(6)
C(33)—C(34)—C(35)	120.4(5)	C(23)—C(49)—C(51)	112.9(7)
C(23)—C(49)—C(52)	105.9(6)	C(54)—C(53)—C(56)	108.7(6)
C(50)—C(49)—C(51)	114.0(8)	C(55)—C(53)—C(56)	109.7(6)
C(50)—C(49)—C(52)	101.5(7)	C(33)—C(57)—C(59)	108.7(6)
C(51)—C(49)—C(52)	108.1(9)	C(33)—C(57)—C(60)	109.8(6)
C(29)—C(53)—C(54)	112.6(5)	C(58)—C(57)—C(59)	109.0(7)
C(29)—C(53)—C(55)	110.6(5)	C(58)—C(57)—C(60)	107.3(7)
C(29)—C(53)—C(56)	109.0(5)	C(59)—C(57)—C(60)	107.9(7)
C(54)—C(53)—C(55)	106.3(6)		

The data was corrected for Lorentz and polarization factors. The structure was solved by direct methods and refined by full-matrix least squares calculations with anisotropic displacement factors for C–atoms. The ring H atoms in the molecule were located experimentally and the positions of the *tert*-butyl H atoms were calculated from an idealized geometry with standard bond length and angles. Calculations were carried out using the SAPI91 programs.

4.4 Electrochemistry

The cyclic voltammogram of **4.3•** measured in CH_2Cl_2 exhibited six reversible one–electron redox waves as shown in Figure 4.4.1. This behavior provides evidence for the formation of the stable singly, doubly, and triply charged species. To our knowledge, only a few examples are known of compounds that exhibit six–stage amphoteric redox behavior. [1] The electrochemical data of **4.3•** are summarized in Table 4.4.1.

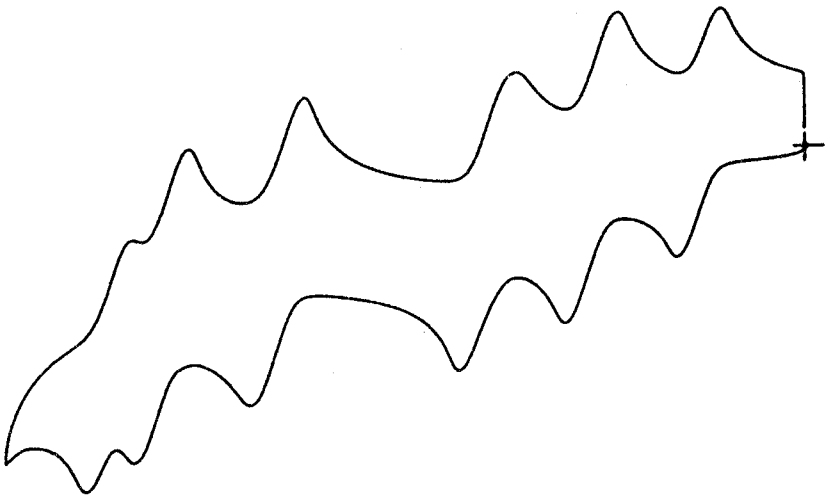

Figure 4.4.1. Cyclic voltammogram of **4.3•**

The sum of the redox potentials, E_1^{sum} of **4.3•** is substantially smaller than those reported so far for hydrocarbons. Such a small E_1^{sum} value can be explained in terms of the electronic stability of three redox states of the phenalenyl units owing to the delocalization of the generated charges or the unpaired electron over the molecule.

compound	E_3^{red}	E_2^{red}	E_1^{red}	E_1^{ox}	E_2^{ox}	E_3^{ox}	E_1^{sum}	E_2^{sum}	E_3^{sum}
4.3•	+0.87	+0.68	+0.27	-0.51	-0.89	-1.25	0.78	1.57	2.12

Table 4.4.1. Cyclic voltammetric data (V vs SCE) of **4.3•** in dichloromethane with 0.1 M $(^nBu)_4NClO_4$ as supporting electrolyte at room temperature; sweep rate = 100 mv/s.

4.5 NMR spectroscopy

4.5.1 Trication 4.3^{3+}

Many polycyclic benzenoid hydrocarbons are known to generate dication species in super acid, which serve as oxidizing agents to remove electrons from molecules. However, relatively small hydrocarbons tend to yield a mixture of radical cation and dication species, and to be protonated in the presence of a proton source. In contrast to the small aromatic hydrocarbons, large aromatic systems generally yield dication species in strong acid media easily. For example, the dication of hexacene is obtained in concentrated H_2SO_4.[3] However, limited examples gave trication species even in such a strong media.

Surprisingly, the trication species **4.3^{3+}** was found to be easily obtained as a dark green solution by dissolving **4.3•** in concentrated D_2SO_4 or as dark green needles by treating **4.3•** with three equivalents of tris(4-bromophenyl)aminium hexachloroantimonate, which is a weak one-electron oxdizing reagent. The trication was so stable as to remain unchanged even at 60°C. Figure 4.5.1 shows the aromatic region of the ^1H NMR spectrum of the dark green solution. The ^1H and ^{13}C NMR chemical shifts are given in Figure 4.5.2.

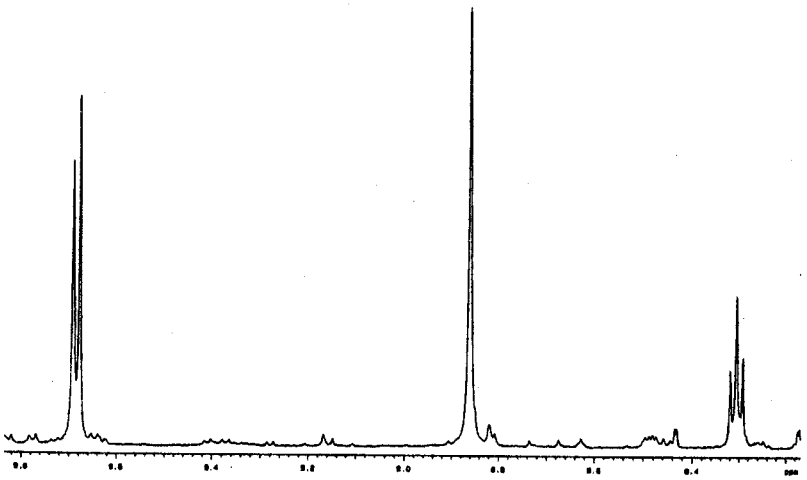

Figure 4.5.1. ^1H NMR spectrum of **4.3^{3+}** in D_2SO_4 at 60 °C.

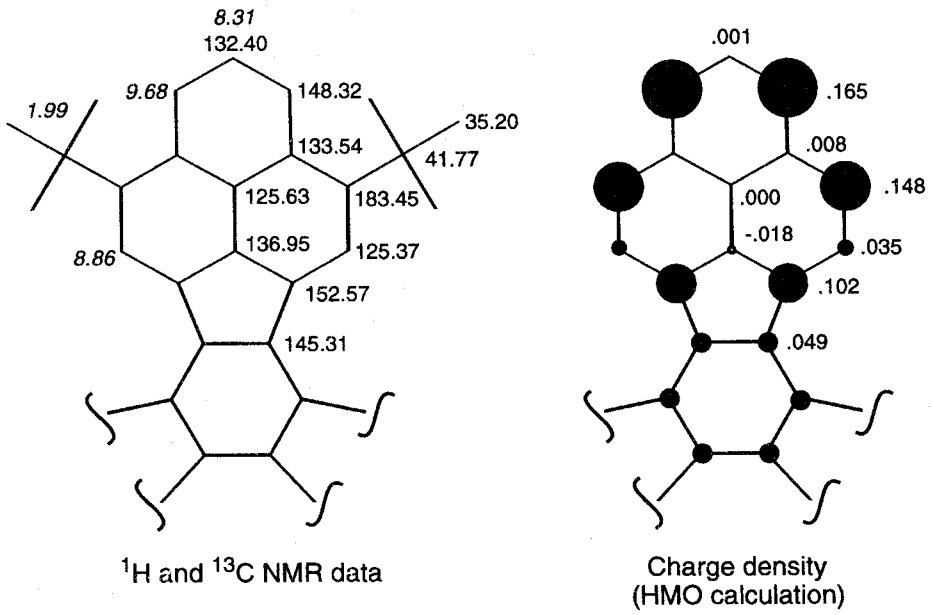

Figure 4.5.2. NMR data and charge density of **4.3**$^{3+}$

The simple ^{1}H and ^{13}C NMR spectra reflect the effective D_{3h} or C_3 structure of **4.3**$^{3+}$. The ^{13}C chemical shifts of **4.3**$^{3+}$ are found to be similar to those of **2.3**$^{2+}$ for equivalent carbon atoms. The HMO calculations indicate that 90% of three positive charges reside on three phenalenyl units. These findings suggest that the positive charge is delocalized mainly over three phenalenyl units (Figure 4.5.2).

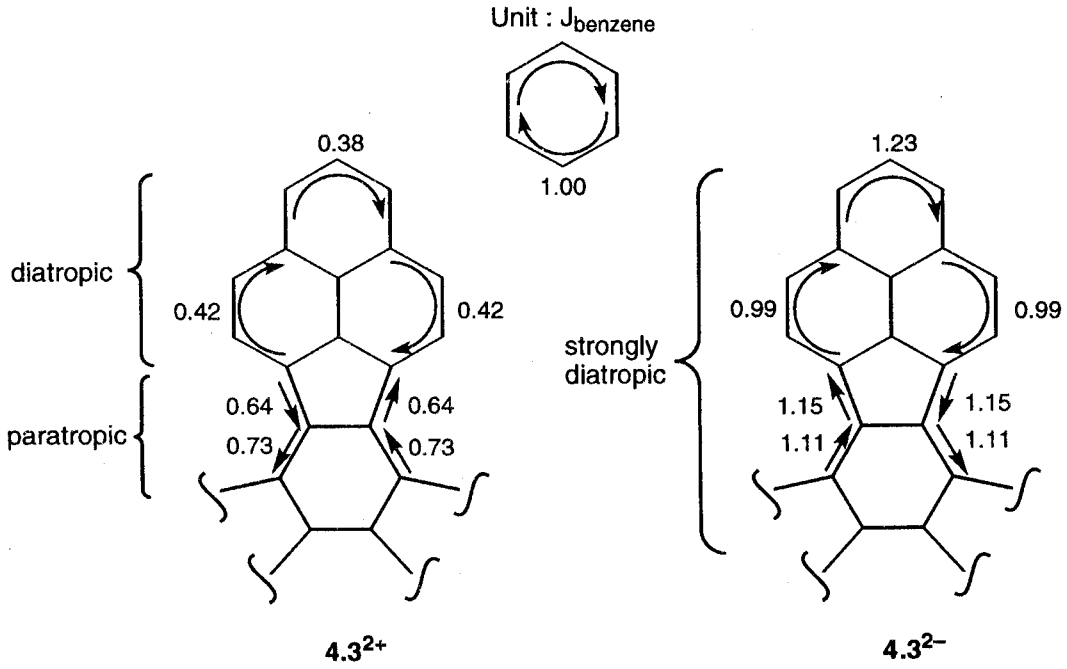

Figure 4.5.3. Ring current calculation of **4.3**$^{3+}$ and **4.3**$^{3-}$

In contrast to the similarity of ^{13}C chemical shifts, ring protons of **4.3**$^{3+}$ appear in considerably lower field region than those of **2.3**$^{2+}$ and **3.2**$^{2+}$. On the basis of the ring current calculations (Figure 4.5.3), the small contributions of paramagnetic ring current effects, which is consistent with the large HOMO(ψ_{20}, ψ_{21})–LUMO(ψ_{22}) gap of **4.3**$^{3+}$, may be responsible for the downfield shifts of **4.3**$^{3+}$.

4.5.2 Trianion 4.3^{3-}

The trianion **4.3**$^{3-}$ was generated as a red purple solution by the reaction of the compounds **4.11** with a potassium mirror in a sealed degassed tube at – 78 °C for a week. The trianion was found to be stable even at room temperature. Figure 4.5.4 shows the aromatic region of the ^{1}H NMR spectrum of the red purple solution. The ^{1}H and ^{13}C NMR chemical shifts are given in Figure 4.5.5.

Trianion also gave the simple ^{1}H and ^{13}C NMR spectra indicating the effective D_{3h} or C_3 structure of **4.3**$^{3-}$. The total ^{13}C chemical shift change of the sp^2 carbon atoms on going from **4.3**$^{3+}$ and **4.3**$^{3-}$ is 1041.63 ppm (or 173.61 ppm/e), which supports the idea of the existence of the trication and trianion, respectively. The shift changes on each carbons are large for the C atoms at α^1, α^2, and α^3, which correspond to the α-position of phenalenyl speceis, but small for the C atoms at other positions except for the central benzene ring. This finding suggests that three phenalenyl units contribute largely to the stability of both triply charged species.

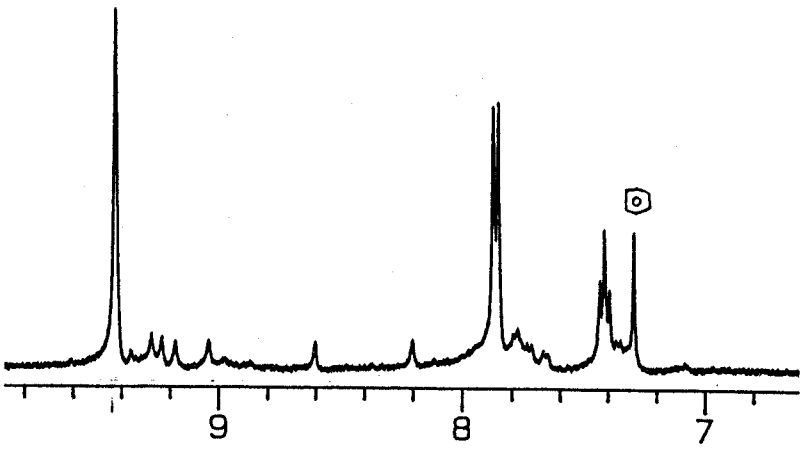

Figure 4.5.4. ^{1}H NMR spectrum of **4.3**$^{3-}$ in THF-d_8 at 30 °C.

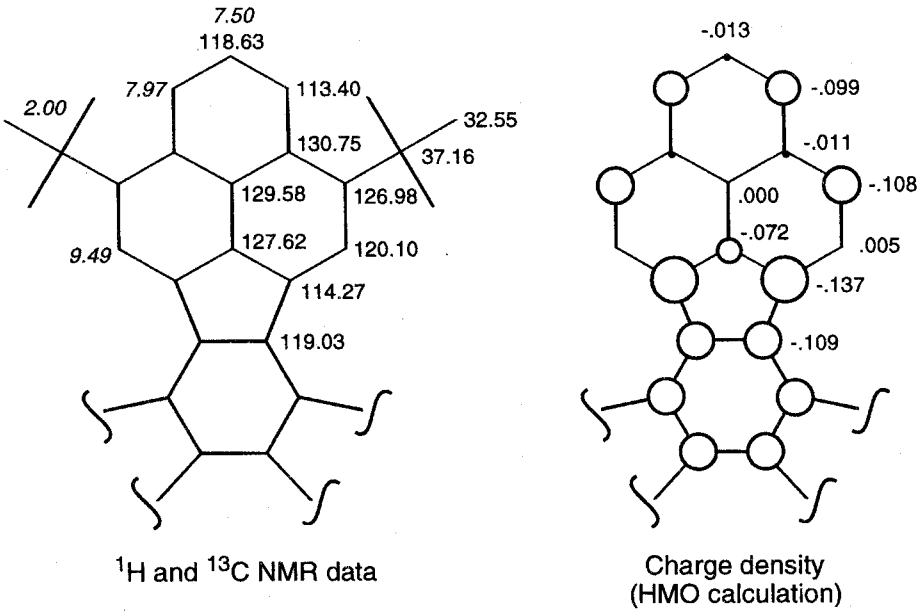

Figure 4.5.5. NMR data and charge density of $\mathbf{4.3}^{3-}$

Surprisingly, the trianion $\mathbf{4.3}^{3-}$ also exhibited the considerable downfield shifts of all ring protons as $\mathbf{2.3}^{2-}$ and $\mathbf{3.2}^{2-}$ in spite of the shielding effect caused by the three negative charges . In particular, the signals of the protons at β^2-position of $\mathbf{4.3}^{3-}$ unexpectedly appear at lower field than the signals of the corresponding protons of $\mathbf{4.3}^{3+}$. The ^{13}C chemical shifts of the C atoms at the posion β^2 reveal that the electron density at the position β^2 is slightly larger in $\mathbf{4.3}^{3-}$ than $\mathbf{4.3}^{3+}$. This finding cleary suggests the effect of a diamagnetic ring current in $\mathbf{4.3}^{3-}$. The ring current calculations indicate the pronounced diamagnetic ring currents along the periphery of the molecules (Figure 4.5.3). Thus the charge–induced upfield shift is compensated with the opposite influence of a diamagnetic ring current which is built up on trianion formation.

The stability of both triply charged species can be ascribed to large contribution of the type **4.3b** structure, which is supported by the HMO calculations indicating 90% of the total positive charges and 78% of the total negative charges on three phenalenyl units, respectively.

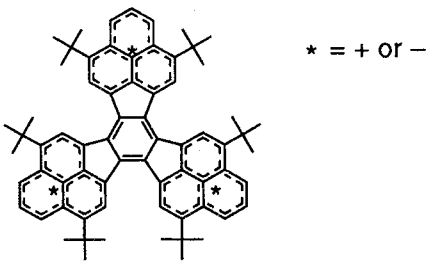

structure **4.3b**

4.5.3 Monocation 4.3+

Removal of one electron from the neutral radical **4.3•** should give the closed shell monocation **4.3+**. The treatment of **4.3•** with one electron oxidizing reagents, *e.g.* Ph_3CBF_4, Ph_3CSbCl_6, $(p\text{-}BrC_6H_5)_3NSbCl_6$, I_2, and $AlCl_3$, afforded dark green powder, which can be assigned to monocation species. However, the solution of the dark green powder in CD_2Cl_2 at room temperature gave no signals except for considerably broad peak at 1–2 ppm. The change of solvents (CD_2Cl_2 + CF_3COOD, CD_2Cl_2 + CD_3COOD, or acetone-d_6) and temperatures (30 °C – -80 °C) did not affect the shape of the peak. The broad peak is attributable to the equilibrium between the paramagnetic species and **4.3+**. The following three mechanisms seem plausible for the equilibrium: 1) disproportionation, $\mathbf{4.3^+ \rightleftharpoons 4.3^\bullet + 4.3^{(\bullet)(+)}}$; 2) electron transfer, $\mathbf{4.3^+ + 4.3^{(\bullet)(2+)} \rightleftharpoons 4.3^{(\bullet)(2+)} + 4.3^+}$; 3) electron transfer via other component **X**, $\mathbf{4.3^+ + X \rightleftharpoons 4.3^{(\bullet)(2+)} + X^{(\bullet)(+)}}$.

Some observations provide some insight. A trace of paramagnetic species were detected by ESR measurement of the solution of the dark green powder. The ESR spectrum was identical with that of $\mathbf{4.3^{(\bullet)(2+)}}$ and the signal intensity was independent of temperatures. These findings suggest that the disproportionation mechanism seems unlikely. Thus the electron transfer between **4.3+** and a trace of $\mathbf{4.3^{(\bullet)(2+)}}$ will be responsible for the broad signal. Elemental analysis for the dark green powder also support the presence of $\mathbf{4.3^{(\bullet)(2+)}}$.

Calc for $C_{69}H_{69}(SbCl_6)_n$: n = 1.0, C 66.41%, H 5.57%; n = 1.15, C 64.60%, H 5.42%. Found C 64.66%, H 5.27%.

Dissolution of the green powder in D_2SO_4 exhibited the simple pattern of ^1H NMR spectrum, which is identical with that of $\mathbf{4.3^{3+}}$.

At present, the pure **4.3+** could not be obtained unfortunately.

4.6 ESR spectroscopy

4.6.1 Neutral 4.3•

Although numerous studies on free radicals have been reported, those on stable hydrocarbon radicals have been limited. The representative examples are triphenylmethyl, [4] Kölsch's, [5] cyclopentadienyl, [6] and phenalenyl radical. [7] In particular, a simple alkyl derivative of the last example, tri-*tert*-butylphenlenyl radical, gave single crystals and the crystal structure was determined at room temperature recently. [8] These hydrocarbons should be stabilized kinetically by steric hindrance and thermodynamically by spin delocalization.

The neutral hydrocarbon **4.3**• is expected to be also stable because of the bulky *tert*-butyl groups and the highly delocalized structure. The dehydrogenation of the compounds **4.11** with *p*-benzoquinone or *p*-chloranil provided the neutral monoradical species as a brown solid. Contrary to the expectation, the neutral radical was found to decompose gradually on exposure to air.

The toluene solution of **4.3**• exhibited too ill–resolved ESR spectrum to determine the hyperfine coupling constants. However, the deuterated derivative **4,4** gave a ESR spectrum with hyperfine structure, from which two coupling constants were obtained, 1.43 G (6H), 0.47 (6H). The coupling constants at β^1 position were determined by a computer simulation. Figure 4.6.1 shows these ESR spectra along with the corresponding simulations. The experimental and theoretical hyperfine coupling constants are given in Figure 4.6.2.

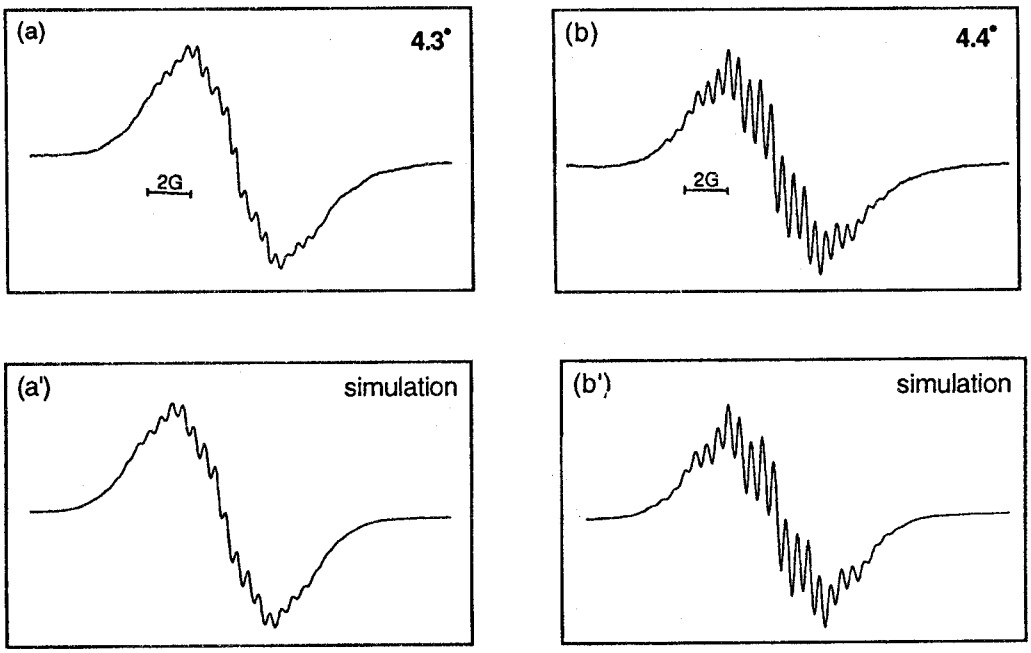

Figure 4.6.1. ESR spectra of (a) the neutral radical of **4.3**• and (b) the deuterated derivative **4.4**• and the corresponding simulated spectra (a') and (b'), respectively.

The liner relationship between the experimental and theoretical coupling constants suggests that the unpaired electron delocalization is not confined to one phenalenyl unit but is operative over the entire C_3 symmetric molecule. The highly delocalized structure is consistent with a single occupancy of the degenerated pair of e_g or nearly degenerate e_g like molecular orbitals.

The unusually broad ESR lines of **4.3**• are characteristic of radicals in a nearly degenerate ground state exhibiting a dynamic Jahn–Teller effect, as expected for a single or triple occupancy of e_g or almost degenerate e_g like molecular orbitals. Thus

the neutral radical **4.3**• retains an effective D_{3h} or C_3 symmetry on the hyperfine time scale and are subject to a dynamic Jahn–Teller effect. [9]

The deuterated compounds were synthesized following Scheme 4.6.1.

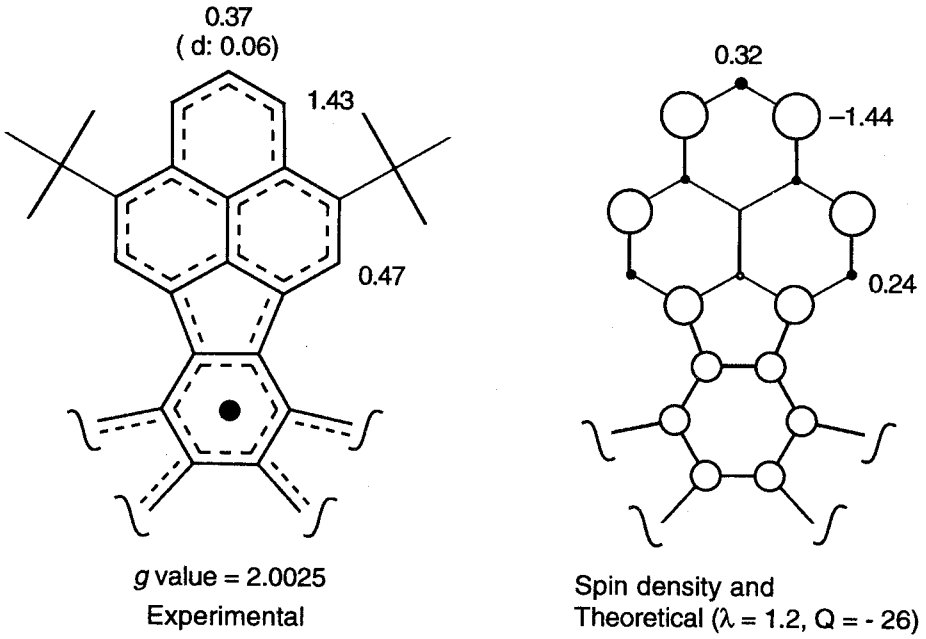

Figure 4.6.2. Experimental and theoretical hyperfine coupling constants (in G) along with spin density of **4.3**• and **4.4**•. In parentheses, a coupling constant of deuteron. Open-circle and closed-circle represent positive and negative spin density, respectively.

Scheme 4.6.1

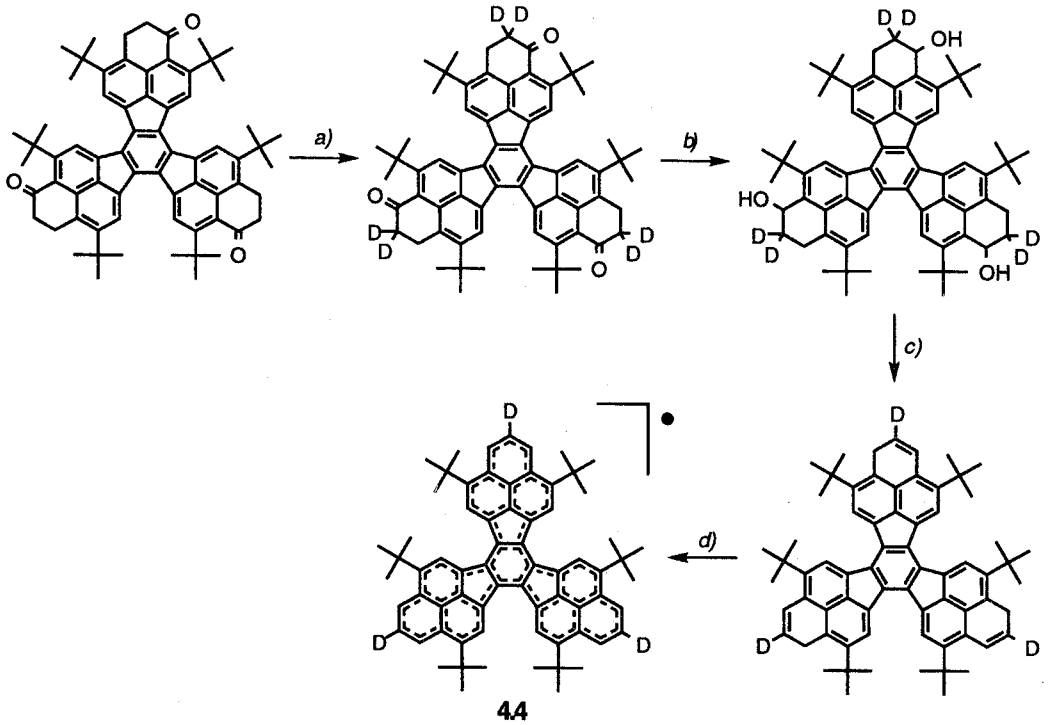

Reaction condition : *a)* CF_3COOD, CH_2Cl_2, 55°C, 12 h, 100%. *b)* $LiAlH_4$, THF, rt, 2 h, 75%. *c)* *p*-toluenesulfonic acid, benzene, reflux, 5 min. *d)* *p*-chloranil, benzene, 60°C, 15 min.

The near degeneracy of ψ_{22}, ψ_{23}, and ψ_{24} leads to the potential quartet state of neutral **4.3**. However, **4.3**• in a benzene matrix gave no quartet signals. This finding suggests no or a considerably small contribution of the structure **4.3c** to the ground state of **4.3**•.

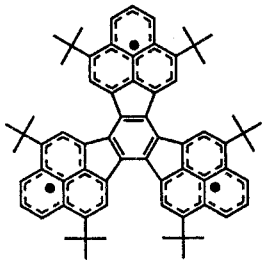

structure **4.3c**

4.6.2 Monoradical dication $4.3^{(\bullet)(2+)}$

Removal of two electrons from neutral **4.3**• should give the monoradical dication species $\mathbf{4.3}^{(\bullet)(2+)}$. On the basis of the HMO calculations, the SOMO corresponds to non-degenerate molecular orbital ψ_{22}.

The monoradical dication $\mathbf{4.3}^{(\bullet)(2+)}$ was obtained as dark green powder by the treatment of **4.3**• with two equivalent of $(p\text{-}BrC_6H_4)_3NSbCl_6$. Oxidation of **4.3**• with two equivalent of $SbCl_5$ also gave $\mathbf{4.3}^{(\bullet)(2+)}$ as a dark green solution. The solution of $\mathbf{4.3}^{(\bullet)(2+)}$ exhibited well–resolved ESR spectra as shown in Figure 4.6.3. Figure 4.6.4 shows the hyperfine coupling constants of $\mathbf{4.3}^{(\bullet)(2+)}$.

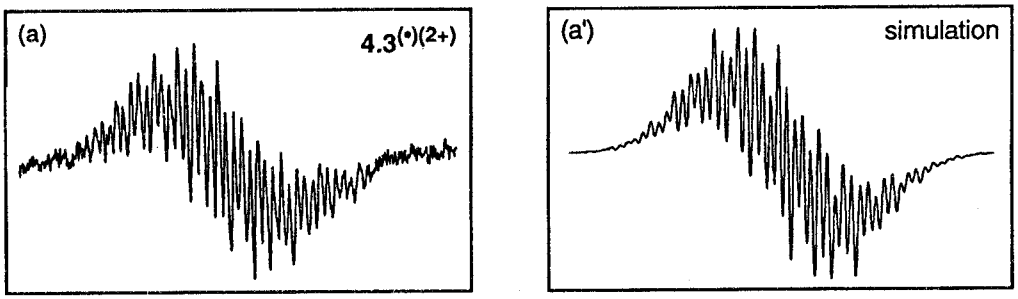

Figure 4.6.3. ESR spectra of (a) the neutral radical of $\mathbf{4.3}^{(\bullet)(2+)}$ and the corresponding simulated spectra (a').

The coupling constants of $\mathbf{4.3}^{(\bullet)(2+)}$ are larger than those of **4.3**•. This behavior is consistent with the HMO calculations indicating larger AO coefficients of ψ_{22} (SOMO for $\mathbf{4.3}^{(\bullet)(2+)}$) on the phenalenyl units compared to ψ_{23} and ψ_{24} (SOMO's for **4.3**•). On the basis of the HMO–McLachlan calculations, 98% of the π-spin population resides on the three phenalenyl units in $\mathbf{4.3}^{(\bullet)(2+)}$, while these units of **4.3**• account for 84% of the total spin population. These findings clearly suggest that the unpaired electron of

4.3$^{(\bullet)(2+)}$ should occupy the non–degenerate orbital ψ_{22}. The well–resolved ESR signal also reflects the non–degeneracy of SOMO of **4.3**$^{(\bullet)(2+)}$.

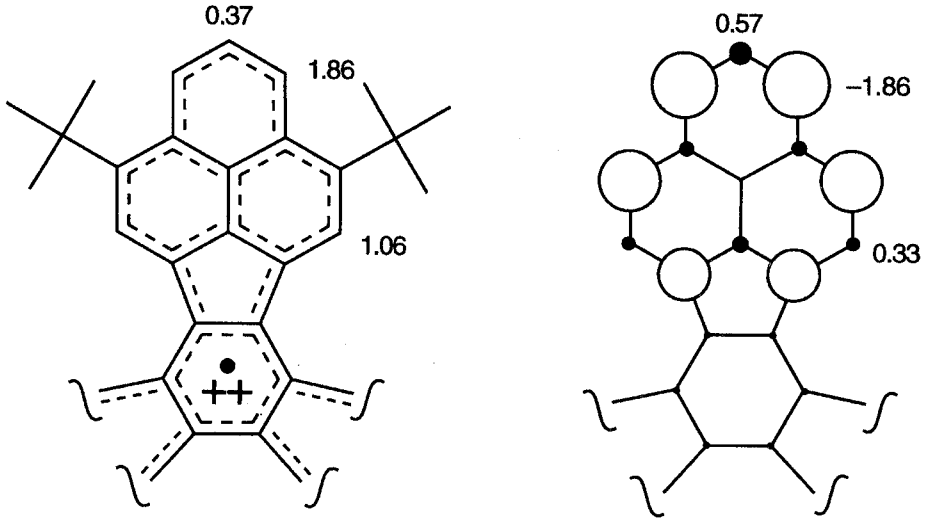

Figure 4.6.4. Experimental and theoretical hyperfine coupling constants (in G) along with spin density of **4.3**$^{(\bullet)(2+)}$. Open-circle and closed-circle represent positive and negative spin density, respectively.

4.6.3 Monoradical dianion 4.3$^{(\bullet)(2-)}$

The monoradical dianion **4.3**$^{(\bullet)(2-)}$ was generated by the rection of **4.3**$^{\bullet}$ with a potassium mirror in THF or DME. Further contact of the solution with a potassium mirror yielded trianion **4.3**$^{3-}$. The pair of the relevant frontier orbitals is degenerate or nearly degenerate with an occupancy number of three in **4.3**$^{(\bullet)(2-)}$.

The ESR spectra of **4.3**$^{(\bullet)(2-)}$ and **4.4**$^{(\bullet)(2-)}$ were given in Figure 4.6.5. A similar spectrum was observed on the oxidation of **4.3**$^{3-}$ with $(p\text{-}BrC_6H_4)_3NSbCl_5$. Simulation of the experimental ESR spectra indicates the following coupling: 3.30 G (2H), 1.07 G (2H), and 0.71 G (1H). The studies for deuterated derivative **4.4**$^{(\bullet)(2-)}$ indicated that the coupling constants of 0.71 G was due to one of the β^1 proton. The ESR studies for the monoradical dication species clearly suggest that the unpaired electron is "localized" mainly on one phenalenyl unit. The localized structure can be investigated by simply counting the number of equivalent protons giving rise to a particular coupling constants. The coupling constants were assigned as shown in Figure 4.6.6 but the assignment remains still questionable, because we could not calculate the spin density of **4.3**$^{(\bullet)(2-)}$ in such a localized structure by the use of the HMO–McLachlan method. The smaller coupling constants of **4.3**$^{(\bullet)(2-)}$ compared to phenalenyl radical suggest that the unpaired

electron resides on not only one phenalenyl unit but also the central benzene unit. Thus formula **4.3d** is the best description for monoradical dication species $\mathbf{4.3}^{(\bullet)(2-)}$.

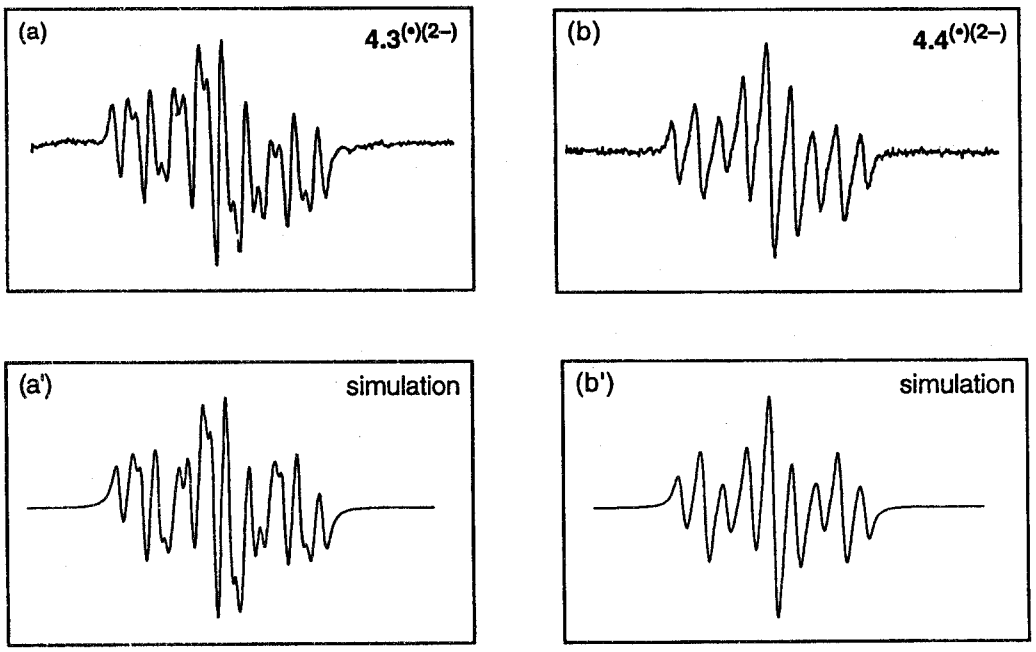

Figure 4.6.5. ESR spectra of (a) the neutral radical of $\mathbf{4.3}^{(\bullet)(2-)}$ and (b) the deuterated derivative $\mathbf{4.4}^{(\bullet)(2-)}$ and the corresponding simulated spectra (a') and (b'), respectively.

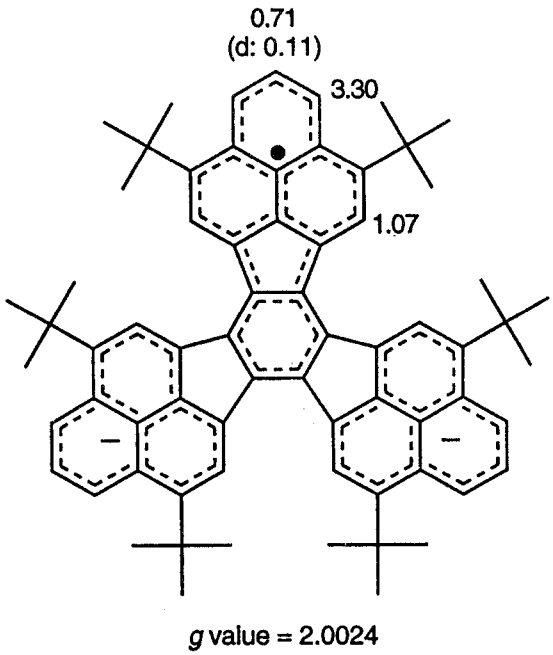

Figure 4.6.6. Experimental hyperfine coupling constants (in G) of $\mathbf{4.3}^{(\bullet)(2-)}$ and $\mathbf{4.4}^{(\bullet)(2-)}$. In parentheses, a coupling constant of deuteron.

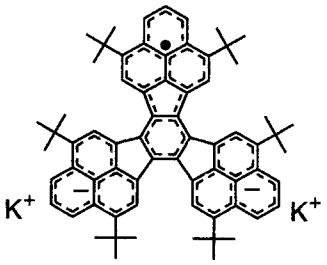

structure **4.3d**

As mentioned above, the unpaired electrons of $\mathbf{2.3}^{(\bullet)(-)}$ and $\mathbf{3.2}^{(\bullet)(-)}$ are delocalized over the entire molecule, while $\mathbf{4.3}^{(\bullet)(2-)}$ has a localized strucutre. [10] The followings are our way of finding the reason for some pieces of behavior observed.

In general, a compound with partially filled degenerate orbitals is unstable to vibrational modes to break down the high symmetry of the molecule in question, and is subject to Jahn–Teller distortion to a lower symmetry structure. For $\mathbf{4.3}^{(\bullet)(2-)}$, two counter cation K^+ will reside near two phenalenyl units and large polarizability in $\mathbf{4.3}^{(\bullet)(2-)}$ may allow the counter cation or solvent to localize two negative charges in two phenalenyl unit. Ion pairing is known to induce localization. In solvents such as THF, which favor the formation of contact ion piars, $\mathbf{4.3}^{(\bullet)(2-)}$ should possess a distorted structure with spin and negative charges–localization. However, even in such conditions as solvent-separated ion pair, *i.e.* DME at low temperature or 18-crown-6 in THF, ESR spectra consistent with localized structures were observed. In such conditions, the contribution of ion pairing to localization in $\mathbf{4.3}^{(\bullet)(2-)}$ should not be significant but may not be excluded. [11]

4.6.4 Monoanion 4.3⁻

The prime interest about $\mathbf{4.3}^-$ relates to whether this species will be singlet or triplet. The potential triplet state can be understood from the simple molecular orbital energy pattern derived from HMO calculations providing ideas that a degenerate pair of orbitals (ψ_{23} and ψ_{24}) is half occupied and the electrons can occupy separate orbitals with unpaired spins.

On exposure of a DME solution of $\mathbf{4.3}^{\bullet}$ to a potassium mirror, the intensity of the ESR signal of $\mathbf{4.3}^{\bullet}$ gradually decreased, and finally the signal became a small and broad peak. At this stage, we measured the ESR spectrum of the rigid solution of the reduced species at 77K and 173K, but no triplet signals were observed. Further reduction produced a new broad signal, which finally became a moderately–resolved ESR peak identical with those of $\mathbf{4.3}^{(\bullet)(2-)}$. More sophisticated calculations (PPP or PM3, Figure 4.6.7) converged in distorted C_2 structures and predict a singlet rather than a triplet

ground state. The ion pair of K^+ with one phenalenyl unit may cause the negative charge localization on one phenalenyl unit (structure **4.3e**).

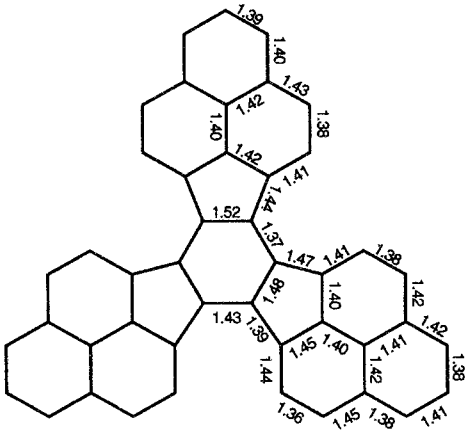

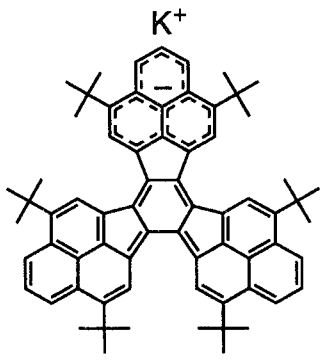

structure **4.3e**

Figure 4.6.7. The structure of $\mathbf{4.3}^-$ in a C_2 symmetry calculated by the PM3 method.

4.7 UV/Vis/NIR

4.7.1 General

In contrast to the five redox states of **2.3** and **3.2** exhibiting unequivocal electronic spectra, satisfactory and reliable spectra for $\mathbf{4.3}^{(\bullet)(+)}$, $\mathbf{4.3}^+$, $\mathbf{4.3}^-$, and $\mathbf{4.3}^{(\bullet)(-)}$ were not obtained, because these species would exist together with other redox states and give complicated spectra. In following sections, I will only discuss the electronic spectra for three redox states, $\mathbf{4.3}^\bullet$, $\mathbf{4.3}^{3+}$, and $\mathbf{4.3}^{3-}$.

*4.7.2 Neutral **4.3**$^\bullet$*

Figure 4.7.1 shows the electronic spectra of the three redox states of $\mathbf{4.3}^\bullet$, while Table 4.7.1 lists the wavelength of the band maxima.

Table 4.7.1. Maxima, λ_{max} (in nm) (ε, $cm^{-1}M^{-1}$), of electronic bands for $\mathbf{4.3}^{3+}$, $\mathbf{4.3}^\bullet$, and $\mathbf{4.3}^{3-}$.

$\mathbf{4.3}^{3+}$	$\mathbf{4.3}^\bullet$	$\mathbf{4.3}^{3-}$
231 (81800)	380	256 (39200)
494 (118000)	437	333 (34300)
550 (sh, 37900)	680	361 (37300)
601 (42500)	710	421 (21000)
676 (sh, 26700)	1130	507 (52300)
775 (sh, 7760)	1340	543 (56300)

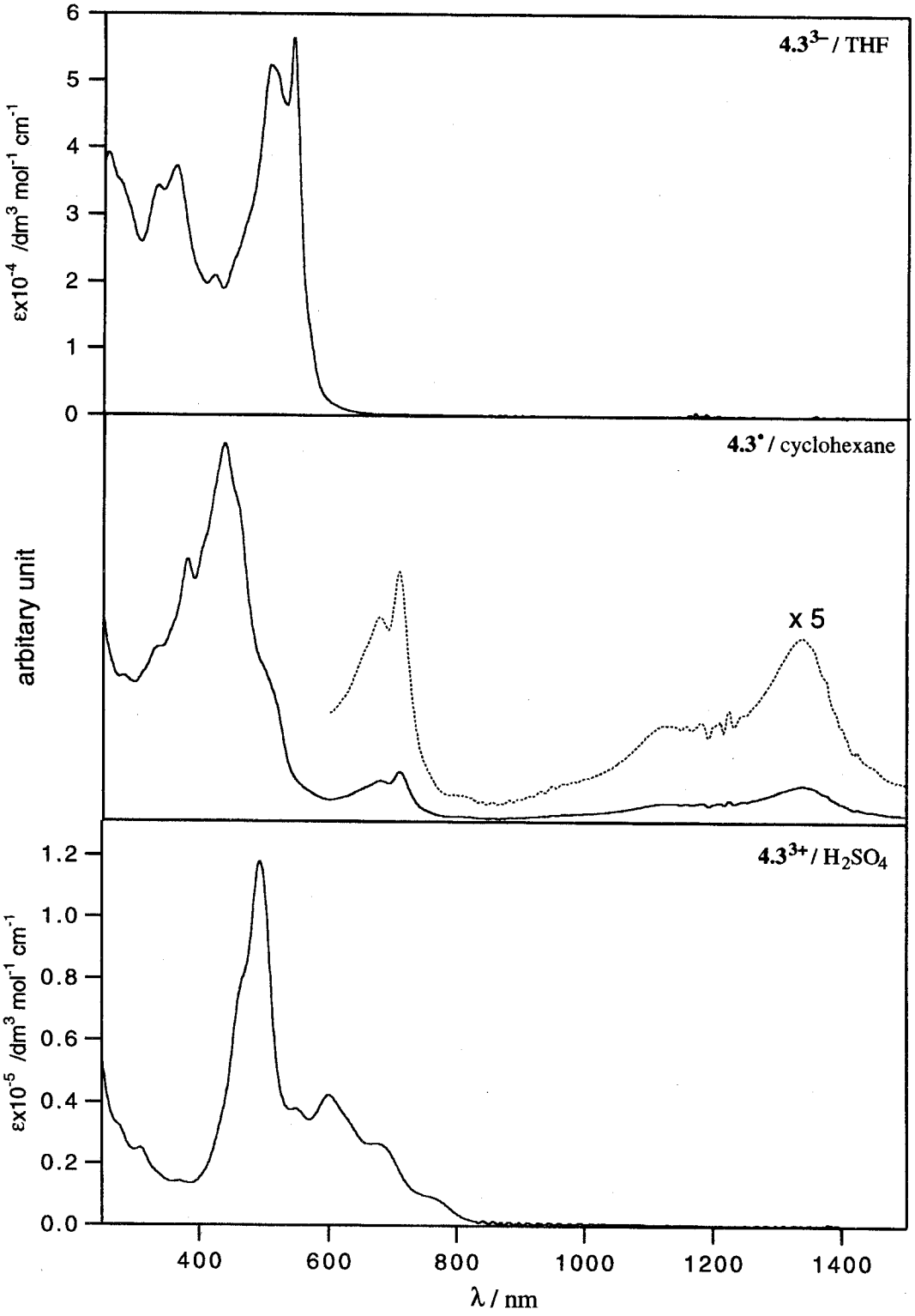

Figure 4.7.1. Electronic absorption spectra of the three redox states of **4.3**$^{\bullet}$.

Table 4.7.2 Selected electronic transition data for **4.3**$^{3+}$, **4.3**$^{\bullet}$, and **4.3**$^{3-}$ calculated by the INDO/S CI method and assignments of the observed electronic bands.

	theoretical				experimental
	symmetry label	ΔE, eV	oscillator strength	substantial contribution [a], %	λ, nm; ΔE,eV
4.3^{3+}		2.20	0.00	e"(ψ_{24}) ← e"(ψ_{20}), 28	*b*
				e"(ψ_{23}) ← e"(ψ_{21}), 28	
				a_1"(ψ_{22}) ← a_2"(ψ_{19}), 18	
		2.33	0.08	a_1"(ψ_{22}) ← e"(ψ_{21}), 40	*b*
				e"(ψ_{24}) ← e"(ψ_{20}), 14	
				e"(ψ_{23}) ← e"(ψ_{21}), 14	
		2.33	0.08	a_1"(ψ_{22}) ← e"(ψ_{20}), 40	*b*
				e"(ψ_{24}) ← e"(ψ_{21}), 14	
				e"(ψ_{23}) ← e"(ψ_{20}), 14	
4.3	B	1.17	0.00	b(ψ_{102})[c] ← a(ψ_{100}), 64	1340; 0.93
				b(ψ_{102}) ← a(ψ_{101}), 21	
	A	1.42	0.02	a(ψ_{101}) ← a(ψ_{100}), 64	710; 1.75
				a(ψ_{103}) ← a(ψ_{100}), 14	
				b(ψ_{102}) ← b(ψ_{99}), 10	
4.3^{3-}		2.53	0.00	e"(ψ_{26}) ← e"(ψ_{23}), 39	*d*
				e"(ψ_{25}) ← e"(ψ_{24}), 39	
		2.63	0.00	e"(ψ_{25}) ← e"(ψ_{23}), 42	*d*
				e"(ψ_{26}) ← e"(ψ_{24}), 42	
		2.67	1.41	e"(ψ_{25}) ← a_1"(ψ_{22}), 21	543; 2.28
				e"(ψ_{26}) ← e"(ψ_{23}), 15	
				e"(ψ_{25}) ← e"(ψ_{24}), 15	
				a_1"(ψ_{27}) ← e"(ψ_{23}), 13	
		2.67	1.41	e"(ψ_{26}) ← a_1"(ψ_{22}), 21	543; 2.28
				e"(ψ_{25}) ← e"(ψ_{23}), 15	
				e"(ψ_{26}) ← e"(ψ_{24}), 15	
				a_1"(ψ_{27}) ← e"(ψ_{24}), 13	

[a] In parentheses, the molecular orbitals calculated by the HMO method. See Figure 4.1.2. [b] Could not be assigned due to the weak and broad peaks. [c] The INDO/S calculations predicted the lower symmetry C_2 for **4.3**$^{\bullet}$. In parentheses, the molecular orbitals calculated by the INDO/S method. See also Figure 4.7.2. [d] Could not be observed due to the intense band at 543 nm.

In order to assign the electronic bands to transitions between orbitals, MO calculations by the INDO/S method were performed (Table 4.7.2). In each case, the ten highest occupied and ten lowest unoccupied orbitals was used for configuration interaction. Figure 4.7.2 presents schematically the calculated SCF levels of seven relevant highest occupied and lowest unoccupied orbitals for **4.3**•, **4.3**$^{3+}$, and **4.3**$^{3-}$.

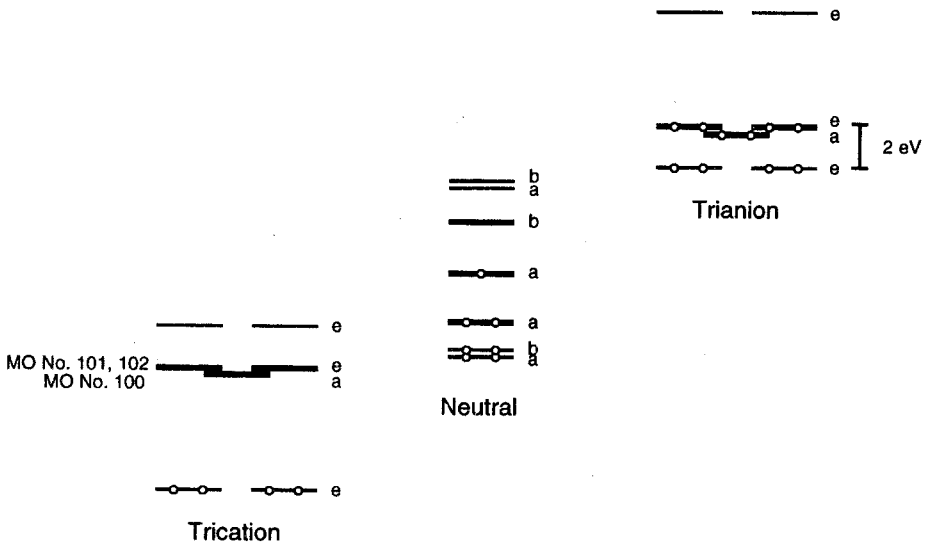

Figure 4.7.2. Energy levels of several occupied and unoccupied MOs in the five redox stages of TBzD **4.1**, as calculated by the MOPAC6/PM3 method. The optimized structures are in C_2 symmetry for neutral state and in C_3 symmetry for other states. The bold lines represent HOMO, SOMO, and LUMO of neutral state.

Dehydration of the orange derivatives **4.11** resulted in formation of a product showing the bathochromic shifts of electronic spectra. The many transitions in visible region are responsible for the dark brown color of the **4.3**•. In addition to the low–energy band at 710 nm, **4.3**• exhibited the weak and broad NIR transitions at 900 – 1500 nm. On the basis of the calculations, these low-energy bands should be due to the transition in which SOMO participates. However, it is not easy at present to assign these peaks exactly. The INDO/S and PM3 calculations predicted the deviated C_2 structure for **4.3**•, where the degenerate *e* pair split into the SOMO *a* and the LUMO *b*. The ESR spectrum of **4.3**• fits into the D_{3h} or C_3 symmetry, something that is not evident from the calculations. On electronic transition time scale, the deviated C_2 structure might give the bands observed, while the time–averaged C_2 structure on ESR time scale might exhibit the ESR signal indicating the unpaired electron delocalization over the entire C_3 molecule.

4.7.3 Trication 4.3^{3+} *and trianion* 4.3^{3-}

The absorption spectra of $\mathbf{4.3}^{3+}$ essentially consist of weak and broad bands at 600–800 nm and relatively intense band at 494 nm. The weak bands should be due to HOMO→LUMO and HOMO→NLUMO transitions. The INDO/S and PM3 calculations predict the C_3 symmetry for $\mathbf{4.3}^{3+}$ and HOMO (ψ_{20} and ψ_{21}) and LUMO (ψ_{23} and ψ_{24}) remains degenerate. The degeneracy of the orbitals may cause the participation of many transitions in a band.

A similar statement should hold for $\mathbf{4.3}^{3-}$. Unfortunately, the predicted first and second bands were not observed due to the intense band at 543 nm. The intense band at 543 nm consists of many transitions, in which NHOMO–LUMO and HOMO–NLUMO excitation participate in addition to the HOMO–LUMO transition. The absorption bands of $\mathbf{4.3}^{3-}$ terminate at the shortest wavelength region, which is consistent with a small paramagnetic ring current effect, *i.e.* a large diamagnetic effect in ^{1}H NMR spectrum as $\mathbf{2.3}^{2-}$ and $\mathbf{3.2}^{2-}$.

4.8 Conclusion

Expectedly, HTB-TBzD **4.3**$^{\bullet}$ containing three phenalenyl units was also found to exhibit high amphotericity and behave as a six-stage amphoteric redox compound. This means that one molecule has as many as seven electronic states. Surprisingly, **4.3**$^{\bullet}$ gave super-charged species, *i.e.* trication and trianion, with no difficulties. This high amphotericity primarily depends on the NBMO character of the frontier orbitals caused by three phenalenyl units. In contrast to **2.3** and **3.2**, the neutral state of **4.3** has an open-shell structure. Unfortunately, single crystal of the radical could not be obtained, but was stable enough to isolate and to study the properties. The highly delocalized structure and bulky *tert*-butyl groups should stabilize **4.3**$^{\bullet}$ thermodynamically and kinetically.

The basic π-electronic structure of redox states of **4.3**$^{\bullet}$ was essentially similar to those of **2.3** and **3.2**, while the most remarkable differences were found in $\mathbf{4.3}^{(\bullet)(2-)}$ and $\mathbf{4.3}^{-}$, which exhibited the charges and spin localization on one phenalenyl unit. These differences would be caused by Jahn–Teller effect. Thus the orbital degeneracy made differences in the properties of the ground state.

4.9 Experimental section

Material. Decacyclene (Aldrich) was recrystallized from xylenes two times.

2,5,8,11,14,17-Hexa-*tert*-butyldecacyclene (4.4). To a suspension of decacyclene (Aldrich; 5.64 g, 12.5 mmol) in CH_2Cl_2 (300 ml) were added *tert*-butyl chloride (28 ml) and anhydrous $AlCl_3$ (2.1 g, 15.7 mmol) at room temperature and stirred for 1 h. Additional *tert*-butyl chloride(10 ml) was added and the reaction mixture was stirred for 1 h. The mixture was poured into ice-water and the organic layer was separated. The aqueous layer was extracted repeatedly with small portions of CH_2Cl_2. The combined organic layers were dried over Na_2SO_4 and filtered, and the solvent was removed. Pure **4.4** (7.3 g, 74%) was obtained after column chromatography on silica gel [benzene/hexane (1:10, v/v)] and subsequent recrystallization (ethanol + CH_2Cl_2). m.p. >300°C. ^{1}H NMR (270 MHz, $CDCl_3$) δ 8.97 (d, *J*=1Hz, 6H), 7.92 (d, *J*=1Hz, 6H), 1.66 (s, 54H). ^{13}C NMR (67.8 MHz, $CDCl_3$) δ 151.05, 137.09, 136.44, 131.45, 129.65, 122.19, 121.83, 35.85 [$\underline{C}(CH_3)_3$], 32.02 [$C(\underline{C}H_3)_3$]. FD MS *m/z* : 786 (M^+). Anal. Calcd for $C_{60}H_{66}$: C, 91.55; H, 8.45. Found: C, 91.38; H, 8.43.

A mixture of 2,5,8,11,14,17-hexa-*tert*-butyl-1,6,12-tribromodecacyclene and 2,5,8,11,14,17-hexa-*tert*-butyl-1,6,13-tribromodecacyclene (4.5). Compound **4.4** (7.87 g, 10 mmol) was dissolved in CH_2Cl_2 (300 ml) and bromine (1.6 ml, 31.1 mmol) was added to the solution, and stirred for 6h at room temperature. 10% Aqueous sodium thiosulfate solution was added to the reaction mixture to reduce the excess bromine. The organic layer was separated and the aqueous layer was extracted with CH_2Cl_2. The combined organic layer were dried over Na_2SO_4 and filtered, and the solvent was removed. The crude product was purified by column chromatography on silica gel [benzene/hexane (1:10, v/v)] to give **4.5** (7.8 g, 76%). ^{1}H NMR (270 MHz, $CDCl_3$) δ 8.88-8.86 (3H), 8.78-8.74 (3H), 8.43-8.38 (3H), 1.88-1.63 (54H). FD MS *m/z* 1020 (M^+)

A mixture of 2,5,8,11,14,17-hexa-*tert*-butyl-1,6,12-trimethyldecacyclene and 2,5,8,11,14,17-hexa-*tert*-butyl-1,6,13-trimethyldecacyclene (4.6). *n*-Butyllitium(7.3 ml, 11.7 mmol, 1.6 M in hexane) was added to a solution of **4.5** (2.0 g, 1.95 mmol) in 150 ml of THF at -78 °C. After stirring for 15 min, methyl iodide (1.46ml, 23.4mmol) was added. The reaction mixture was allowed to warm to room temperature over night. Saturated aqueous ammonium chloride solution and 100 ml of benzene were added to the reaction mixture. The organic layer was separated and the aqueous layer was extracted repeatedly with small portions of benzene. The combined organic layers were dried over Na_2SO_4 and filtered. After evaporation of the solvent, purification by column chromatography on silica gel [benzene/hexane (1:4, v/v)] followed by recrystallization (CH_2Cl_2 + ethanol) gave pure **4.6** (1.31 g, 81%). ^{1}H NMR (270 MHz, $CDCl_3$) δ 8.89-8.87 (3H), 8.82-8.79 (3H), 8.13-8.12 (3H) 3.08-3.07 (9H), 1.76-1.62 (54H). FD MS *m/z* 828 (M^+).

A mixture of 2,5,8,11,14,17-hexa-*tert*-butyl-1,6,12-tris(bromomethyl)decacyclene and 2,5,8,11,14,17-hexa-*tert*-butyl-1,6,13-tris(bromomethyl)decacyclene (4.7). The mixture of compound **4.6** (829 mg, 1 mmol), *N*-bromosuccinimide (587 mg, 3.3 mmol), benzoylperoxid (80 mg, 0.33 mmol) in 100 ml of benzene was refluxed for 20 min. The reaction mixture was concentrated *in vacuo* and 3 ml of *n*-hexane was added. The resulting colorless precipitate was removed by filtration and the filtrate was concentrated *in vacuo* to give crude **4.7** (1.02 g, 95.5%). ^{1}H NMR (270 MHz, $CDCl_3$) 8.85-8.80 (3H), 8.75-8.69 (3H), 8.34-8.33 (3H), 5.54-5.52 (6H), 1.81-1.64 (54H).

A mixture of 2,5,8,11,14,17-hexa-*tert*-butyl-1,6,12-tris[2,2-bis(ethoxycarbonyl) ethyl]decacyclene and 2,5,8,11,14,17-hexa-*tert*-butyl-1,6,13-tris[2,2-bis (ethoxy-carbonyl)ethyl]decacyclene (4.8) . Diethyl malonate (0.91 ml, 6.03 mmol) was added to a sodium ethoxide solution freshly prepared from 15 ml of anhydrous ethanol and sodium (126 mg, 5.48 mmol). To the clear solution was added **4.7** (1.02 g, 0.955 mmol) dissolved in benzene (15 ml). After the stirring for 4 h, water was added to the reaction mixture. The organic layer was separated and the aqueous layer was extracted repeatedly with small amounts of benzene. The combined organic layers were dried over $MgSO_4$ and filtered. After evaporation of the solvent, the crude product was purified by column chromatography on silica gel (benzene) to give **4.8** (383 mg, 31%) . ^{1}H NMR (270 MHz, $CDCl_3$) 8.88 (s, 3H), 8.80 (s, 3H), 8.03-8.02 (3H), 4.28 (m, 6H), 4.22-3.92 (m, 12H), 3.91 (m, 3H), 1.74-1.61 (54H), 1.13-1.05 (18H). FD MS *m/z* 1303 (M^+).

A mixture of 2,5,8,11,14,17-hexa-*tert*-butyl-1,6,12-tris(2-carboxyethyl)decacyc-lene and 2,5,8,11,14,17-hexa-*tert*-butyl-1,6,13-tris(2-carboxyethyl)decacyclene (4.9). The suspension of **4.8** (383 mg) in ethanol (14 ml) and 10% aqueous potassium hydroxide solution (7 ml) was refluxed for 3 h. The reaction mixture was cooled and concentrated *in vacuo*. The obtained yellow solid in 4 N hydrochloric acid (20 ml) was heated with refluxing for 8 h. The resulting yellow precipitate was filtered and washed with water. Pure **4.9** (280 mg, 95%) was obtained after column chromatography on silica gel [benzene/acetone (3:1, v/v)]. FD MS *m/z* 1003 (M^++H). IR (KBr) 3600-2500, 2961, 1709 cm^{-1}.

A mixture of 4,7,11,14,18,21-hexa-*tert*-butyl-1,2,3,8,9,10,15,16,17-nona-hydro-1,8,15-trioxo-tribenzodecacyclene and 4,7,11,14,18,21-hexa-*tert*-butyl-1,2,3,8,9,10, 15,16,17-nona-hydro-1,8,17-trioxo-tribenzodecacyclene (4.10). A mixture of compound **4.9** (500 mg, 0.498 mmol) and oxalyl chloride (3 ml) was heated with refluxing for 1 h. The reaction mixture was cooled and concentrated *in vacuo*. The

resulting orange solid was dissolved in CH_2Cl_2 (70 ml) and cooled to -78 °C. Anhydrous $AlCl_3$ (750 mg, 5.62 mmol) was added to the solution and the reaction mixture was allowed to warm to -50 °C over 2 h, and stirred at -50 °C for 4 h. 2 N hydrochloric acid was added to the mixture and the organic layer was separated. The aqueous layer was extracted with small portions of CH_2Cl_2. The combined organic layers were washed with brine and dried over Na_2SO_4 and filtered. After column chromatography on silica gel (CH_2Cl_2), pure **4.10** (467 mg, 98.8%) was obtained as an orange powder. ^1H NMR (270 MHz, $CDCl_3$) δ 8.99-8.95 (3H), 8.85-8.80 (3H), 3.91 (t, 6H), 3.23 (t, 6H), 1.73-1.70 (54H). FD MS *m/z* 949 (M^++H). IR (KBr) 2965, 1699 cm^{-1}.

A mixture of 4,7,11,14,18,21-hexa-*tert*-butyl-1,2,3,8,9,10,15,16,17-nona-hydro-1,8,15-trihydroxy-tribenzodecacyclene and 4,7,11,14,18,21-hexa-*tert*-butyl-1,2,3,8,9,10,15,16,17-nona-hydro-1,8,17-trihydroxy-tribenzodecacyclene

A mixture of **4.10** (467 mg, 12.2 mmol) and sodium borohydride (460 mg, 12.2 mmol) in CH_2Cl_2 (20 ml) and ethanol (10 ml) was refluxed for 24 h. The mixture was cooled and 2 N hydrochloric acid was added dropwise. The organic layer was separated and the aqueous layer was extracted repeatedly with small portion of CH_2Cl_2. The combined organic layers were washed with brine and dried over Na_2SO_4, and filtered. After column chromatography on silica gel (CH_2Cl_2), pure triols (430 mg, 91.5%) was obtained as a yellow powder. ^1H NMR (270 MHz, $CDCl_3$) δ 8.78 (s, 6H), 5.90 (br, 3H), 3.71 (m, 3H), 3.48 (m, 3H), 2.59 (m, 3H), 2.17 (m, 3H), 1.76-1.71 (54H). FD MS *m/z* 955 (M^+), 937 (M^+- H_2O), 919 (M^+- $2H_2O$), 901 (M^+- $3H_2O$). IR (KBr) 3425, 2956 cm^{-1}.

A mixture of 4,7,11,14,18,21-hexa-*tert*-butyl-1,8,15-trihydro-tribenzodecacyclene and 4,7,11,14,18,21-hexa-*tert*-butyl-1,8,17-trihydro-tribenzodecacyclene (4.11). Triols (57 mg, 59.7 μmol) in benzene (15 ml) was heated with refluxing. *p*-Toluene sulfonic acid monohydrate (1 mg, 5.2 μmol) was added to the solution, and the reaction mixture was stirred for 5 min. The mixture was cooled on ice-bath and concentrated *in vacuo*. The crude product was purified by column chromatography on silica gel [benzene/hexane (1:4, v/v)] to give **4.11** (39.8 mg, 74%). ^1H NMR (270 MHz, $CDCl_3$) δ 8.95 (s, 3H), 8.88 (s, 3H), 7.66 (dt, *J*=10.56, 1.97 Hz, 3H), 6.61 (dt, *J*=10.56, 4.29 Hz, 3H), 4.31 (dd, *J*=1.97, 4.29 Hz, 3H), 1.77 (54H). FD MS *m/z* 900 (M^+), 899 (M^+-H), 898 (M^+-2H), 897 (M^+-3H).

Deutrated derivatives of 4.11. A solution of **4.10** (215 mg, 226 μmol) in CF_3COOD (2mL) was heated at 55 °C for 22 h. After cooling, the mixture was extracted with benzene, washed with saturated aqueous $NaHCO_3$ followed by with

brine, dried over Na_2SO_4 and filtered. Purification with column chromatography on silica gel [benzene/ehter (100:1, v/v)] gave deuterated **4.10** (163 mg, 76%). The same procedures as non-deuterated compounds affroded deuterated **4.11** (%D > 98%).

4,7,11,14,18,21-hexa-*tert*-butyltribenzodecacyclenyl radical (4.3•).

A mixture of **4.11** (41.5 mg, 46 μmol) and *p*-benzoquinone (12.4 mg, 115 μmol) in benzene (10 ml) was refluxed for 5 min. The mixture was cooled on ice-bath and 40 mL of hexane was added to the mixutre. The collected crude product was purified by column chromatography on silica gel [benzene/hexane (1:4, v/v)] to give **4.3•** (22.4 mg, 54%).

Trication (4.3^{3+}). A mixture of **4.11** (53 mg, 58.8 μmol) and *p*-benzoquinone (9.5 mg, 88.2 μmol) in benzene (10 ml) was refluxed for 10 min. The mixture was cooled on ice-bath and concentrated *in vacuo*. Hexane (20 mL) was added to the mixture and undissolved materials were removed by filtration. The filtrate was concentrated *in vacuo* and the resulting crude powder **4.3•** was dissolved in 5 mL of CH_2Cl_2 and cooled on ice-bath. Tris(*p*-bromophenyl)aminium hexachloroantimonate (142 mg, 174 μmol) was added to the solution and the reaction mixture was stirred for 7 h. The dark green precipitates were removed by filtration and 6 ml of hexane was added to the filtrate. The mixture was cooled at 0 °C and allowed to stand overnight. The resulting dark green powder was filtered, washed with hexane+CH_2Cl_2 (3:1) four times, and dried. Yield 58.1 mg (52%). Anal. Calcd for $C_{69}H_{69}Sb_3Cl_{18}$: C, 43.58; H, 3.66. Found: C, 43.06; H, 3.60.

Radical dication ($4.3^{(\bullet)(2+)}$). A mixture of **4.3•** (22.4 mg, 24.9 μmol) and tris(*p*-bromophenyl)aminium hexachloroantimonate (40.7 mg, 49.8 μmol) in 2 ml of CH_2Cl_2 was stirred at 0 °C for 2 h. Ether (6 mL) was added slowly to the mixture, which was allowed to stand overnight. The resulting dark green powder was filtered, washed with 2 mL of ether, and dried. Yield 10 mg (6.4 mg, 26%). Anal. Calcd for $C_{69}H_{69}Sb_2Cl_{12}$: C, 52.88; H, 4.44. Found: C, 53.09; H,4.30.

Monoanion and radical dianion (4.3^- and $4.3^{(\bullet)(2-)}$). Anions were generated in a sealed degassed cell (Figure 2.8.2) by the reaction of **4.3•** with a potassium mirror in THF or DME.

Trianion (4.3^{3-}). The reaction of the compounds **4.11** (7 mg, 7.8 μmol) with a potassium mirror in THF-d_8 (0.5 ml) in a sealed degassed tube afforded trianion species.

NMR spectroscopy.

Trianion (4.3^{3-}). The procedure for the generation of **4.3**$^{3-}$ is similar to that of **2.3**$^{2-}$. The contact of the THF-d_8 solution of **4.11** with a potassium mirror at - 78 °C for a week gave the red solution, whose NMR spectrum supported the generation of **4.3**$^{3-}$.

ESR spectroscopy.

Neutral (3.2). The cell A (Figure 2.8.2) was used for the ESR measurement of **3.2**. The *p*-chloranil (1 mg, 4 μmol) was introduced into the ESR tube ***a*** and 1 mL of the toluene solution of **3.2** (10^{-4} M) was added by a syringe. The cell was connected to a vacuum line at ***b*** and the solvent was degassed by a repeated freeze-pump-thaw method (5 times). The cell was sealed at ***c*** and heated at 60 °C for 5 min. The ESR spectra of **4.3**$^{\bullet}$ were recorded at -60 – 20 °C.

Radical dications and radical dianions (4.3$^{(\bullet)(2+)}$ and 4.3$^{(\bullet)(2-)}$). The procedures for the generation of **4.3**$^{(\bullet)(2+)}$ (3.3×10^{-4} M) and **4.3**$^{(\bullet)(2-)}$ (10^{-3} M) are similar to those of **2.3**$^{(\bullet)(+)}$ and **2.3**$^{(\bullet)(-)}$, respectively.

Monoanion. The procedures for the generation of **4.3**$^{-}$ (10^{-3} M) are similar to that of **2.3**$^{(\bullet)(-)}$. The contact of the DME solution with a potassium mirror at ***d*** exhibited the gradual decrease of signals of **4.3**$^{\bullet}$ and a new broad signal appeared. At this stage, the solution was freezed at -100 °C and the ESR spectrum was measured. However, no triplet signals were observed. Further contact with a potassium mirror gave the moderately-resolved ESR spectrum attributable to **4.3**$^{(\bullet)(2+)}$.

UV/Vis/NIR specroscopy.

Trication (4.3^{3+}). The quantitative electronic spectrum of **4.3**$^{3+}$ was obtained by the dissolution of the **4.3**$^{3+}\bullet(SbCl_6)_3$ (1.084 mg, 0.570 μmol) in D_2SO_4 (100 mL) at room temperature.

Neutral (3.2). The compound **3.2** was purified by a column chromatography (silica gel). The pure **3.2** was dissolved in cyclohexane and the qualitative measurement was carried out at room temperature.

Trianion (4.3^{3-}). The procedures for the generation of **4.3**$^{3-}$ are similar to that of **2.3**$^{2-}$. The contact of the THF solution of **4.11** (3.517×10^{-5} M) with a potassium mirror at ***d*** at room temperature gave a red purple solution, which exhibited the quantitative electronic spectrum of **4.3**$^{3-}$.

4.10 References

1) J. Heinze, *Angew. Chem. Int. Ed. Engl.* **1981**, *20*, 202.

2) A. T. Peters, *J. Chem. Soc.* **1942**, 562. H. E. Nürsten, A. T. Peters, *J. Chem. Soc.* **1950**, 729.

3) H. Angliker, E. Rommel, J. Wirz, *Chem. Phys. Lett.* **1982**, *87*, 208.

4) M. Gomberg, *J. Am. Chem. Soc.* **1900**, *22*, 757; *Chem. Ber.* **1900**, *33*, 3150.

5) C. F. Koelsch, *J. Am. Chem. Soc.* **1957**, *79*, 4439.

6) K. Ziegler, B. Schnell, *Liebigs Ann. Chem.* **1925**, *445*, 266. H. Sitzmann, H. Bock, R. Boese, T. Dezember, Z. Havlas, W. Kaim, M. Moscherosch, L. Zanathy, *J. Am. Chem. Soc.* **1993**, *115*, 12003.

7) D. H. Reid, *Chem. and Ind.* **1956**, 1504.

8) K. Goto, Master's Thesis, Osaka University, Japan, 1997.

9) E. de Boer, S. I. Weissman, *J. Am. Chem. Soc.* **1958**, *80*, 4549. R. Bachmann, F. Gerson, G. Gescheidt, E. Vogel, *J. Am. Chem. Soc.* **1992**, *114*, 10855. R. Bachmann, F. Gerson, C. Pütz, E. Vogel, *J. Chem. Soc. Perkin Trans. 2*, **1996**, 541.

10) For localization vs delocalization, see; S. Utamapanya, A. Rajca, *J. Am. Chem. Soc.* **1991**, *113*, 9242.

11) For electrostatic perturbation of counter cations, see; A. H. Reddoch, *J. Chem. Phys,* **1965**, *43*, 225.

List of Publication

1. Hexa-*tert*-butyltribenzodecacylenyl: A Six-Stage Amphoteric Redox System.
   T. Kubo, K. Yamamoto, K. Nakasuji, T. Takui, I. Murata, *Angew. Chem. Int. Ed. Engl.* **1996**, *35*, 439.

2. 2,5,8,11,14,17-Hexa-*tert*-butyldecacyclene.
   T. Kubo, K. Yamamoto, K. Nakasuji, N. Kanehisa, Y. Kai, in preparation.

3. 4,8,12,16-Tetra-*tert*-butyl-*s*-indaceno[1,2,3-*cd*:5,6,7-*c'd'*]diphenalene: A Four-Stage Amphoteric Redox System.
   K. Ohashi, T. Kubo, T. Masui, K. Yamamoto, K. Nakasuji, T. Takui, I. Murata, in preparation.

4. 4,9,13,16-Tetra-*tert*-butyl-*as*-indaceno[1,2,3-*cd*:6,7,8-*c'd'*]diphenalene: A Four-Stage Amphoteric Redox System.
   T. Kubo, K. Yamamoto, K. Nakasuji, T. Takui, in preparation.

Acknowledgment

The studies presented in this thesis have been carried out under the direction of Professor Kazuhiro Nakasuji at the Department of Chemistry, Graduate School of Science, Osaka University.

The author wishes to express my grateful gratitude to Professor Kazuhiro Nakasuji for his continuous guidance, helpful suggestion and encouragement throughout the work. The author is also deeply grateful to Associate Professor Kagetoshi Yamamoto for his valuable advice and stimulating discussions during the course of the work. The author wishes to thank Dr. Yasushi Morita and Dr. Jiro Toyada for their helpful advice and encouragement.

The author is greatly indebted to Emeritus Professor Ichiro Murata for his continuing interest, guidance and encouragement in the work. The author wishes to thank Professor Yoshikadu Sugihara, Department of Chemistry, Faculty of Science, Yamaguchi University, for his helpful advice and encouragement.

The author wishes to thank Professor Takeji Takui, Department of Chemistry, Faculty of Science, Osaka City University, for measurements of ESR spectra and his helpful discussion. The author is also grateful to Professor Yasushi Kai, Department of Chemistry, Faculty of Engineering, Osaka University, for X-ray analyses and his helpful advice.

The author is grateful to Dr. Ken-ichi Lee, Mr. Mikitsugu Doi, and Mr. Seiji Adachi, Faculty of Science, Osaka University, for NMR measurements, and to Mr. Hiroshi Adachi, Faculty of Science, Osaka University, for measurements of mass spectra, and to Mrs. Kazuyo Hayashi and Miss Tomomi Ikeuchi, Faculty of Science, Osaka University, for elemental analyses, and to Mr. Tetsuo Yamamoto, Faculty of Science, Osaka University, for X-ray measurements. The author also thanks Mrs. Takako Abe for her kind assistance, and all members of Nakasuji laboratory and Murata laboratory for their helpful discussions and kind friendship; in particular, Mr. Takashi Masui, Mr. Kenji Ohashi, Mr. Yoshinori Fujiwara, Mr. Kosaburo Goto, and Miss Minako Akabane participated in some of the work presented here as part of an research project; their help and suggestions are greatly appreciated.

Finally, the author is particularly indebted to his parents, Mr. Takahiro Kubo and Mrs. Kuniyo Kubo, for their hearty encouragement and assistance throughout the study.

久保孝史

Takashi Kubo

November, 1996

博士論文公開発表の要旨

1996年11月20日

大阪大学大学院理学研究科有機化学専攻博士後期課程　久保孝史

題目　「フェナレニル骨格を含む多段階両性レドックス系炭化水素に関する研究」

フェナレニルはカチオン、中性ラジカル、アニオンがいずれも熱力学的に安定であることで知られている。この事はフェナレニルラジカルを中心に考えてみると、酸化、及び還元が非常に容易に起こることを示している。この様な化合物の事を、二段階両性レドックス系化合物という。

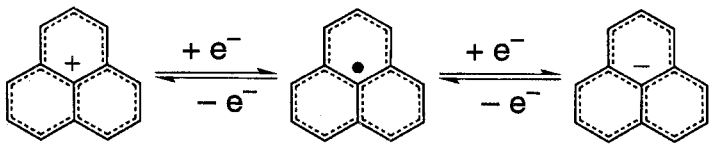

phenalenyl species

両性レドックス系の酸化還元能の高さは電気化学的な方法（サイクリックボルタンメトリー）によって見積もることが出来る。第一酸化電位（E_1^{ox}）と第一還元電位（E_1^{red}）の幅、すなわち E_1^{sum}（$E_1^{sum} = E_1^{ox} + (-E_1^{red})$）が小さければ酸化還元能が高いと判断できる。フェナレニルの E_1^{sum} は1.6 Vであり、通常の芳香族炭化水素（3から4 V）に比べると非常に小さい。これはこの化合物がNBMO（非結合性軌道）を有しているからである。ただ、フェナレニルラジカルの最大の欠点はラジカル種であるために速度論的に不安定であり、すぐに二量化してしまうことにある。

このフェナレニルを、その特徴を保ちつつ、一分子内に二つ組み込めば、高い酸化還元能を有する安定な閉殻化合物が期待できる。この考え方を基に当研究室では以下のような分子が合成され、その性質について調べられてきた。

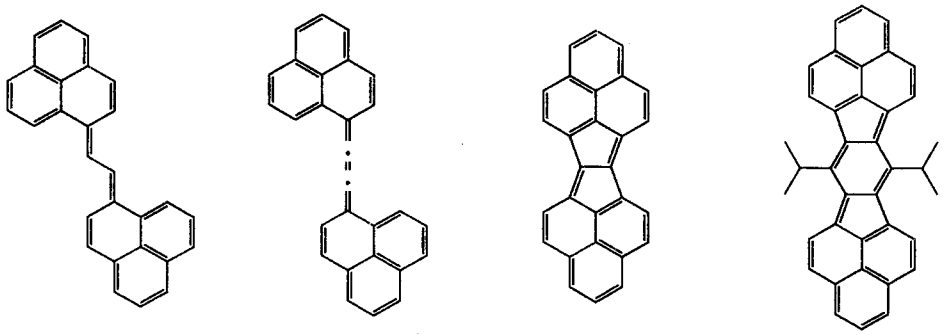

E_1^{sum}　1.51 V　　1.34 V　　0.99 V　　1.10 V

IDPL

注目の E_1^{sum} の値は非常に小さなものとなり、非常に高い酸化還元能を有していることがわかった。またこれらの分子は二つのフェナレニルが存在するため、四段階両性レドッ

クス系として振る舞うこともわかった。確かに酸化還元能の高さは実現できたわけだが、残念ながら、これらの化合物が与える酸化還元種は速度論的に不安定なものが多く、酸化還元状態の性質について詳細に調べることが出来なかった。

速度論的な不安定性の解消に対して嵩高い置換基は非常に効果的に働く。そこでIDPLに関して分子内に *tert*-butyl 基を導入することにより、速度論的な安定性を向上させ、酸化還元状態の性質を詳細に調べてみた。

1 は室温でも非常に安定であった。**1** はフェナレニル骨格を含む両性レドックス系炭化水素の中で初めてX線解析でその結晶構造が明らかとなった。骨格は完全に平面であり、D_{2h} という高い対称性を保持しており、π 電子は非局在化していることが示唆される。酸化還元能の目安となる E_1^{sum} は 1.16 V であり、置換基による影響はほとんど無い。またその電子スペクトルでは長波長部に吸収（755 nm）を与えており、**1** の HOMO–LUMO gap が非常に小さいということを示しており、CV の結果と矛盾しない。

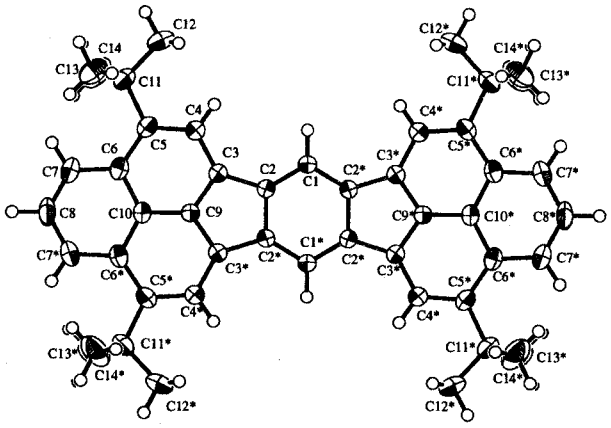

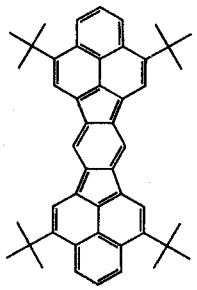

1

1 の構造異性体である **2** は **1** と異なり、極限構造式中では *o*-quinoid 骨格が現れてくる。*o*-quinodimethane は *p*-quinodimethane と比べると熱力学的に不安定で、HMO 計算による HOMO–LUMO gap は *o*-quinodimethane の方が小さい。つまり、**2** は **1** よりも更なる高い酸化還元能が期待できる。CV による E_1^{sum} の値は 1.00 V となり、**1** よりも小さくなっており、実際に酸化還元能が上がっていることがわかった。電子スペクトルも最長吸収波長は 1224 nm であり、**1** と比べると低エネルギー側にシフトしている。酸化還元状態の電子構造は ESR や ^{13}C NMR から基本的に **1** とほぼ同様であり、両性レドックス系としての性質にフェナレニル骨格が大きく貢献していることがわかった。

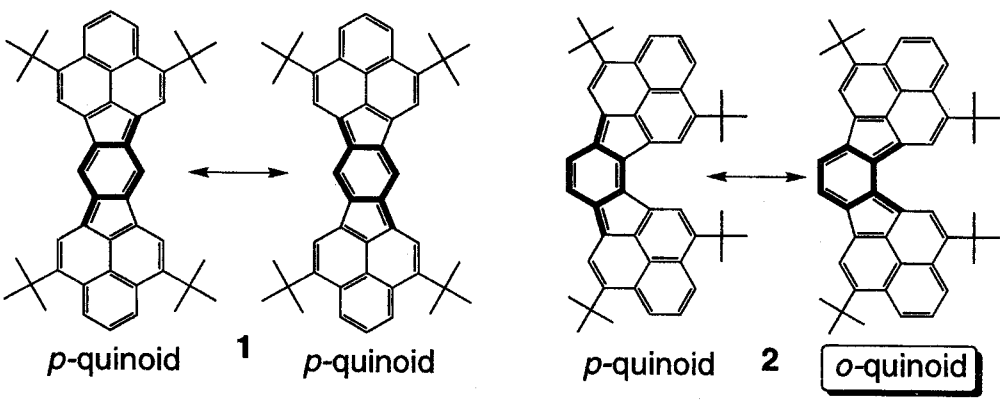

3$^{\bullet}$は三つのフェナレニル骨格を有し、より高度な両性レドックス系として振る舞うことが期待できる。CVでは六つの酸化還元波が観測され、六段階両性レドックス系として振る舞うことがわかった。つまり、**3**$^{\bullet}$は一つの化合物が七つの異なる電子状態を与えるという非常に珍しい例である。E_1^{sum}は0.78 Vとこれまで合成された両性レドックス系炭化水素の中では最も小さな値となり、電子スペクトルでは1340 nmに吸収を与えている。ESRや^{13}C NMRから、**3**$^{3+}$、**3**$^{(\bullet)(2+)}$、**3**$^{\bullet}$、**3**$^{3-}$に関してはスピンや電荷は主に三つのフェナレニル骨格上のα位に存在し、**1**や**2**の場合と同様に分子全体に非局在化していることがわかった。しかしながら、**3**$^{-}$や**3**$^{(\bullet)(-)}$に関しては、**1**$^{(\bullet)(-)}$や**2**$^{(\bullet)(-)}$と異なり、スピンや電荷は一つのフェナレニル骨格上に局在化しているとする解釈が妥当である。

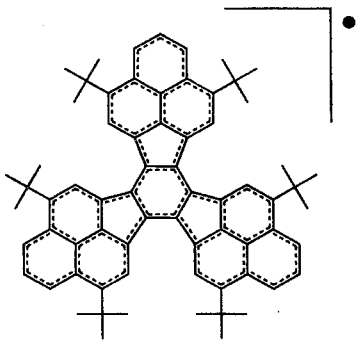

3$^{\bullet}$

以上、フェナレニル骨格を有する三種の縮合多環炭化水素は、良好な両性レドックス系として振る舞うことが分かった。即ち、二つのフェナレニル骨格を有するTTB-IDPL **1**、TTB-as-IDPL **2**は四段階両性レドックス系として、三つの骨格を有するHTB-TBzD **3**は六段階両性レドックス系として振る舞うことが分かった。両性度の高さの目安となるE_1^{sum}の値は**1**が1.16 V、**2**が1.00 V、**3**が0.78 Vとなり、全て、高い酸化還元能を有していた。酸化還元能が高いということはHOMO–LUMO gapが小さいということを示しており、これは電子スペクトルで長波長部に吸収が観測されるという事実と一致している。この酸化還元能の高さはフロンティア軌道がNBMO性を有しているためだと考えられる。フロンティア軌道のNBMO性は酸化還元状態の電子構造を調べることで明らかとなった。ESRや^{13}C NMRから得られた酸化還元状態の電子構造は、電荷やスピンは主にフェナレニル骨格上に存在し、しかもその分布の仕方はフェナレニル化学種のものと同様だった。つまり、α位上で大きくそれ以外では小さいことが分かった。発生した酸化還元種は全て室温でも安定に存在していた。これは嵩高い*tert*-butylの立体保護の効果のため、並びに電荷やスピンが主にフェナレニル骨格上に分布することにより、分子全体に広く非局在化するためだと考えられる。この様にフェナレニル骨格は高い酸化還元能、及び酸化還元種の高い安定性を発現させるのに非常に重要な役割を果たしていることが分かった。

	E_3^{ox}	E_2^{ox}	E_1^{ox}	E_1^{red}	E_2^{red}	E_3^{red}	E_1^{sum}	E_2^{sum}	E_3^{sum}	λ_{max}
1		+0.84	+0.48	-0.67	-1.25		1.16	2.09		755
2		+0.75	+0.42	-0.58	-0.96		1.00	1.71		1224
3$^{\bullet}$	+0.87	+0.68	+0.27	-0.51	-0.89	-1.25	0.78	1.57	2.12	1340

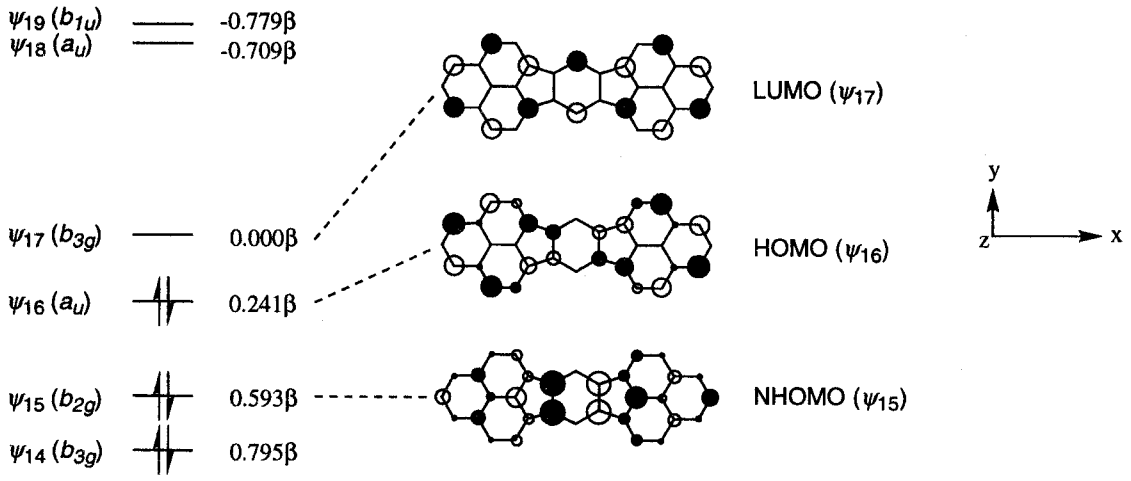

Figure 1. Selected molecular orbitals of **1** calculated by the HMO method.

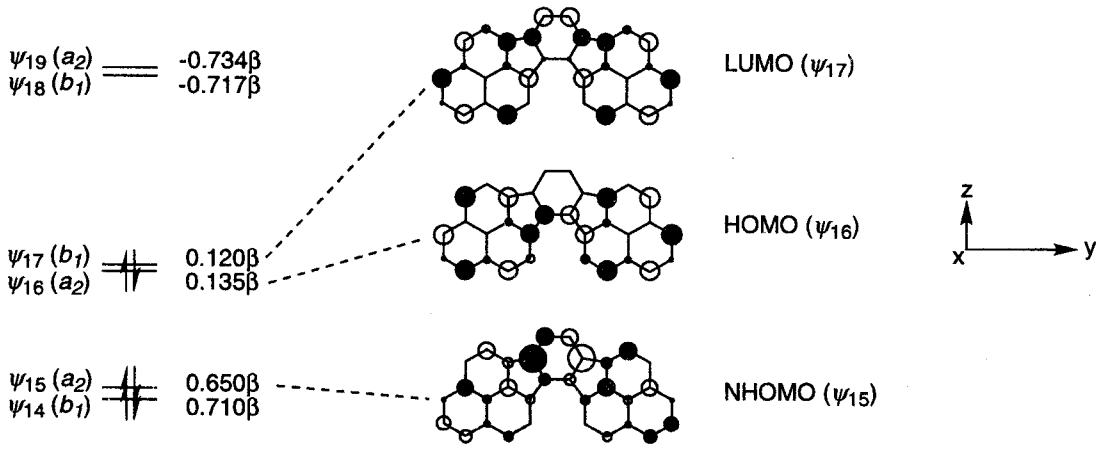

Figrure 2. Selected molecular orbitals of **2** calculated by the HMO method.

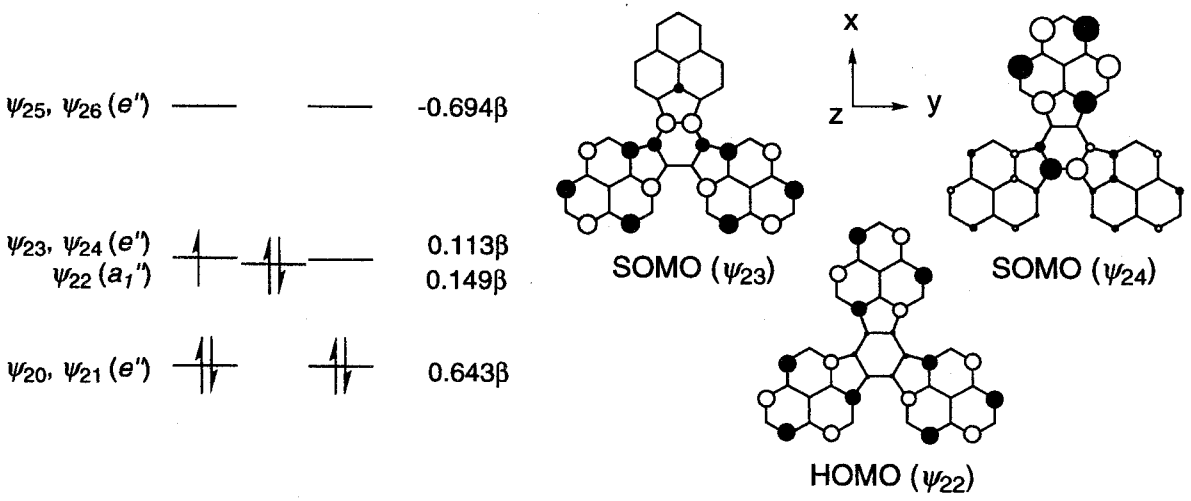

Figure 3. Selected molecular orbitals of **3**$^{\bullet}$ calculated by the HMO method.